VIETNAM NATIONAL UNIVERSITY
HANOI UNIVERSITY OF SCIENCE

NGUYEN THI PHUONG

SOLAR AND OTHER OBSERVATIONS USING A SMALL RADIO TELESCOPE

MASTER THESIS

ATOMIC PHYSICS

MAJOR ID: 60440106

SUPERVISORS: PR. PIERRE DARRIULAT

DR. PHAM NGOC DIEP

HANOI, 2016

ACKNOWLEDGEMENTS

The present work was performed at the Vietnam Astrophysics LaboratorY (VATLY), Institute for Nuclear Sciences and Technology (it has become Department of Astrophysics of Vietnam National Satellite Centre since Jan 1st, 2015) under supervision of Pr. Pierre Darriulat and Dr. Pham Ngoc Diep.

First of all, I would like to express my deepest gratitude to my supervisors, who have encouraged, supported and closely followed my work since the first day I joined the laboratory for my dissertation. Following closely their lectures and research life, I have learned and gained a lot of knowledge, both in the science and in the life. They are the most important people helping me to complete this thesis, without them this thesis is impossible. On this occasion, I would like to express my heartfelt to them for all of things they have been doing for me.

I would also like to give my thankfulness to all other VATLY members Dr. Pham Thi Tuyet Nhung, Dr. Nguyen Thi Thao, Dr. Do Thi Hoai and Dr. Pham Tuan Anh for their helping, encouragement, supporting since the first day I came. I am thankful for all the knowledge they have been sharing with me in the science and life. I am very lucky to become a member of this "family" and I am happy with this.

I am grateful to the teachers from the Faculty of Physics and the Nuclear Physics Department at Hanoi University of Science for all knowledge they have given me during the four years at undergraduate and two years at master when I studied at the University.

Last but not least, I am grateful to my family, who are always beside, take good care of me, believe and support all my decisions. I also thank my friends for their friendship, thank them for listening to me and sharing the life with me.

Hanoi, 25th May, 2016

Student

Nguyen Thi Phuong

CONTENTS

LIST OF FIGURES

LIST OF ABBREVIATIONS

ADC	**A**nalogue to **D**igital **C**onverter
AGN	**A**ctive **G**alactic **N**uclei
CME	**C**oronal **M**ass **E**jections
EUV	**E**xtreme **U**ltra-**V**iolet
FAST	**F**ive-hundred-meter **A**perture **S**pherical **T**elescope
GONG	**G**lobal **O**scillations **N**etwork **G**roup
IF	**I**ntermediate **F**requency
LNA	**L**ow **N**oise **A**mplifier
LO	**L**ocal **O**scillator
NOAA	**N**ational **O**ceanic and **A**tmospheric **A**dministration
PSF	**P**oint **S**pread **F**unction
RFI	**R**adio **F**requency **I**nterference
SF	**S**ignal **F**requency
SgrA*	**S**a**g**itta**r**ius **A***
SOHO	**So**lar and **H**eliospheric **O**bservatory
SRT	**S**mall **R**adio **T**elescope
VATLY	**V**ietnam **A**strophysics **T**raining **L**aborator**Y**
VLA	**V**ery **L**arge **A**rray
VLBA	**V**ery **L**arge **B**aseline **A**rray

INTRODUCTION

VATLY, the Vietnam Astrophysics Training LaboratorY, acquired a radio telescope[1] in April 2011, which was installed on the roof of the Institute for Nuclear Science and Technology (INST) in the premises of which VATLY was hosted[2]. It has a 2.6 m diameter antenna and is operated at frequencies in the neighbourhood of the 1.42 GHz frequency of the 21 cm hydrogen line. When I joined VATLY in 2013, the telescope had already been run-in and used to make observations of the Milky Way and of the Sun. Much of this work had been the substance of the master thesis of Nguyen Van Hiep (N.V. Hiep 2012) and of articles reporting the performance of the instrument (N.V. Hiep *et al.* 2012), the HI map in the Galaxy (N.V. Hiep *et al.* 2013) and observations of solar flares and oscillations (N.V. Hiep *et al.* 2014). I was then given the responsibility of the routine operation of the telescope and of the collection of data at the same time as I was progressively becoming familiar with their off-line analysis. The present thesis reports on observations that have been made since that time, on their analysis and interpretation. Much of this work has been described in greater detail in a VATLY internal note (N.T. Phuong *et al.*, VATLY internal note 51, 2014). The thesis is organised in four chapters, one dealing with the performance of the instrument, another with solar flares, the third with solar oscillations and the fourth with observations of the Moon. When relevant, they are preceded by a short introduction[3] recalling the main features of the topics being addressed.

[1] Custom Astronomical Support Services Inc. (CASSI), 436 Highview Dr., Jackson, MO 63755, USA.

[2] From January 1st, 2015, it has been moved to the roof of Education and Service Building of Vietnam Academy of Science and Technology (VAST) and VATLY has become the department of astrophysics of Viet Nam National Satellite Centre (VNSC).

[3] The sources used for the redaction of such introductions include lecture notes, in particular by Prof. Pierre Darriulat, and general articles from Internet sites such as NASA or Wikipedia. References are only given for material going beyond what can be considered as general textbook knowledge.

CHAPTER 1
THE VATLY RADIO TELESCOPE

1.1 Basics of radio astronomy

1.1.1 Overview

Radio waves have wavelengths in the millimetre to kilometre range. Above 100 m they are reflected by the ionosphere and cannot reach the Earth but in space, beyond the ionosphere, one could in principle detect radio waves up to 10 km wavelength (30 kHz). The first radio astronomical observations were made in 1932 by Karl Jansky, a Bell Lab physicist who detected cosmic radio noise from the Milky Way while investigating radio disturbances interfering with transoceanic communications. Since then, astronomers have built many radio telescopes with sophisticated systems that allow for a high angular resolution resulting in the production of detailed radio pictures of celestial objects.

Radio astronomy developed fast after World War II, focusing first on the most intense radio sources: Sun, Super Nova Remnants (SNR), the centre of the Milky Way (Sgr A*), quasars, Active Galactic Nuclei (AGN). The 21 cm hydrogen line allowed for the exploration of the galactic and extra galactic Universe. Millimetre radio astronomy developed in the last quarter of the XXth century.

Radio telescopes have two basic components: a large radio antenna (or set of antennas) and sensitive radio receivers. As an example, the Very Large Array (VLA) is one of the world's best astronomical radio observatories (Figure 1.1 left). It consists of three equal arms of 9 antennas each, symmetrically arranged at 120^{o} from each other. The antennas are parabolic, 25 m in diameter and the array is up to 36 km across.

Incoming signals are collected by the dish of the antenna and reflected by its parabolic surface to the focus where there is either another reflector or a receiver. In large radio telescopes, the receivers are usually located below the antenna and cooled down to 15 K in order to minimize thermal noise. The receiver amplifies separately the two opposite circular polarizations components of the signal.

Differential fluxes (also called flux densities, i.e. fluxes per unit of frequency) are measured in Jansky (10^{-26} Wm^{-2}Hz^{-1}). When the flux has its source in thermal emission, the frequency spectrum is that of a black body with a Planck distribution. In the case of radio waves, where one is dealing with large wavelengths, the Planck relation reduces to the so-called Rayleigh-Jeans relation: the flux Φ is related to the black body temperature T through the relation $\Phi = 2kT/\lambda^2$ where k is Boltzmann's constant and λ is the wavelength. The lowest temperature that can be detected is limited by the detector thermal noise and is equal to $T_{min} = T_r/\sqrt{B\tau}$ where B is the bandwidth, τ is the time of integration and T_r is the temperature of the receiver. The lowest detectable flux is therefore $2kT_{min}/\lambda^2$. In practice, one can go down to $T_{min}=10\ K$.

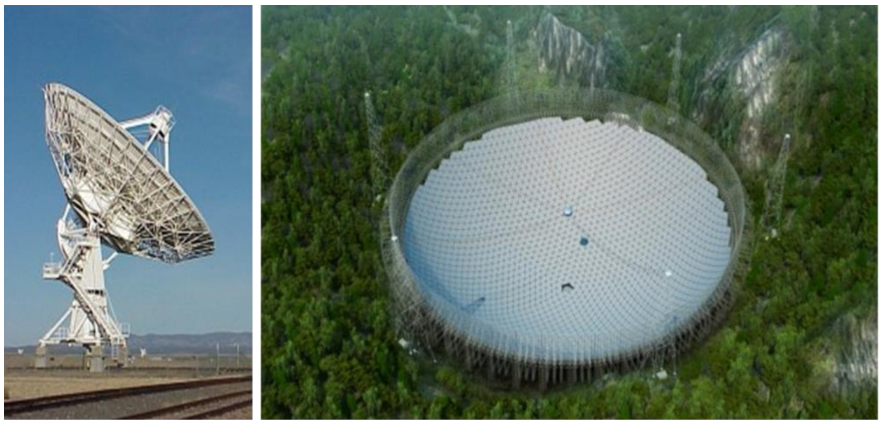

Figure 1.1 An antenna of the Very Large Array (left) and the Five-hundred-meter Aperture Spherical Telescope in construction in nearby China (right).

The sensitivity of a radio telescope, the ability to measure weak sources of radio emission, is proportional to the area and efficiency of the antenna and the sensitivity of the radio receiver used to amplify and detect the signal. For broadband continuum emission the sensitivity also trivially depends on the bandwidth of the receiver.

The angular resolution, or ability of a radio telescope to distinguish two neighbour sources, namely fine details in the sky, is limited by diffraction: it is equal to the ratio between the wavelength of observation and the diameter of the antenna of the instrument. This is at variance with ground observation in the visible where atmospheric turbulences (changing the index of refraction) rather than diffraction limit the angular resolution. For a same angular resolution a short wavelength antenna will therefore afford to be smaller than a large wavelength antenna.

Radio waves penetrate much of the gas and dust in space as well as the clouds of planetary atmospheres and pass through the terrestrial atmosphere with little distortion. In principle, radio astronomers can therefore obtain a much clearer picture of stars and galaxies than is possible by means of optical observation from ground. However this requires the use of very large antennas.

The first large parabolic antenna was built in Jodrell Bank (United Kingdom) in 1957 with a diameter of 75 m for wavelengths larger than 15 cm. The largest movable parabolic antenna is 100 m in diameter (Eiffel Mountain, Germany). Building significantly larger antennas is not possible: thermal and mechanical deformations distort the shape of the detector beyond the permissible limit, *i.e.* a fraction of a wavelength-typically one tenth. In 1963, Cornell University built a fixed antenna in Arecibo (Puerto Rico). It is 305 m in diameter and is installed in a natural basin. A larger antenna using a similar design (FAST, for Five-hundred-meter Aperture Spherical Telescope) is under current construction in nearby China (Figure 1.1 right). Parts of it, with sizes comparable to that of the Arecibo antenna, will be remotely shaped into a parabolic receptor by computer control. Better angular resolutions are achieved with interferometers, such as the VLA, with base lines that may be as large as the Earth diameter (Very Large Baseline Array, VLBA).

Radio sources can produce radio waves by thermal emission (usually resulting from the thermal movement of electrons and ions in a plasma) or by non-thermal emission (such as synchrotron radiation or coherent movements in oscillating plasmas). Thermal emission obeys the Rayleigh-Jeans relation. Outside of the solar system radio waves are good detectors of gas clouds in the interstellar matter, of supernova remnants and of plasmas of various kinds.

In addition to these continuous spectra there are also line spectra in radio astronomy as there are in the visible. The 21 cm hydrogen line, corresponding to the spin flip of the electron of a neutral hydrogen atom, is used in the present work. There also exist many molecular lines that tell us which molecules are present in interstellar clouds. Moreover, line spectra allow for a measurement of the velocity of the object from their Doppler shift: radio waves are good at observing highly red shifted molecular lines allowing for the study of far away galaxies in the early universe. Measuring the polarization of radio waves, which requires two independent receivers, provides useful additional information.

Figure 1.2 shows an overall view of the radio sky in galactic coordinates with a clear contribution of the Milky Way, in particular near the galactic centre.

1.1.2 Antennas

The elements of a standard radio telescope are the reflector, feed, transmission line and receiver. The reflector collects power from an astronomical source and provides directionality. The power collected by an antenna is approximately given by $P=S_\nu A\Delta\nu$, where S_ν is the flux density on Earth from some astronomical source, A is the effective area of the antenna and $\Delta\nu$ is the frequency interval or bandwidth of the measured radiation. An antenna operates the same way whether it is receiving or transmitting radiation (so-called reciprocity theorem). So the response pattern of an antenna, or Point Spread Function (PSF), that is receiving radiation is the same as that produced when the antenna is transmitting. It has a typical cardinal-sine, or Airy, shape, with a central lobe of size $\theta=\lambda/D$ (where λ is the wavelength and D is the dish diameter) surrounded by side lobes (Figure 1.3). The beam width θ is also a measure of the directivity of the antenna. More precisely, the angular pattern of the electric field in the far-field is the Fourier transform of the electric field distribution across the aperture.

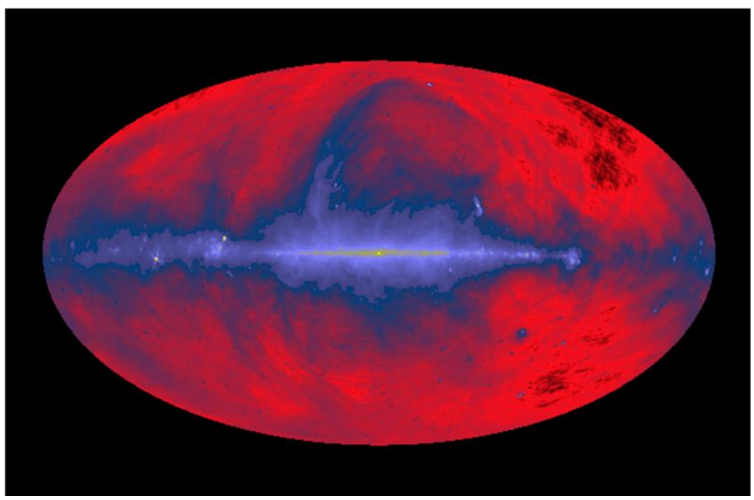

Figure 1.2 The radio sky 408 MHz continuum image *(*Haslam *et al*. 1982*)* (galactic coordinates)

Radio and radar engineers normally speak about antennas in terms of their gain in dB calculated as the ratio of powers P: $G = 10\log_{10} (P_{out}/P_{in}) = 20 \log_{10} (A_{out}/A_{in})$. A factor 2 is 3 dB (+ for amplification and – for attenuation), a factor 10 is 10 dB. The gain, G, of an antenna relative to isotropic is related to its effective collecting area, A, by $G=4\pi A/\lambda^2$, where λ is the wavelength. This means that the power collected in the pointing direction by an effective area A is G times higher than what an ideal isotropic antenna would collect, namely $\lambda^2/4\pi$. The beam solid angle is $\Omega_A=4\pi/G$ corresponding to a cone of $arctan(2/\sqrt{G})$ half aperture (measured in radians). The gain is therefore related to the directivity of the antenna: an antenna with a smaller beam will have a higher gain. To achieve an effective area or aperture of many square wavelengths, a parabolic reflector is the simplest and best approach.

With the availability of excellent Low Noise Amplifiers (LNAs), optimizing the antenna efficiency is less important than optimizing the ratio of efficiency to system noise temperature or gain over system temperature, G/T_s. This means that using a feed with low side lobes and slightly under-illuminating the dish may reduce T_s by more than it reduces G and so improve sensitivity.

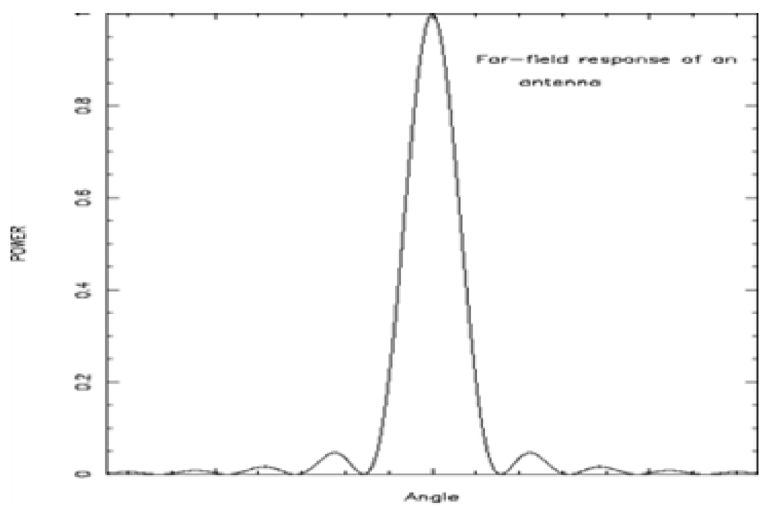

Figure 1.3 Fraunhofer pattern of a typical antenna response.

The antenna noise is a very important performance parameter along with the gain or equivalent effective aperture. Antenna noise originates from the sky background, Ohmic losses, and ground pickup or *spill over* from side lobes. While the sky noise cannot be acted upon, the losses and side lobes can be made small by a good design. Sky noise is frequency dependent but never gets any lower than the 2.7 K cosmic microwave background. The lowest system noise achievable is about 18 K.

1.1.3 Receivers

After the antenna, the first stage of the receiver, the low-noise amplifier (LNA), is probably the most important component of a radio telescope. Since the signals are so weak, the noise performance of the receiver is crucial, and this leads to big efforts, such as cryogenic cooling, to reduce noise in the LNA. The noise performance of radio-astronomy receivers is usually characterized by an equivalent system temperature, T_{sys}, referred to the feed or even to outside Earth's atmosphere. Using temperature units for the system allows direct comparison with source temperatures. Typical system temperatures are ten to a hundred K for centimetre wavelengths or up to several hundred K for millimetre and sub-millimetre wavelengths.

Most receivers use so-called super-heterodyne schemes. The goal is to transform the frequency of the signal (SF) down to a lower frequency, called the intermediate frequency (IF) that is easier to process, but without losing any of the information to be measured. This is accomplished by mixing the SF from the LNA with a local oscillator (LO) and filtering out any unwanted sideband in the IF. A bonus is that the SF can be shifted around in the IF, or alternatively, the IF for a given SF can be shifted around by shifting the LO.

Inside radio-astronomy receivers, a signal is usually represented by a voltage proportional to the electric field (as collected by the antenna). As it averages to zero, one needs a device that produces an output proportional to the square of the voltage, a so-called square-law detector, and that averages over at least a few cycles of the waveform.

It is not unusual to detect and measure signals that are less than 0.1% of the system noise. The increase in power, measured in K, due to the presence of a radio source in the beam is given by $2kT_a=AF$ where A is the effective aperture (or aperture efficiency times physical aperture), F is the radio flux density in $Wm^{-2}Hz^{-1}$, and k is Boltzmann's constant, 1.38×10^{-23} $WHz^{-1}K^{-1}$. While voltages in the antenna add up linearly at a given time, the lack of coherence between signal and background (unrelated phases) implies that they must be added in quadrature (i.e. the square root of the sum of their squares) to obtain the summed voltage averaged over several RF periods: it is indeed power that is relevant. Note that the factor of 2 in the left hand side of the above relation is because radio astronomers usually define the flux density as that present in both wave polarizations, but a receiver is sensitive to only one polarization. If the receiver gain is perfectly stable, our ability to measure small changes in signal is proportional to the square root of the time of integration.

All the final processing of a radio telescope output is done with a computer, after conversion in an Analogue to Digital Converter (ADC) of the analogue voltage from the detector to numbers that can be processed in software.

Radio astronomy is often limited by interference, especially at low frequencies. The spectrum is overcrowded with transmitters: Earth-based TV, satellite TV, FM, cellular phones, radars, and many others. Radio astronomy has some protected frequency bands, in particular at 21 cm, but these bands are often contaminated by harmonics accidentally radiated by TV transmitters, intermodulation from poorly designed transmitters, and noise from leaky high-voltage insulators and automobile ignition noise. Some of the worst offenders are poorly designed satellite transmitters, whose signals come from the sky so that they affect even radio telescopes that are well shielded from the local terrain.

1.1.4 The 21 cm line

The 21 cm line, also referred to as hydrogen line or HI line, is associated with the hyperfine transition of the hydrogen ground state. Its frequency is 1420.40575177 MHz, equivalent to the vacuum wavelength of 21.10611405413 cm in free space.

Hyperfine splitting (Figure 1.4) is the result of the spin-spin interaction between the electron and proton spins in the hydrogen atom. This transition is highly forbidden (it has $\Delta l=0$) with an extremely small probability of 2.9×10^{-15} s^{-1}. This means that the time for a single isolated atom of neutral hydrogen to undergo this transition is around 10^7 years and therefore difficult to observe on Earth. However, as the total number of atoms of neutral hydrogen in the interstellar medium is very large, this emission line is easily observed by radio telescopes. Moreover, the lifetime can be considerably shortened by collisions with other hydrogen atoms and interaction with the cosmic microwave background. The line has an extremely small natural width because of its long lifetime, so most broadening is due to Doppler shifts caused by the motion of the emitting regions relative to the observer.

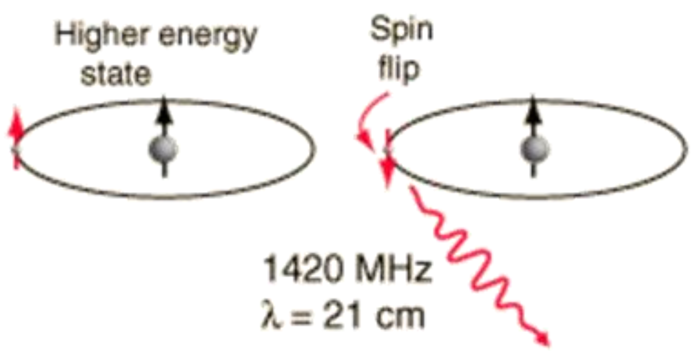

Figure 1.4 Hyperfine splitting of the hydrogen ground state

First predicted in 1944 by J.H. Oort and H. van de Hulst (1945), the 21 cm line was first detected in 1951 by Ewen and Purcell (1951) at Harvard University and shortly after confirmed by C.A. Muller and J.H. Oort (1951). The first maps of neutral hydrogen in the Milky Way were then made and revealed, for the first time, its spiral structure. Assuming that the hydrogen atoms are uniformly distributed throughout the galaxy, each line of sight through the galaxy will reveal a hydrogen line. The only difference between each of these lines is their Doppler shift. Hence, mapping the 21 cm line allows for measuring the rotation curve of the Galaxy and, once it is known, to map its arm structure. Hydrogen line observations have also been used indirectly to calculate the mass of galaxies, to put limits on any changes over time of the universal gravitational constant and to study dynamics of individual galaxies.

1.2 The VATLY radio telescope: overview and early measurements

1.2.1. General description

The telescope is equipped with a steerable parabolic dish, 2.6 m in diameter, remotely adjustable in elevation and azimuth (Figure 1.5). The reflected power is collected at the focus, where it is locally preamplifier, shifted to lower frequency using standard super-heterodyne, amplified and digitized.

Figure 1.5 Close-up views of the telescope antenna and of the motor system (gear box and telescopic arm (left panel) and of the feed horn and the calibration antenna (right panel).

The feed includes a two-turn left polarization helix antenna, meaning that the telescope observes the right circular polarization component of the detected wave. Super-heterodyne uses a local oscillator frequency range of 1370 to 1800 MHz and an intermediate frequency centred on 800 kHz with a 6 dB range of 0.5 to 3 MHz. The back end includes analog-to-digital conversion (ADC) on a dedicated PCI card, data being transferred to a hard disk for off-line analysis. Typical system temperature (including all non-astronomic sources) is of the order of 200 K to 250 K. A block diagram of the electronics is shown in Figure 1.6.

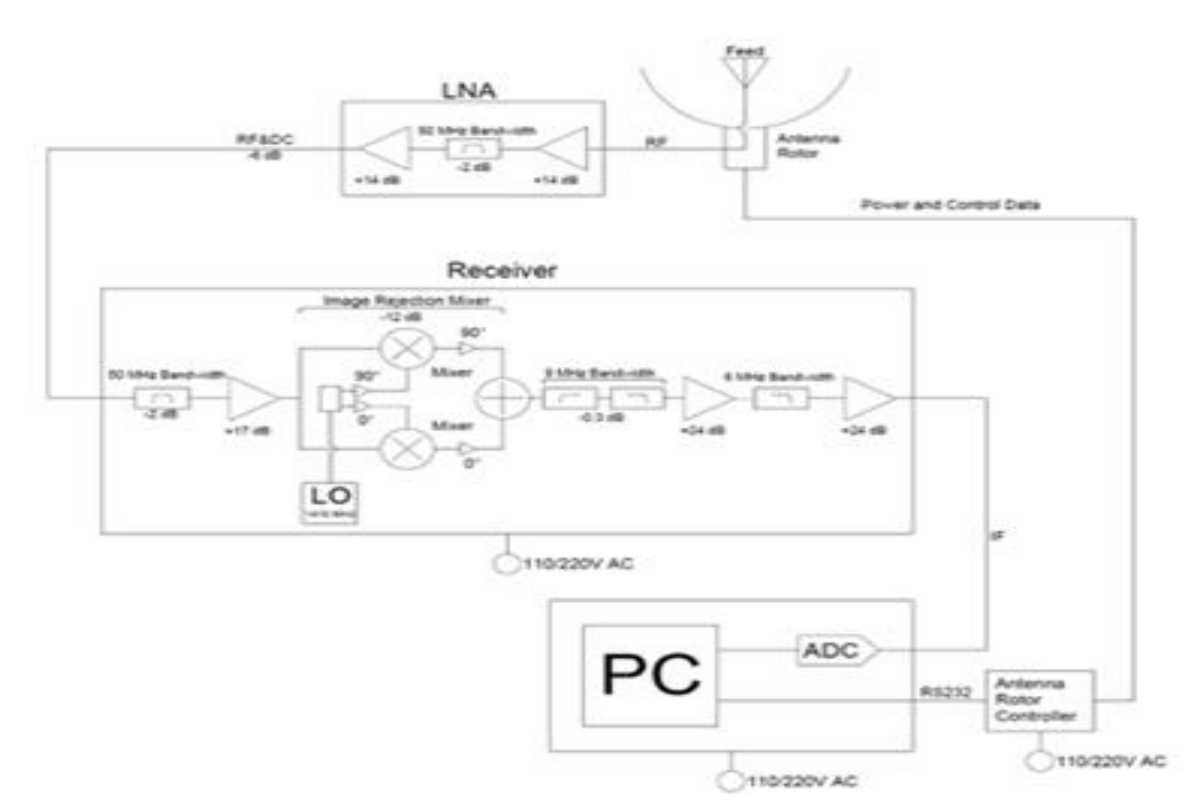

Figure 1.6 Block diagram of the electronics.

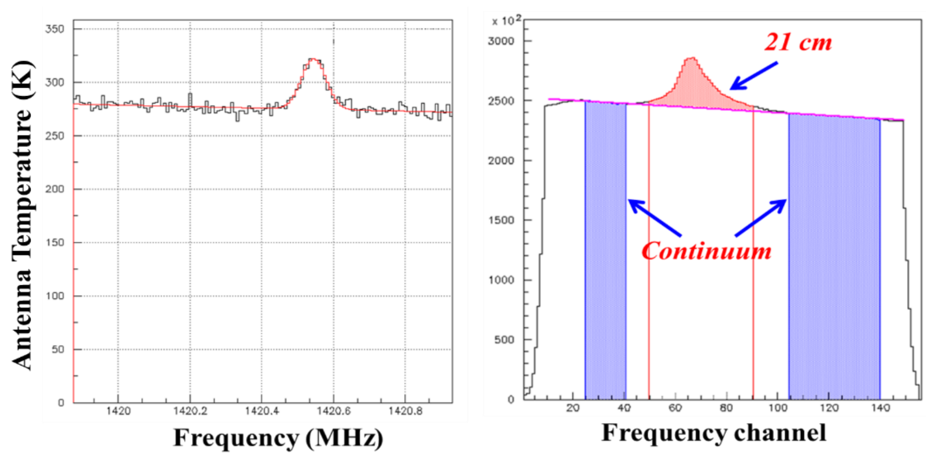

Figure 1.7 A typical frequency spectrum (left) and its decomposition in 21 cm and continuum signals (right).

Standard data collection consists of a sequence of successive measurements of ~8 s duration each, digitized in the form of a frequency histogram covering ~1.2 MHz in 156 bins of ~7.8 kHz each (obtained by stitching together three adjacent bandwidths).

Such a typical distribution is shown in Figure 1.7 (left). The 21 cm hydrogen line is clearly seen above a slowly varying continuum, revealing the presence of hydrogen clouds in the field of view.

The telescope orientation is remotely adjustable and a small TV camera allows watching the antenna movement from the control room below where a desktop displays the data being recorded and other relevant information.

1.2.2. The background sky and measurement accuracy

When pointing the telescope to a fixed direction in the sky, one records the sum of a general background and of signals associated with radio sources passing by as the Earth rotates (one speaks of drift scans). Examples of drift scans on the Sun and on SgrA* respectively are illustrated in the next sections.

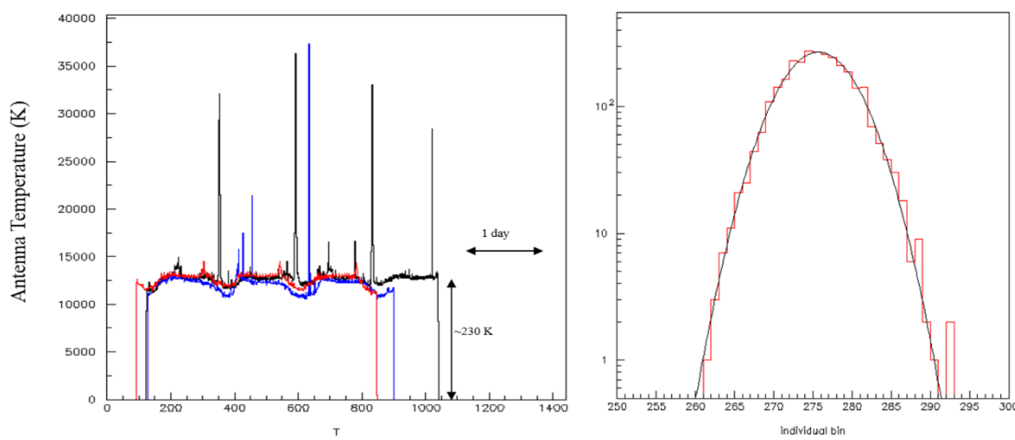

Figure 1.8 Left: Time dependence of the content of frequency bin number *35*. The abscissa is measured in tenths of an hour. The full range is nearly *5* days. Different colours correspond to different elevations. The first three large black spikes are due to the Sun passing by. Right: Distribution of measurements made in a single frequency bin during a stable period of ~ *6.2* hours after correction for slow drifts.

In the present section, we are not interested in a particular radio source but rather in the contribution of the background. Collecting such data over several days shows the presence of spikes, sometimes occurring on a single day, sometimes repeating each day (Figure 1.8 left). They are the result of anthropogenic parasites (Radio Frequency Interferences, RFIs) having their source in the severe electromagnetic pollution that exists above Hanoi and they become more important at low elevations as can be expected. They are nevertheless easily removed to obtain frequency distributions free of parasitic interferences. In order to illustrate the stability of the response, we show in

Figure 1.8 (right) the distribution of the signal measured in a same frequency bin over a ~6.2 h period (after correction for slow drifts). The fact that the distribution is well described by a Gaussian indicates that the measurement uncertainties are dominated by noise. A systematic study of such data allows for an estimate of the relative measurement uncertainty obtained for a single frequency bin by summing *n* successive measurements:

$$\frac{\Delta P}{P} = \sqrt{\frac{(0.27\%)^2+(1.59\%)^2}{n}} \tag{1.1}$$

For *n~35*, corresponding to *4.7 min*, the two terms under the square root are equal, giving an optimal time scale of, say, *~10 min* per measurement. The constant term, *~0.3%* (meaning an antenna temperature of ~0.6 K) is of systematic origin and essentially common to all frequency bins: it gives a measure of the best possible accuracy obtainable in measuring the power flux of a given radio source.

1.2.3. The Sun: grid scans and pointing accuracy

The Sun gives a strong signal in the continuum while the 21 cm line is essentially unaffected. As its apparent diameter is much smaller than the antenna lobe (the Sun seen at 21 cm is dominated by solar spots above a disk having the same size as the photosphere) the Sun can be considered as being a point source and be used to assess the telescope pointing accuracy.

In order to reveal possible pointing errors, grid scans (Figure 1.9) are made at different times of the day. Each grid scan takes only 6 *min* and consists in 25 measurements pointing to the nodes of a 5×5 grid centred on the Sun and having a mesh size of ~2.6° (½ beam width) in elevation *h* and ~2.6°/*cosh* in azimuth *a*.

The angular distance d_i between the true Sun and grid node *i* at the time when it is being measured is easily calculated by using the relation

$$cosd = \cos(h_1 - h_2) - cosh_1 cosh_2[1 - \cos(a_1 - a_2)] \tag{1.2}$$

which gives the angular separation between the directions (a_1, h_1) and (a_2, h_2).

In the limit of small angular separations relation (1.2) reduces to:

$$d^2 = (h_1 - h_2)^2 + cosh_1 cosh_2 (a_1 - a_2)^2 \tag{1.3}$$

Locally, one has a Euclidean metric in coordinates *(coshda, dh)*. The best Gaussian fit of the measured signals S_i, integrated over frequency, to a form $A + Bexp[-0.5(d^2/\sigma^2)]$ is used to define the telescope offsets in azimuth and elevation, δa and δh.

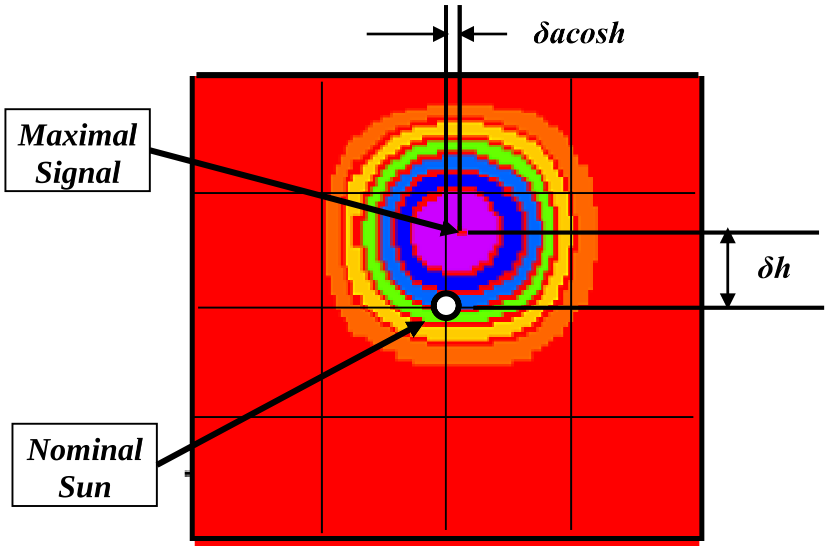

Figure 1.9 A typical grid scan: the 5×5 grid, centred on the nominal Sun, is shown together with the signal density in local coordinates *(dacosh,dh)*. The definition of the offsets is illustrated.

In practice, in addition to δa and δh, A and B are free parameters adjusted by the fit while σ, a measure of the lobe size, is fixed at 2.34° (see below). Two main causes come to mind to explain why δa and δh deviate significantly from zero: a possible tilt of the antenna rotation axis with respect to vertical and zero offsets of the azimuth and elevation scales. A tilt by an angle ε_0 in a plane of azimuth a_0 generates offsets

$$\delta a = -\varepsilon_0 \sin(a - a_0) \tan h \text{ and } \delta h = -\varepsilon_0 \cos(a - a_0) \quad (1.4)$$

Defining $\varepsilon_1 = \varepsilon_0 sina_0$ and $\varepsilon_2 = \varepsilon_0 cosa_0$, one obtains

$$\delta a = \varepsilon_1 cosatanh - \varepsilon_2 sinatanh \text{ and } \delta h = -\varepsilon_1 sina - \varepsilon_2 cosa \quad (1.5)$$

where both ε_1 and ε_2 are small angles.

We call ε_3 the zero offset of the azimuth scale. Rather than defining a zero offset of the elevation scale, it is better to define a zero offset ε_4 of the length of the telescopic arm that changes the elevation to which the telescope is pointing. This implies writing the zero offset of the elevation scale as $\varepsilon_4 \partial h/\partial l$ where the function $\partial h/\partial l$ has been calculated from the geometry of the movement:

$$\frac{\partial h}{\partial l} = -\frac{0.00792+0.666\ 10^{-3} f}{g} \quad (1.6)$$

where $f = 51.1 - 0.391h - 0.00254h^2 + 0.77\ 10^{-5}h^3$

and $g = \sqrt{1 - (0.956 - 0.00792f - 0.333\ 10^{-3}\ f^2)^2}$

One can now express δa and δh in terms of four small parameters $\varepsilon_{1\ to\ 4}$ which define the correction to apply to the nominal pointing direction of the telescope and are related to the azimuth and elevation offsets by the relations:

$$\delta a = \varepsilon_1 cosatanh - \varepsilon_2 sinatanh + \varepsilon_3$$

$$\delta h = -\varepsilon_1 sina - \varepsilon_2 cosa + \varepsilon_4 \partial h/\partial l \qquad (1.7)$$

Here, the tilt angle is $\varepsilon_0 = \sqrt{\varepsilon_1{}^2 + \varepsilon_2{}^2}$ and the azimuth of the tilt plane is $a_0 = tan^{-1}(\varepsilon_1/\varepsilon_2)$.

Measurements performed soon after installation revealed a tilt of $\varepsilon_0=1.2^o$ in the plane of azimuth 37.2^o and allowed for an evaluation of the pointing error accuracy: $cosh\Delta a=0.1^o$, $\Delta h=0.15^o$.

In 2013, the telescopic arm controlling the elevation of the dish axis jammed, necessitating a repair and new calibration grid scans. Between August and October 2013, over hundred grid scans have been collected. The values of the best fit parameters are:

$\varepsilon_1 = 0.89 \pm 0.03$, $\varepsilon_2 = 0.82 \pm 0.06$, $\varepsilon_3 =-0.10 \pm 0.01$, $\varepsilon_4 = 1.07 \pm 0.03$

corresponding to ε_0=1.2^o for an azimuth of the tilt plane a_0=47^o, in good agreement with earlier values. The difference between measured and calculated offsets have rms values of 0.22^o in $cosh\Delta a$ and 0.11^o in Δh.

The movement of the dish is controlled by two motors to which one sends pulses, each pulse causing a step of 0.42^o in azimuth or 0.85 mm in the length of the telescopic arm, namely, at an elevation of 45^o, an angular step of ~0.3^o (0.30^o in $coshda$ and 0.13^0 in elevation). The above quoted rms values correspond to a third of a motor step in azimuth and one motor step in elevation.

1.2.4 The Sun: drift scans

Drift scans are made by pointing the telescope to a given nominal Sun position during the whole duration of the scan, starting approximately half an hour before and ending approximately half an hour after the expected transit of the Sun at that point (Figure 1.10, left). The exact time at which the recorded signal is maximal defines a line in the sky to which the telescope must be pointing. This line is the locus of points for which the distance to the Sun trajectory is minimal at the point where the signal is maximal, namely the major circle normal to the Sun trajectory at the point where the signal is maximal. Calling h* and a* the elevation and azimuth of this point and h and a the elevation and azimuth of the direction to which the telescope is pointing, the projection d on the Sun trajectory of the vector joining these two directions is a measure of the telescope offset. Precisely, calling $(cos\theta, sin\theta)$ the unit vector along the Sun trajectory in local coordinates $(dacosh, dh)$,

$$d = (a - a^*)coshcos\omega + (h - h^*)sin\omega \quad (1.8)$$

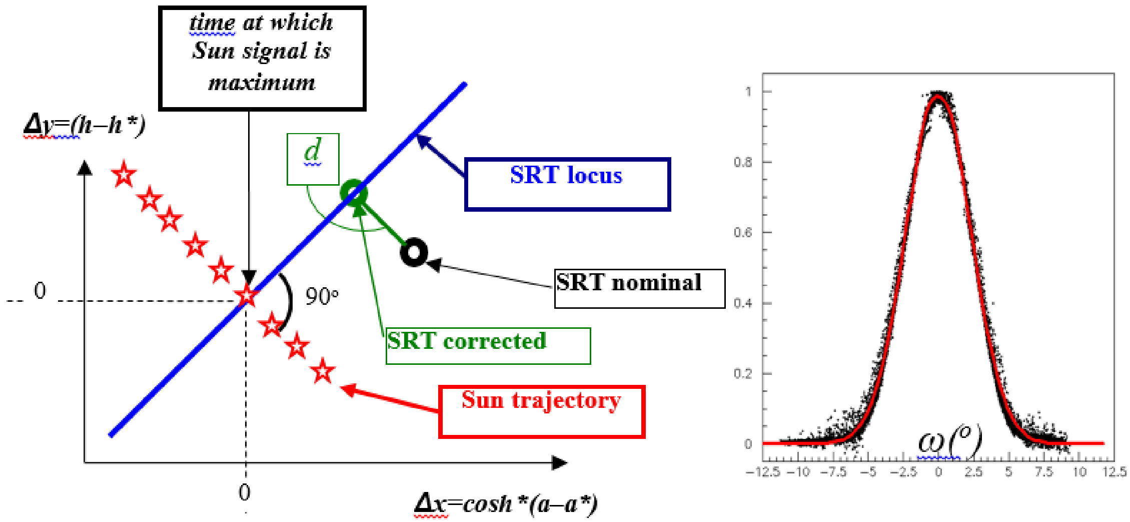

Figure 1.10 Left: Principle schematics of a drift scan (SRT stands for Small Radio Telescope). Right: Dependence of the amplitude of the Sun signal on the angular separation between Sun and telescope. The best Gaussian fit is shown as a red line.

Typically, the rms deviation of d around its mean is 1.2^o before and 0.3^o after applying pointing corrections, which is consistent with the rms values obtained from the grid scans and suggesting to retain an estimate of 0.3^o for the overall pointing accuracy. Drift scans provide a measurement of the shape of the antenna lobe as illustrated in Figure 1.10 (right) where the dependence of the signal, after subtraction of the background and proper normalisation, is displayed as a function of the angular separation ω between Sun and SRT (using best fit pointing corrections obtained from the drift scans). The FWHM of the antenna lobe is measured this way to be 5.4 ± 0.2^o, corresponding to $\sigma=2.3\pm0.1^o$.

1.2.5 The centre of the Galaxy: a strong 21cm signal

Drift scans across the disk of the Milky Way give evidence for a strong 21 cm signal. The centre of the Galaxy contains a black hole, Sgr A*, having a mass of some 3 million solar masses; it is a strong radio source. The disk of the Galaxy, and particularly its centre, contain a large number of hydrogen clouds that are the source of the observed 21 cm signal.

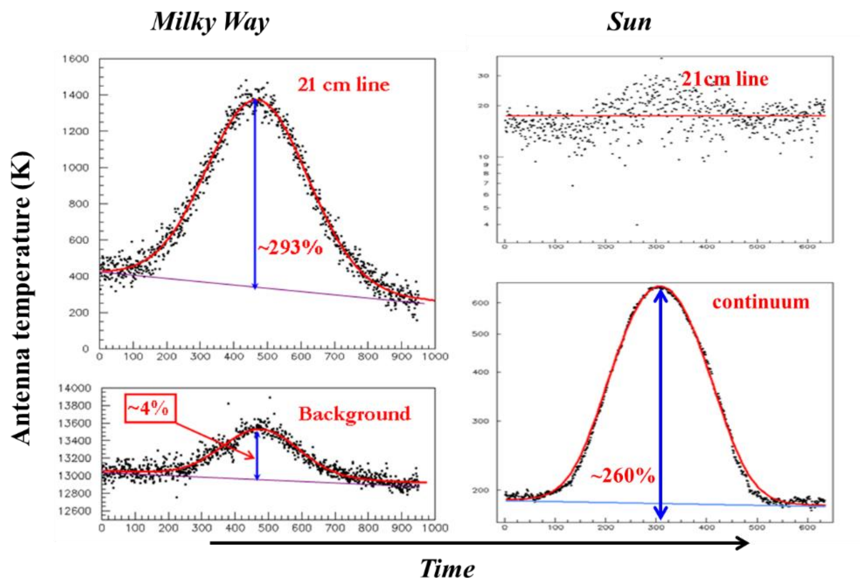

Figure 1.11 Drift scans across the centre of the Milky Way (left) and across the Sun (right). The 21 cm signal (upper panels) and the continuum signal (lower panels) are shown separately. The difference between the Milky Way, dominated by hydrogen clouds, and the Sun, dominated by a hot plasma, is spectacular.

Figure 1.11 illustrates such a drift scan and compares it with a drift scan across the Sun. In the former case, there is only a small enhancement of the continuum, due to the much higher density of stars in the direction of Sgr A*, while the 21 cm signal is nearly tripled due to the presence of hydrogen clouds. In the Sun case, on the contrary, it is the continuum signal that is strongly enhanced, again by a factor of nearly 3, while the 21 cm signal is essentially unaffected. Indeed, there is no enhancement of neutral hydrogen in the direction of the Sun.

1.3 Drift scans across the Sun

1.3.1 General features

Drift scans across the Sun being a convenient source of information allowing for tracking the antenna temperature from the normal sky level up to that of the Sun, both in the continuum and on the 21 cm line, we performed a number of new scans in 2013. The procedure, illustrated in Figure 1.12, is essentially the same as described earlier (Figure

1.10). Data are collected over two hours starting at time t (h), the telescope pointing to the position at which the Sun passes at time $t+1$. This allows for the study of three regions, labelled 1 to 3 in the figure, corresponding to periods before, during and after Sun crossing. The frequency spectra, using a central frequency of 1420.4 MHz, allow for defining a continuum level by linear interpolation on either side of the 21 cm HI line and for evaluating the contribution of the line by subtraction of the continuum. While the Sun does not emit significantly on the line, its continuum contribution, in quiet state, is typically a factor ~6 above that of the empty sky.

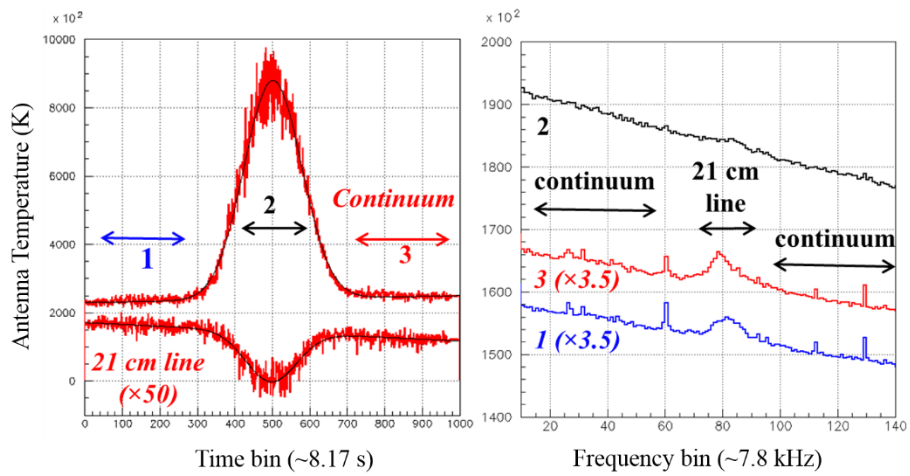

Figure 1.12 Left panel: time dependence of the spectral flux density (arbitrary units) for the continuum and the 21 cm line (multiplied by 50) separately; the abscissa, in measurement numbers, covers two hours. Right panel: frequency spectra measured before (blue, 100-300) during (black, 450-650) and after (red, 750-950) Sun crossing. The blue and red spectra have been multiplied by 3.5 for convenience.

1.3.2 Frequency dependence of the gain

Over the bandwidth, the frequency dependence of the continuum is expected to be negligible. The decrease observed in Figure 1.12, of nearly 10% in total, is purely instrumental. A linear fit to the continuum of the form $ai+b$, where i labels the frequency bin, allows for the study of the dependence of a on b when scanning across the Sun and on the central frequency f by taking drift scans at different f values.

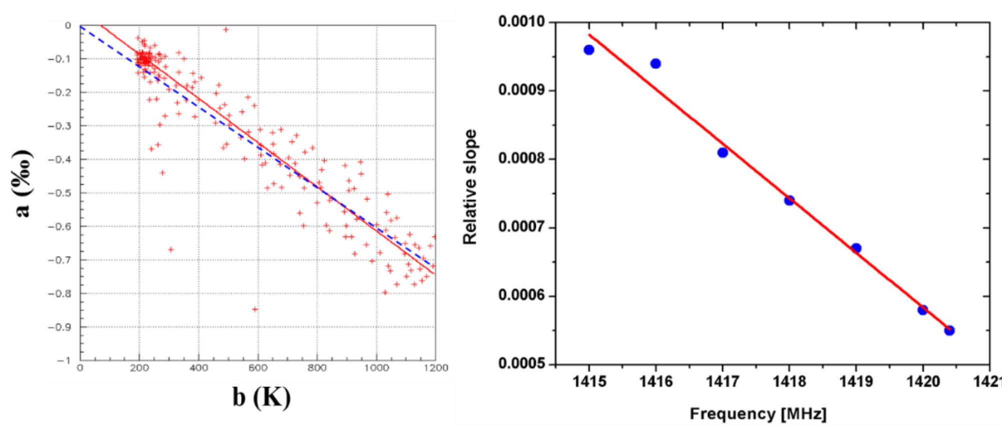

Figure 1.13 Left panel: dependence of *a* (‰) on *b* (K). The dotted line shows perfect proportionality as a reference. Right panel: dependence of –*a/b* on central frequency (MHz).

The relative gain drop per frequency channel is 0.55‰ (*i.e.* ~70 ppm/kHz) at a central frequency of 1420.4 MHz and decreases by 80 ppm (*i.e.* ~10 ppm/kHz) per MHz of central frequency.

1.3.3 Non-linearity of the response

When scanning across the Sun, the contribution of the 21 cm line is seen to drop to zero (Figures 1.12 and 1.14 left). The cause is instrumental as the Sun covers a negligible part, at the percent level, of the field of view: it results from a small non linearity of the response causing too large a continuum subtraction on the Sun. Indeed, the contribution of the Sun to the 21 cm line is obtained by subtracting off-the-Sun from on-the-Sun two large numbers: the total contribution (line+continuum). However, in both cases, the line is a minor fraction of the continuum and a small lack of linearity causes a large overestimate of the quantity to be subtracted. Assuming a non linearity proportional to the signal, *i.e.* a quadratic response with a linear dependence of the gain on amplitude, it is sufficient to have a gain 4.6‰ times lower on-the-Sun than off-the-Sun to explain the effect, or, equivalently, 6.2‰ smaller on the Sun than at zero amplitude.

1.3.4 Small corrections related with the 3-bandwidth structure

The three bandwidth structure of the frequency spectra is revealed by small imperfections of the response: slight differences, of the order of 2.5‰±1.5‰, between their respective gains and, for each of these, a slight enhancement in the middle of the bandwidth with respect to its edges as illustrated in Figure 1.14 (right). The latter is well described by a parabolic shape having a same sagitta in each of the three bandwidths. It has a broad distribution with a mean value of 1.8 ‰ and an rms value of 1.6 ‰.

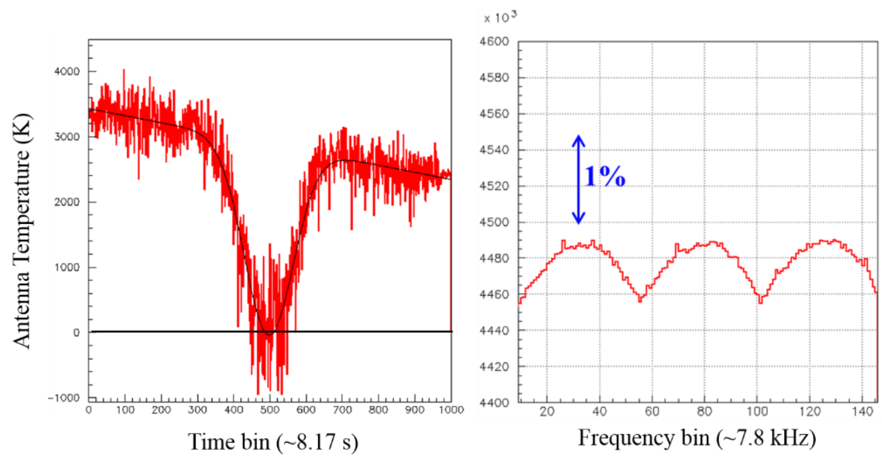

Figure 1.14 Left: The 21 cm line integrated between frequency channels 78 and 91 and over 74 drift scans of two hours each is displayed as a function of time (500 corresponding to the Sun position). Right: Three-bandwidth structure of a frequency spectrum corrected for the frequency dependence of the gain discussed in Section 1.3.2. Here, the relative sagitta of the parabolic bumps is ~6‰, more than twice the average value.

1.4 Interferences (RFIs)

Spikes, occurring in a few adjacent frequency bins, or bumps, covering some 20 adjacent bins, namely ~150 kHz, are occasionally observed. By changing the value of the central frequency, one can verify that they occur at well-defined frequencies. Both spikes and bumps have relative amplitudes with respect to the underlying continuum at the few percent level, occasionally reaching a few 10%.

1.4.1 Bumps and spikes in the frequency spectrum

Figure 1.15 displays data collected at 1417.6 MHz at 10^{o} elevation and 190^{o} azimuth (0^{o} in azimuth pointing to the north) during the night of 17th to 18th February 2014. The frequency spectrum shows a spike and a bump, the amplitudes of which are observed to switch on and off at well-defined times, providing evidence for their human origin. Note that the spike remains present during the whole night (7 pm to 7 am), however at much lower amplitude than during the day.

Mapping the sky around this direction reveals the presence of another bump, also of human origin, at an azimuth of 180^{o}. While the spike is relatively well localised over a region consistent with the size of the main antenna lobe, the bumps are nearly twice as broad. Such behaviour is typical. Moreover, varying the central frequency in steps of 0.25 MHz between 1415 and 1425 MHz reveals the existence of a whole sequence of bumps spaced by 1.2 MHz typically and having a width of some 150 kHz and a variety of amplitudes at the level of a few percent. Harmonics, reflections on obstacles, detection into side lobes or pick-up by the electronics contribute to such interferences, making it difficult to identify precisely their sources. They are usually easy to remove when reducing the data and do not significantly deteriorate the quality of the observations.

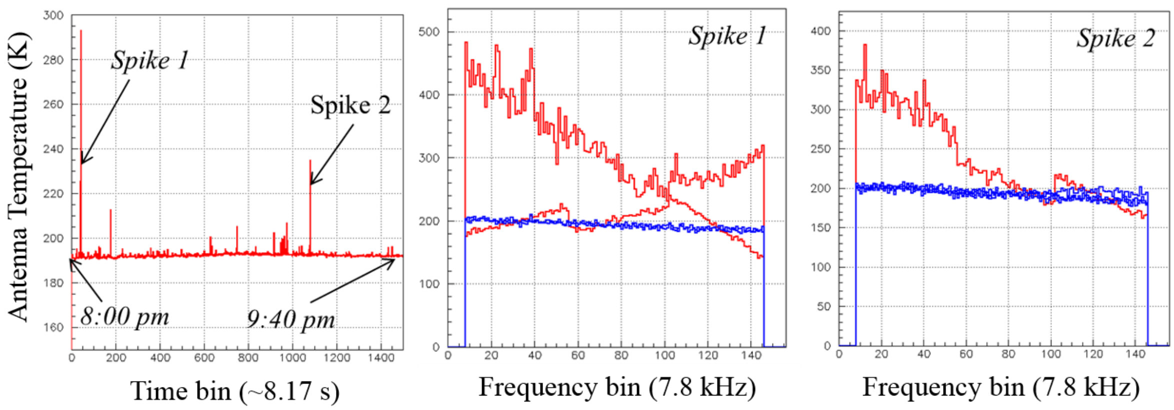

Figure 1.15 Spikes in the time dependence of the spectral flux density. Left: a typical time distribution; Centre and right: frequency spectra associated with the largest spikes. The spectra bracketing the spike are in blue, those measured on the spike in red.

1.5 Sensitivity and stability

In addition to external interferences, spikes and bumps, or the presence of multipath oscillations, noise, including electronic noise as well as gain fluctuations due to other sources, limits the sensitivity of the instrument.

1.5.1 Fluctuations

A first evaluation of the noise is obtained from the rms fluctuations of the antenna temperature around its mean when observing the Sun. Figure 1.16 displays the distribution of the χ^2 to a fit allowing for multipath oscillations covering the months of November and December 2013, using a reference uncertainty of 3‰. The mean value of the distribution, 1.58, implies a mean noise level of $3\sqrt{1.58} = 3.8$‰ of the solar signal, namely ~5.3 K.

A second evaluation is obtained from the spectral flux density recorded during quiet hours of the night between 12th and 13th February 2014. The data collected between 0:20 and 2:30 local time are split in 10 lumps of 100 measurements each, corresponding to 13.6 min for each lump. The flux in each lump is fit to a second order polynomial dependence on time with respect to which the rms deviation is calculated. For an average temperature of 191.5 K, the mean rms fluctuation is measured to be 0.28 K, namely a noise to signal ratio of 1.5‰.

Depending on where it occurs in the amplification chain, the noise can be expected to include a constant term and a term proportional to the signal. From the above examples, we may retain as a conservative estimate a background to noise ratio making it possible to detect signals at the permil level above background by making long enough observations.

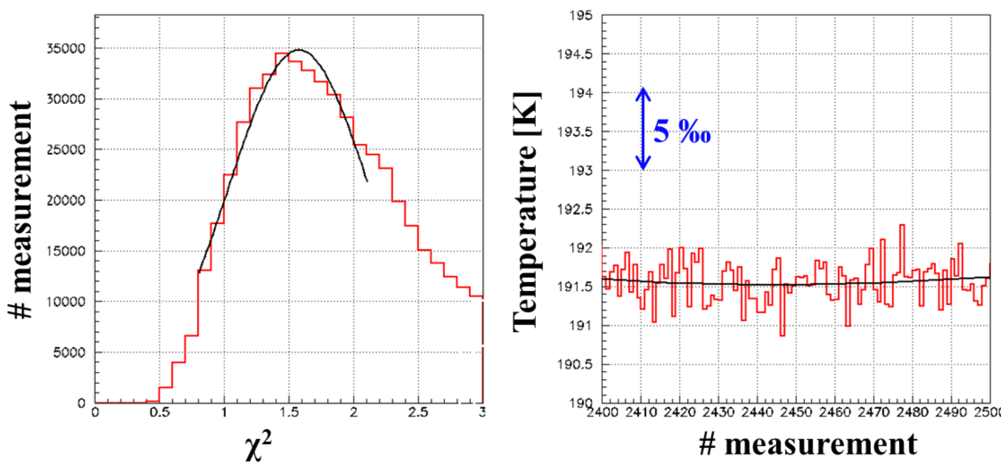

Figure 1.16 Left panel: Distribution of the χ^2 per degree of freedom, using arbitrary uncertainties of 3‰, to a fit of solar data allowing for multipath oscillations. Right panel: distribution of the temperature recorded during a February 2014 night in one of the ten 13.6 min lumps used for the noise analysis. The line shows the polynomial fit.

1.5.2 Weak sources

A confirmation has been obtained by observing radio sources such as Cygnus X and the Crab, expected at the few kJy level. The latter illustrates well the practical limit of what can be reliably achieved on such sources. Figure 1.17 left shows the detection of the Crab at the ~1K level over a ~250K background from a set of 34 drift scans across the Crab. Also shown is the result of 21 drift scans across points that are shifted by ±10° of galactic longitude with respect to the Crab. In such a case, the sensitivity is limited by the need to subtract spikes associated with human interferences, which could not be done reliably for significantly lower signals.

In summary, reliable measurements can be performed with an accuracy of a few permil over short periods and of a few percent over a whole day down to a lower limit of ~0.3 K. Main limitations are uncontrolled slow gain drifts in the case of long observation times and small spikes caused by human interferences in the case of drift scans. In practice, it is difficult to reach sensitivities better than ~1 K, corresponding to ~800 Jy. Yet, a sensitivity of only 300 Jy has been reached in a study of the radio emission of the Moon, as reported in Chapter 4.

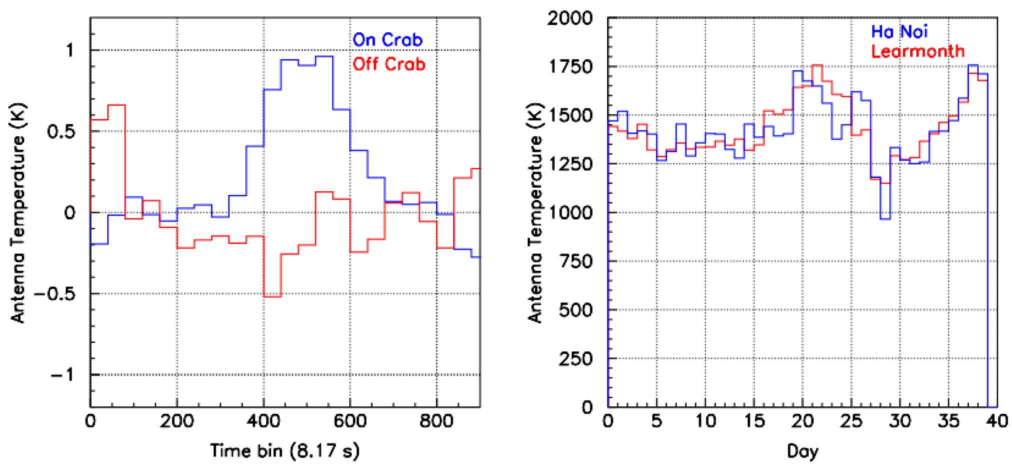

Figure 1.17 Left: Antenna temperature (K) averaged over 34 drift scans across the Crab (blue) and over 21 drift scans shifted by ±10^o in galactic longitude (red). Right: Distribution of daily averaged solar fluxes measured in Learmonth (red) normalised to the Ha Noi system temperature in K and Ha Noi (blue) from October 25th to December 9th 2013.

1.5.3 Efficiency factor

The daily averaged solar fluxes measured between October 25th and December 9th 2013 are compared in Figure 1.17 right with measurements made at the same frequency during the same period by the Learmonth solar observatory located at opposite latitude but same longitude as Ha Noi. Their daily averaged rms deviations are 2.7% and 1.3% respectively, mostly due to slow drifts such as caused by changes in the ambient temperature. More precisely, the Ha Noi data are of the antenna temperature, 1438 K on average, and the Learmonth data of the spectral flux density, 115 SFU on average (1 SFU=10^4 Jy). Their ratio has a narrow distribution having a mean value of 12.5 K/SFU with an rms deviation of 0.9 K/SFU (7%) with respect to the mean. It corresponds to an antenna effective area of 3.45 m^2 for a true area of 5.3 m^2, namely an efficiency factor of 65%. In Ha Noi, a calibration was performed each morning using a calibrated noise resistor and pointing to a fixed quiet region of the sky, measuring 206 K on average with an rms deviation with respect to the mean of 9 K (4.4%).

1.6 Summary and conclusions

The performance of the VATLY radio telescope, operated in Ha Noi on and near the 21 cm HI line, has been studied. Quantities such as the pointing accuracy ($0.11^o \times 0.22^o$), the beam width (σ=2.3^o) and the frequency resolution (7.8 kHz) have been evaluated.

Drift scans across the Sun have revealed a small dependence of the gain on frequency, measured as a relative gain drop of ~70 ppm/kHz at a central frequency of 1420.4 MHz, itself decreasing by ~10 ppm/kHz per MHz of central frequency, implying a gain drop of nearly 130 ppm/kHz at a central frequency of 1415 MHz. The gain was also observed to decrease when the amplitude of the detected signal increases, being 6.2‰ smaller on the Sun than at zero amplitude, meaning a relative gain drop of ~5 ppm/K of antenna temperature. A small modulation of the gain, in the form of three adjacent enhancements having sagittas at the level of a few permil, results from the stitching together of three separate bandwidths.

Human interferences have been found to be ubiquitous, either in the form of spikes in the frequency spectra, usually at well-defined frequencies and sky coverage, or in the form of brief spikes affecting all frequencies for a single, or at most a few successive measurements. Such interferences practically limit the sensitivity of the instrument at the level of a few hundred Jy. Observations over extended periods suffer small gain drifts that imply daily averaged rms deviations of ~2.7%, typically twice as large as achieved at the Learmonth Australian solar observatory using a similar instrument. Comparison between simultaneous observations performed in Ha Noi and in Learmonth are consistent with an antenna efficiency factor of ~65% and a conversion factor of 1.25 K/kJy fluctuating with an rms deviation of 0.09 K/kJy (7%) with respect to the mean. Very large spikes may occasionally occur, causing major disturbance to the system as do major solar flares.

The performance of the VATLY radio telescope as a training tool is remarkable and offers excellent opportunities for students to become familiar with the techniques and methods of radio astronomy. While giving access to detailed studies of strong radio sources, such as the Sun in the continuum or the disk of the Milky Way on the 21 cm line, its ability to detect sources of lesser strength is limited to a very few, such as Cygnus X or the Crab.

CHAPTER 2

SOLAR FLARES

2.1 Introduction to solar physics

The Sun has recently gone through a new phase of activity (Figure 2.1) after a long period of quietude[4]. Solar flares occur frequently, associated with large radio bursts that tend to last longer than the visible flares (Loughhead et al., 1957). In the present chapter, we present the results of solar observations made between spring 2012 and spring 2014 at frequencies in the 1.4 GHz range.

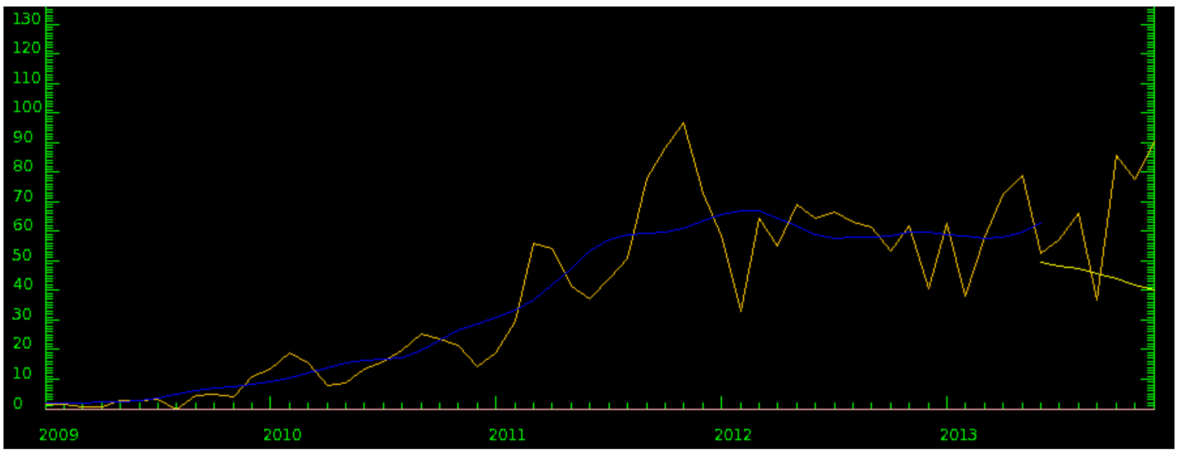

Figure 2.1 Dependence of the Sun spot number on calendar time. The transition from cycle 23 to cycle 24 is defined as occurring on 1st January 2008.

2.1.1 Solar activity monitors

The Sun activity is continuously monitored from both space and ground based observatories, such as SOHO[5] and TESIS[6] for the former and LEARMONTH[7] and NOBEYAMA[8] for the latter (Figure 2.2).

SOHO was launched on December 2nd, 1995 and was designed to observe the Sun continuously for at least two years, to study its internal structure, its extensive outer

[4] http://www.n3kl.org/sun/noaa.html; http://www.n3kl.org/sun/status.html; http://www.universetoday.com/10846/predicting-times-for-clear-space-weather
[5] soho.nascom.nasa.gov
[6] http://www.tesis.lebedev.ru/en/sun_flares.html
[7] http://www.ips.gov.au/World_Data_Centre/1/10
[8] http://solar.nro.nao.ac.jp/norh/html/event/

atmosphere and the origin of the solar wind, the stream of highly ionized gas that blows continuously outward through the Solar System.

Figure 2.2 Upper left: radio antennas at the Learmonth solar observatory on the North West Cape of Australia; Upper right: The TESIS satellite; Lower: Nobeyama radioheliograph (Japan).

TESIS is a set of solar imaging instruments developed by the Lebedev Physical Institute of the Russian Academy of Science, launched on January 30th, 2009. Its main goal is to provide observations of solar active phenomena from the transition region to the inner and outer solar corona with high spatial, spectral and temporal resolution in the EUV and Soft X-ray spectral bands. It includes an Imaging Spectroheliometer (MISH), a EUV Spectroheliometer (EUSH), two Full-disk EUV Telescopes (FET) and an X-ray photometer-spectroheliometer (SphinX). Its main tasks are the study of the mechanisms of solar wind generation and coronal heating, the development of methods for space weather forecasting, the study of the production and evolution of high-temperature plasmas in the corona and the analysis of processes of magnetic energy accumulation and release before and during flares.

The LEARMONTH Solar Observatory, in Western Australia, is located at a longitude 8^{o} east of Hanoi, which makes it particularly well suited for comparisons with our data. Its solar radio telescopes monitor both the quiet and active Sun, at 245, 410, 610, 1415, 2695, 4995, 8800, and 15400 MHz. The background solar radio emission (the quiet Sun) and solar radio bursts (the active Sun) that can exceed the background solar radio emissions by several orders of magnitude are made available to the public. The magnetic structure of individual sunspot groups is observed in solar magnetograms.

The NOBEYAMA Radioheliograph (Japan) observes the Sun 8 hours per day measuring both intensity and polarization at different frequencies around 17, 35 and 80 GHz. An interferometer array of eighty-four antennas, 80 cm in diameter, covering 490 m east/west and 220 m north/south in a T-shaped configuration, provide radio images of the Sun at the maximum rate of 20 images per second. It views the full solar disk at a resolution of 5” to 10”, and has a time resolution of 0.1 second.

The Solar Data Services of the National Oceanic and Atmospheric Administration (NOAA) handle, archive, and distribute solar data from the following disciplines: Solar Features, Solar Imagery, Solar Indices Data, Solar Indices Bulletin and Miscellaneous Solar Data[9]

2.1.2 Solar flares

At the beginning of a solar cycle, sunspots form between 30 and 50 degrees of the solar equator. As the solar cycle progresses from its minimum to its maximum and on to the next minimum, sunspots form at progressively lower latitudes until, by the second solar minimum, sunspots are forming very close to the equator. Flares occur in active regions around sunspots, where intense magnetic fields penetrate the photosphere to link the corona to the solar interior. Flares are powered by the sudden (timescales of minutes to tens of minutes) release of magnetic energy stored in the corona. The same energy releases may produce coronal mass ejections (CME). Radio, X-ray and UV radiation emitted by solar flares can affect Earth's ionosphere and disrupt long-range radio communications. The frequency of occurrence of solar flares varies, from several per day when the Sun is particularly active to less than one every week when the Sun is quiet.

Flares occur when accelerated charged particles, mainly electrons, interact with the plasma medium. Magnetic reconnection is responsible for the acceleration of the charged particles, the magnetic field winding faster at low latitudes than at high latitudes. On the Sun, magnetic reconnection may happen on solar arcades of magnetic lines that quickly reconnect, leaving a helix of magnetic field unconnected to the rest of the arcade (Figure 2.3). The sudden release of energy in this reconnection is at the origin of the particle acceleration. The unconnected magnetic helical field and the material that it contains may violently expand outwards forming a coronal mass ejection.

---

[9] http://www.ngdc.noaa.gov/stp/spaceweather.html

Solar flares are classified as A, B, C, M or X according to the peak flux (in W/m^2) near Earth: A$<10^{-7}$, B 10^{-7} to 10^{-6}, C 10^{-6} to 10^{-5}, M 10^{-5} to 10^{-4} and X$>10^{-4}$. Within a class, a linear scale goes from 1 to 9. Powerful X-class flares create radiation storms that produce auroras.

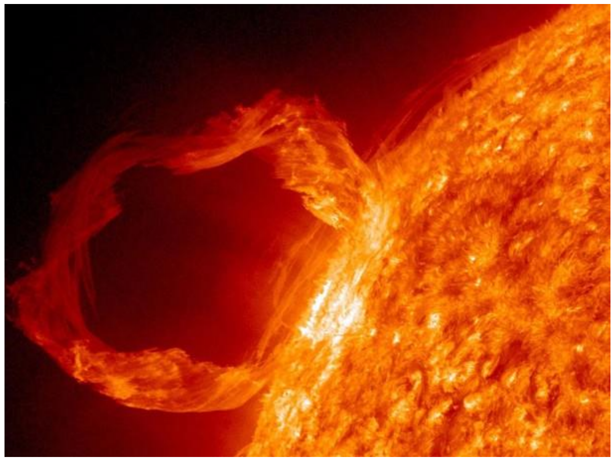

Figure 2.3 A very large and strong solar flare (NASA/GSFC/Solar Dynamics Observatory's AIA Instrument)

2.1.3 Helioseismology

It was only in 1960 that Sun's oscillation were first observed, by Robert Leighton, Robert Noyes, and George Simon, and in 1970-1971 that Roger Ulrich, John Leibacher, and Robert Stein were able to describe their pattern in terms of trapped acoustic waves. This explanation predicted certain detailed features of the spectrum of solar oscillations that were confirmed by observations made in 1975 by Franz Deubner. In the eighties, helioseismology developed rapidly and 1995 saw the birth of two major observational efforts: GONG (Global Oscillations Network Group), a ground-based network of six telescopes around the globe, and SOHO, space based. These observatories have contributed much to our understanding of the inner structure and dynamics of the Sun. A typical oscillation episode, measured on the H_α line, is shown in Figure 2.4.

Acoustic waves cannot propagate in a medium with variable density unless their wavelength is smaller than the length over which the density changes significantly. The rapid decrease in density at the solar surface causes sound waves of frequency less than about 5 mHz (periods greater than 3.3 minutes) to be reflected and thus trapped inside the Sun. Due to this trapping, the Sun rings at discrete frequencies which are its normal mode frequencies. Several millions of these normal modes are seen (Figure 2.5), labelled by their spherical harmonic indices, with observed periods between 3 and 12 minutes, typical surface velocities of about 5 cm/s, and lifetimes of a few days. The modes are thought to be excited by turbulence in the convection zone.

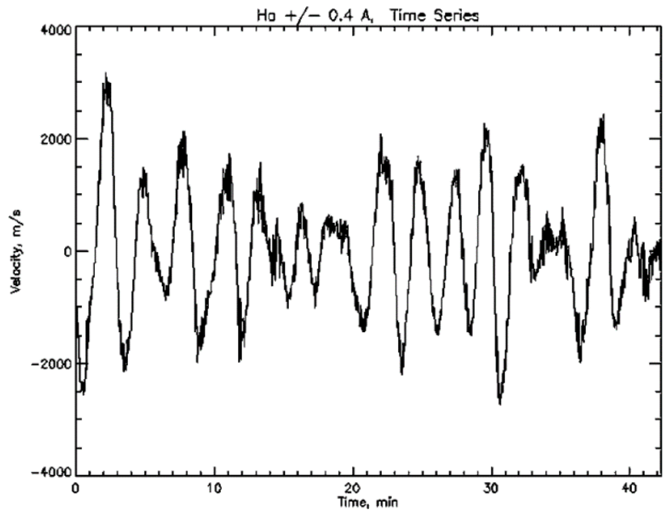

Figure 2.4 Data from the Sayan solar observatory (Siberia) on the H_α line taken on 18/08/2004 between 01:01 and 01:43 UT

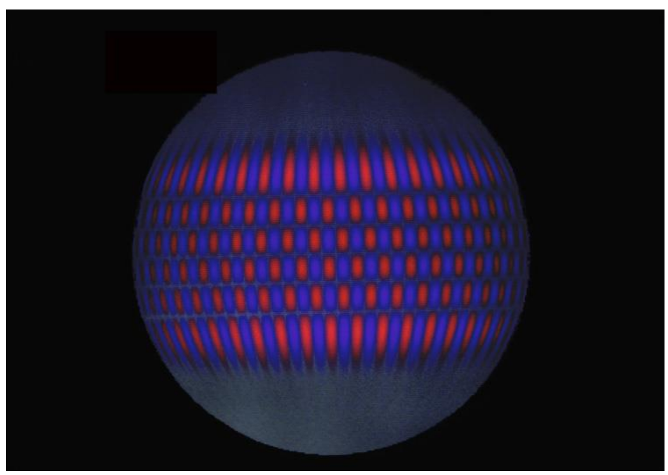

Figure 2.5 The velocity field at the solar surface associated with a mode of *l*=12 and *m*=10. Bright regions are moving toward us and dark regions away from us (or conversely).

The measurement of frequencies of different modes enables us to determine the sound speed and other variables in the solar interior as a function of depth. These oscillations have provided a powerful observational tool in the study of the solar interior, in a way similar to the use of earthquakes by seismologists. The two dimensional power spectrum of oscillations, called *l*-*v* diagram, was observed to contain discrete ridges, different ridges corresponding to eigenmodes with different numbers of nodes in the radial direction. This established that these oscillations are superpositions of global, non-radial, acoustic normal modes (known as p-modes) of the Sun.

Various kinds of wave motions have been observed in sunspots. These include characteristic umbra oscillations (the umbra is the inner, dark, cool (~ 3700 K) region of a sun spot) with periods around 3 minutes, umbra oscillations with periods around 5 minutes (which differ in several respects from the 5-minute *p*-mode oscillations in the quiet photosphere), and large-scale propagating waves in the penumbra. These oscillatory phenomena are of some interest, as being the most readily observable examples of magneto hydrodynamic (MHD) waves under astrophysical conditions. In addition, observations of oscillations in a sunspot and its nearby surroundings can be used to probe the structure of a sunspot below the solar surface ("sunspot seismology"). Interest in sunspot oscillations began in 1969 with the discovery of periodic umbra flashes in the Ca II H and K lines. These flashes were soon attributed to the compressive effects of magneto-acoustic waves. In 1972 three other types of sunspot oscillations were discovered: running penumbral waves in Hα, 3-minute velocity oscillations in the umbra photosphere and chromosphere, and 5-minute velocity oscillations in the umbra photosphere. For some time these three types of oscillations were considered as distinct phenomena, but recent work suggests that they might actually be different manifestations of the same coherent oscillations of the entire sunspot.

2.2 Observations

As a by-product of observations (N.V. Hiep *et al.* 2014, P. N. Diep *et al.* 2014) of the Sun using the VATLY radio telescope (N.V. Hiep *et al.* 2012, N.T. Phuong *et al.* 2014), a sample of 34 solar flares observed simultaneously in Ha Noi and Learmonth (Australian Government) has been collected. Of these, 7 were recorded in a first campaign of observation at 1415 MHz, between April and September 2012, the remaining 27 in a second campaign at 1417 MHz between October 2013 and January 2014.

Ha Noi and Learmonth are located at nearby longitudes (105.8^{o}E and 114.1^{o}E respectively) and at nearly opposite latitudes (21.0^{o} N and 22.2^{o} S respectively). The technical characteristics of the Learmonth radio telescope (Figure 2.6) are essentially identical to those of the Ha Noi telescope, apart from the use of a linear rather than helical feed, implying detection of the linear rather than circular component of the wave. The Learmonth observatory is staffed seven days a week from sunrise to sunset and contributes data to the US Air Force Weather Agency, to the US National Oceanic and Atmospheric Administration and to the Global Oscillation Network Group. In addition to the 2.4 m dish, it operates an 8.5 m dish (245 to 610 MHz), a 1 m dish (15.4 GHz), a swept frequency interferometric radiometer (30 to 80 MHz) and an optical telescope. Its long experience with solar measurements and its commitment to serve a large community make it a highly reliable source of data. The noise level is a factor ~1.7 lower for the Learmonth radio telescope than for that in Ha Noi.

Details about the VATLY radio telescope and its performance have been reviewed in the preceding chapter (N.V. Hiep *et al.* 2012, N.T. Phuong *et al.* 2014) and do not need to be repeated here. It is sufficient to recall that it is equipped with a fully steerable parabolic dish, 2.6 m in diameter, remotely adjustable in elevation and azimuth. It is operated at frequencies between 1400 and 1440 MHz. The reflected power is collected at focus by a left-handed helical feed, where it is locally pre-amplified, shifted to lower frequency using standard super-heterodyne, amplified and digitized. Standard data collection consists in a sequence of successive measurements of ~8.2 s duration each, digitized in the form of a frequency histogram covering ~1.2 MHz in 156 bins of ~7.8 kHz each. The telescope orientation is remotely adjustable. The angular aperture of the main lobe (the "beam") is well described by a Gaussian having a σ of 2.3^o and the pointing accuracy is measured to be 0.22^o in $a\times cos(h)$ and 0.11^o in h where a and h are the azimuth and elevation respectively. An antenna efficiency factor of ~65% has been measured, meaning a conversion factor of 1.25±0.09 K/kJy. The system temperature, including all sources of non-astronomical origin, is of the order of 200 K to 250 K.

Figure 2.6 The Ha Noi (left) and Learmonth (right) radio telescopes. The former is on the roof of a small Ha Noi building in an urban environment, the latter in an airport near the ocean. The insert shows the left-handed feed of the Ha Noi telescope. A 1 m diameter antenna is also visible on the Learmonth picture.

2.3 Data reduction

The time dependence of the measured flux emitted by a large flare is illustrated in Figure 2.7 that displays both the Ha Noi and Learmonth observations. Each measurement is averaged over the 1 MHz bandwidth. Averaging is done for us in the Learmonth case, the data being available on the web (Australian Government) at 1 second intervals in solar flux units (1 SFU=10^4 Jy). In the Ha Noi case, the measured antenna temperature is averaged over the 138 channels of a same frequency spectrum after having cleaned the data for possible radio frequency interferences (RFIs) and converted to flux density. The Ha Noi measurements are taken at intervals of ~8.17 s instead of 1 s in Learmonth. They are of the antenna temperature and are converted to SFU with a conversion factor of 12.5 K/SFU. They are used to generate a list of values available at each second by linear interpolation between successive measurements. This procedure implies that the VATLY radio telescope is blind to fine structures at the level of 1 Hz as illustrated in Figure 2.8. In both Ha Noi and Learmonth data some measurements are occasionally missing or faulty and replaced by interpolated values. The synchronism between the times at which flares are seen to occur, measured by a delay Δt between the Learmonth and Ha Noi measurements has a mean value of 1.8 s and an rms dispersion of ±3.9 s in good agreement with expectation.

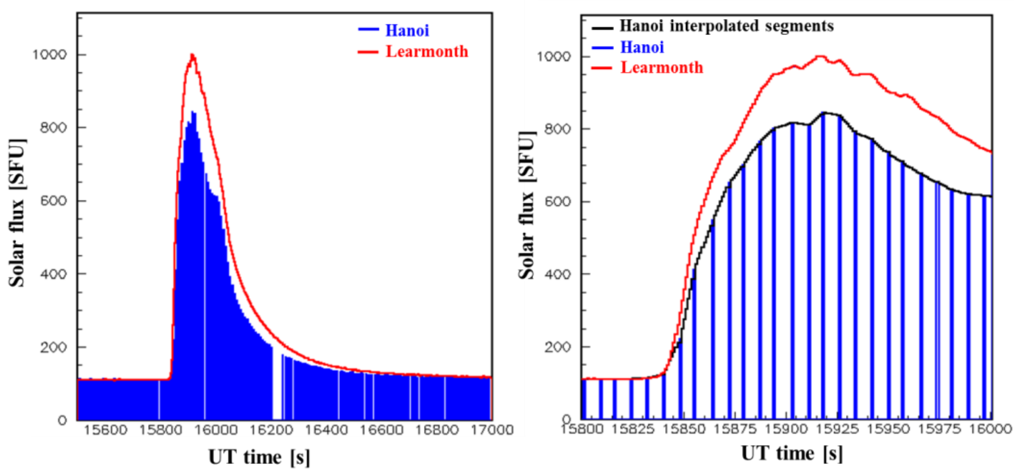

Figure 2.7 A large flare as seen in Learmonth (red) and in Ha Noi (raw data, blue). The Ha Noi data are converted to SFU using a conversion factor of 1.15 K/kJy in order to have a same quiet Sun flux density as in Learmonth. The abscissa is UT time in seconds. In the Learmonth case, there is in principle one measurement each second. In the Ha Noi case, there is, in principle, one measurement every 8.2 s or so. The right panel shows a zoom on the start of the flare, displaying in addition the interpolated Ha Noi data (black).

In most cases, the measurements of the quiet Sun flux made in Ha Noi and Learmonth are in good agreement: their ratio (Ha Noi to Learmonth) has a mean value of 0.98 and an rms dispersion of 0.07. In what follows, the Ha Noi data are normalized to the Learmonth data in an interval of a few minutes preceding the flare.

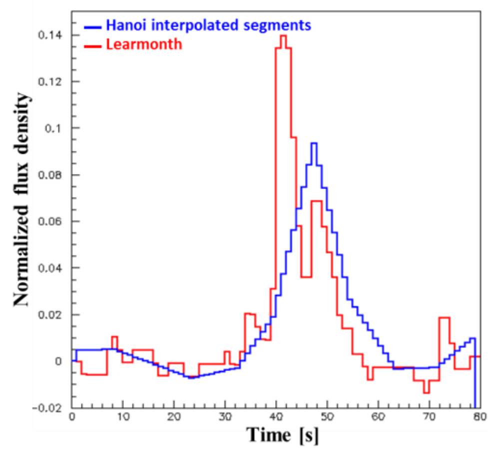

Figure 2.8 Time dependence of flare 18 displaying fine structure as detected by Learmonth (red) to which Ha Noi (blue) is blind. The quiet Sun level has been subtracted and the flux densities normalized to the flare area. Segments associated with the interpolation performed between successive Ha Noi measurements are clearly visible.

2.4 Disturbed frequency spectra

In a very few cases disagreement between the Learmonth and Ha Noi data has been observed, suggesting an anomalous functioning of the latter. We now address this issue.

Each frequency spectrum is fitted to a straight line. The quality of the fit is measured by a χ^2 evaluated for a constant relative uncertainty of 2% and normalized to the number of degrees of freedom. Its distribution is displayed in Figure 2.9 (left). We arbitrarily define as "bad fits" those having $log_{10}(\chi^2)>0.1$ ($\chi^2>1.26$). The slope of the straight line, measured in ppm per kHz, deviates by a quantity δ from its average value (slightly dependent on the central frequency, as shown in the preceding chapter); its distribution is displayed in Figure 2.9 (centre) for "good" and "bad" fits respectively. Having noticed that "bad fits" are often associated with slightly different amplitudes in each of the three sub-bandwidths, we define, for each frequency spectrum, an asymmetry α as the deviation from unity of the ratio between the mean antenna temperature measured in the central sub-bandwidth to the mean antenna temperature measured in the edge sub-bandwidths. Its distribution is displayed in Figure 2.9 (right) for "good" and "bad" fits respectively. As the data from the three sub-bandwidths are read in sequence rather than simultaneously, it is not surprising that they display differences when the signal varies significantly during the measurement. If the signal increases or decreases uniformly during the measurement, the value of δ will be affected but those of α and χ^2 will not. On the contrary, if the signal goes through a maximum or a minimum during the measurement, the value of χ^2 will be affected but those of α and δ will be less.

The distributions displayed in Figure 2.9 show that the system is usually well behaved. In particular, the slope of the frequency spectrum is mostly Gaussian distributed with an rms of only 9 ppm/kHz. While the "bad" fit values of δ span a broad range, those of α are confined to large values. Indeed, all spectra having $log_{10}(\chi^2)<0.1$ ($\chi^2<1.26$) have $log_{10}(\alpha)<-1.4$ ($\alpha<0.04$). This strong correlation between α and χ^2 is confirmed in Figure 2.10 where the two quantities are plotted together for the 94 spectra (out of 4995) having $log_{10}(\chi^2)>0.1$. It implies that the main cause of deterioration of the quality of the fit is related with different flux densities recorded in each of the sub-bandwidth, and therefore a consequence of rapid changes of the signal level.

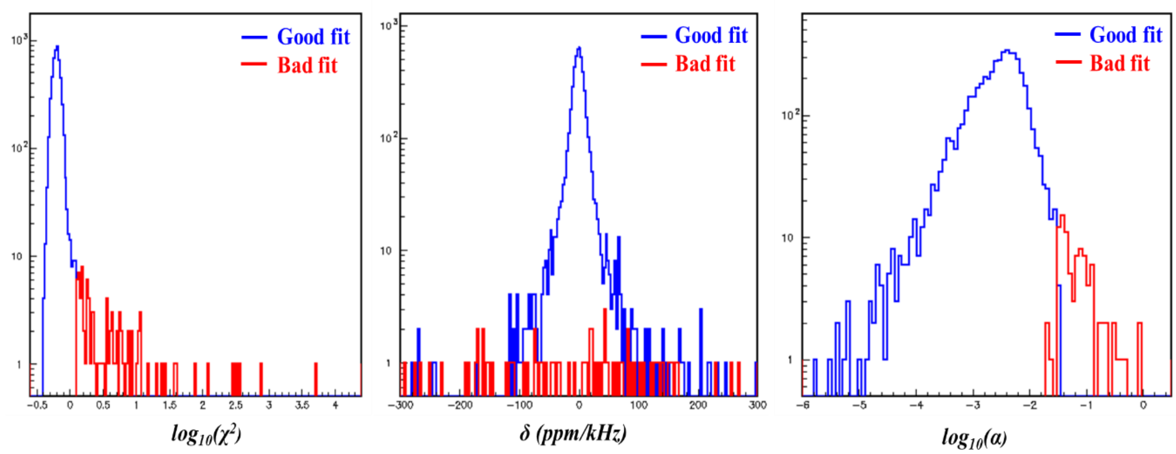

Figure 2.9 Distributions of $log_{10}(\chi^2)$ (left), of δ (in ppm/kHz, middle) and of $log_{10}(\alpha)$ (right). "Good" and "bad" fit values are shown in blue and red respectively. Log scales are used for the ordinates.

In most "bad" fit cases, the dissymmetry between the central and edge sub-bandwidths, which is responsible for the large value of χ^2, is rather modest. A value of α equal to 0.2 ($log_{10}(\alpha)=-0.7$) typically means an error of only ~7% on the flux density. We inspected by eye all spectra having $log_{10}(\chi^2)>0.5$ in order to unveil possible dysfunctions of a different nature. This resulted in a sample of 45 measurements (out of a total of 4995) associated with 9 flares. Figure 2.11 displays the four profiles including the spectra having the larger values of χ^2. As expected, the steepness of the variation of the detected flux is a more important parameter than the flare amplitude in producing "bad" fits.

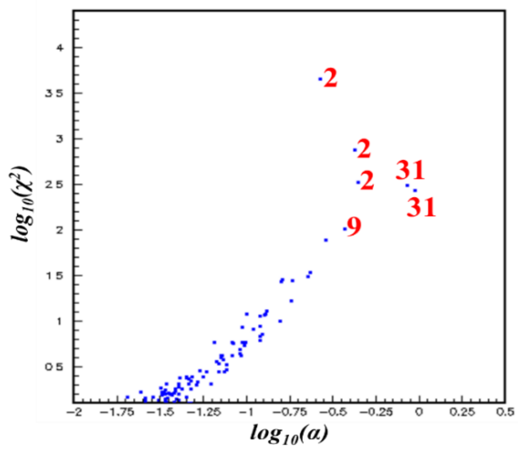

Figure 2.10 Two-dimensional plot of $log_{10}(\chi^2)$ (ordinate) *vs* $log_{10}(\alpha)$ (abscissa) for "bad" fits. Flares having the larger values of χ^2 are labelled as in Figure 2.11

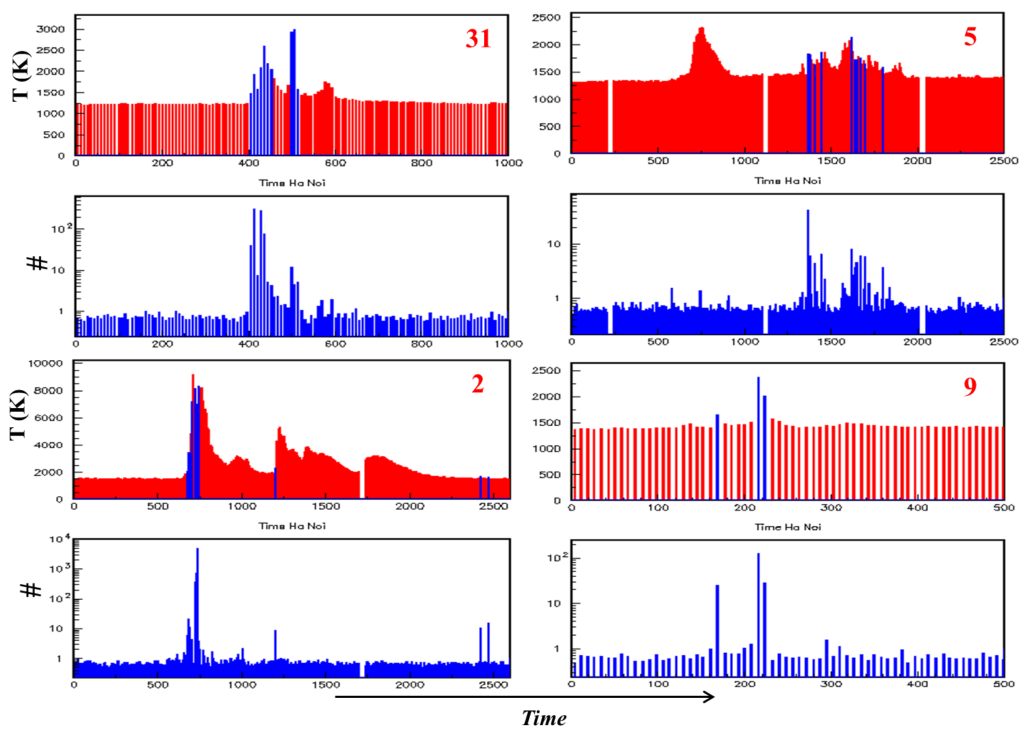

Figure 2.11 The four flares having frequency spectra with the larger values of χ^2. Each flare is illustrated by two panels, the top one displaying the variation of the antenna temperature *vs* time (in seconds) and the lower one displaying the variation of χ^2. In the upper panels, measurements having $\chi^2>\sqrt{10}$ are shown in blue.

A sequence of frequency spectra, displaying particularly strong δ and α variation, is displayed in Figure 2.12. It illustrates well how "bad" fits are normally associated with important dissymmetry between the three sub-bandwidths. Of the 45 spectra inspected by eye, only three display severe dysfunctions going beyond a simple sub-bandwidth asymmetry. They are associated with the largest flare, labelled 2 in Figures 2.10 and 2.11, and are displayed in Figure 2.13.

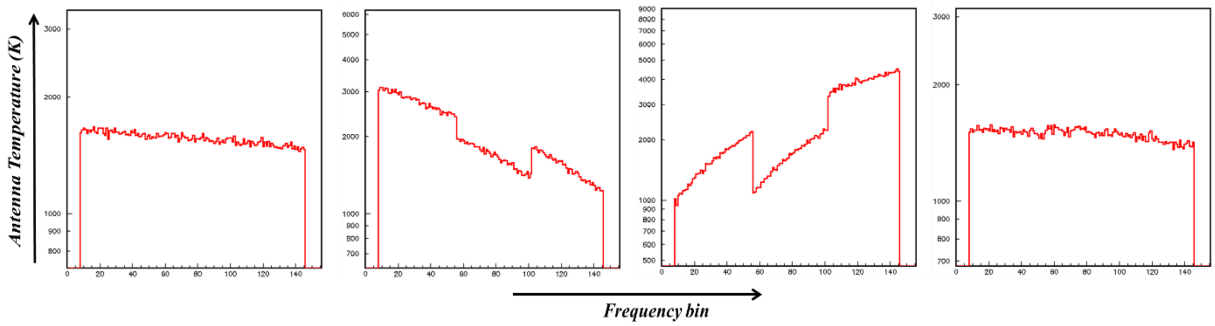

Figure 2.12 Frequency spectra of a sequence of four successive measurements, the two central being "bad" fits (taken from flare 5).

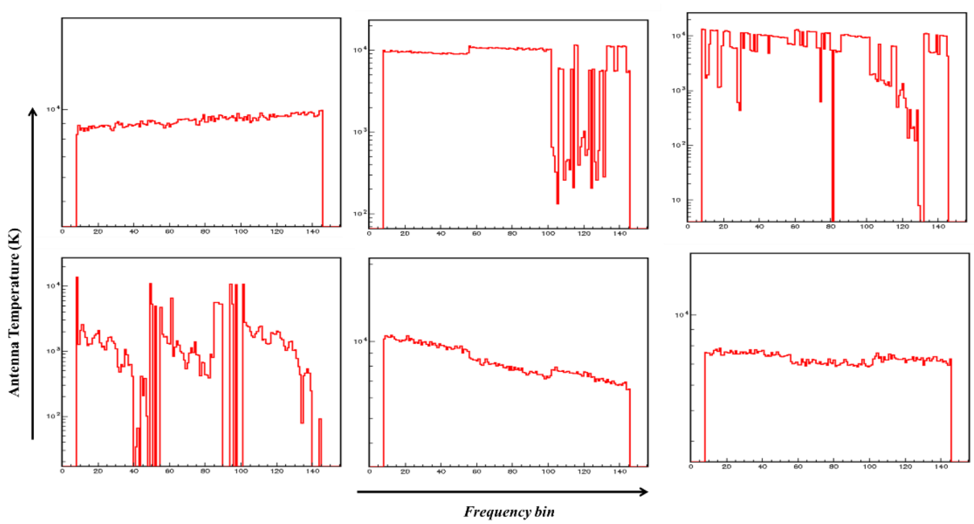

Figure 2.13 Frequency spectra of the only sequence of measurements displaying dysfunctions of another type than simple fluctuations of δ and α. They are taken from flare 2 data.

In conclusion, in the vast majority of measurements, the instrument is well behaved and the evaluation of the antenna temperature is reliable to a precision of a few percent. In a few cases where the signal varies rapidly, the frequency spectrum has a slope that differs significantly from average and/or displays significant differences between the level of the central sub-bandwidth and that of the edge sub-bandwidths.

However, this affects only modestly the flux density measurement. Only in the extreme case of three measurements of the largest flare (#2) spectra showing severe dysfunction (Figure 2.13) have been excluded from the subsequent analysis.

2.5 Comparison between Ha Noi and Learmonth observations

We now compare the flare data collected in Ha Noi with those collected in Learmonth. In spite of the strong similarity between the profiles obtained by the two observatories, significant differences are present, which ask for an explanation. As a working hypothesis, we take the Learmonth observations as reference and accept that the Ha Noi measurements may suffer instrumental problems, but we assume that perfect instruments should observe identical profiles. This is only true in the absence of polarization. While the Learmonth telescope will generally catch half of the power collected by the dish, the Ha Noi telescope may catch it all if the wave is right-handed but will catch nothing if the wave is left-handed. A possible influence of the ionosphere, which is in quite different states in Ha Noi and at Learmonth, is supposed to be negligible at our frequency.

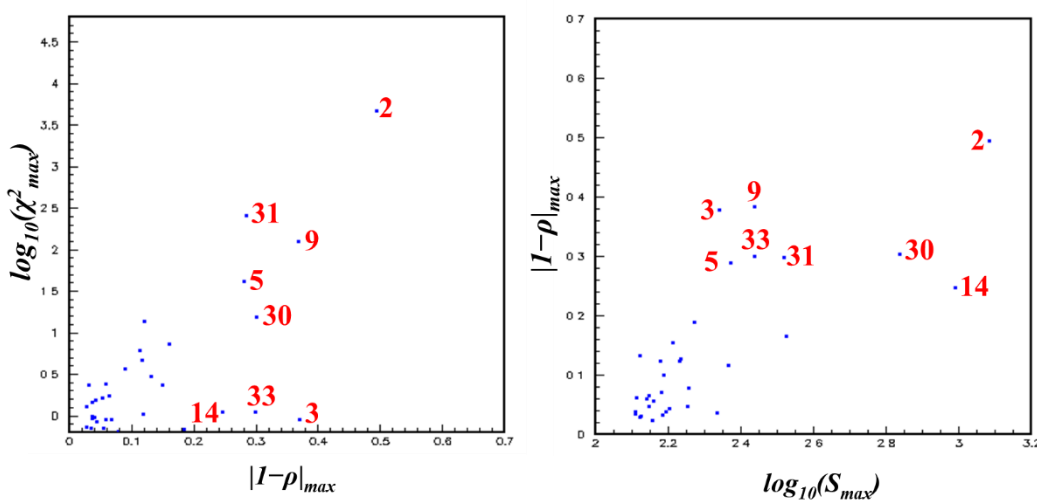

Figure 2.14 Left: distribution of $log_{10}(\chi^2_{max})$ (ordinate) *vs* $|1-\rho|_{max}$ (abscissa). Right: distribution of $|1-\rho|_{max}$ *vs* $log_{10}(S_{max})$

In order to reveal possible differences between Learmonth and Ha Noi observations, we evaluate the ratio $\rho=S_{HN}/S_{LM}$ of the Ha Noi to Learmonth flux densities as a function of time and look for significant deviations from unity. We observe that important deviations are usually associated with large flares and with flares having disturbed frequency spectra, as discussed in the preceding section. We measure the latter by the maximal value χ^2_{max} taken by χ^2 (defined in the preceding section); similarly, we measure the deviation of ρ from unity by the maximal value $|1-\rho|_{max}$ that it takes over the flare and the strength of the flare by the maximal value S_{max} taken over the flare by the flux density measured in Learmonth. Distributions of these parameters are displayed in Figure 2.14. Eight flares are seen to have $|1-\rho|_{max}$ in excess of 0.2. Of these, three (2, 14 and 30) are the stronger flares in the sample. Figure 2.15 (left) displays the distribution of $log_{10}(S_{HN})$ *vs* $log_{10}(S_{LM})$ for all flares. Flares 3, 30 and 2 deviate significantly from the mean. While flares 2 and 30 are among the stronger, flare 14, which is equally strong, displays no significant deviation, excluding effects caused exclusively by the amplitude of the signal, such as saturation of the electronics.

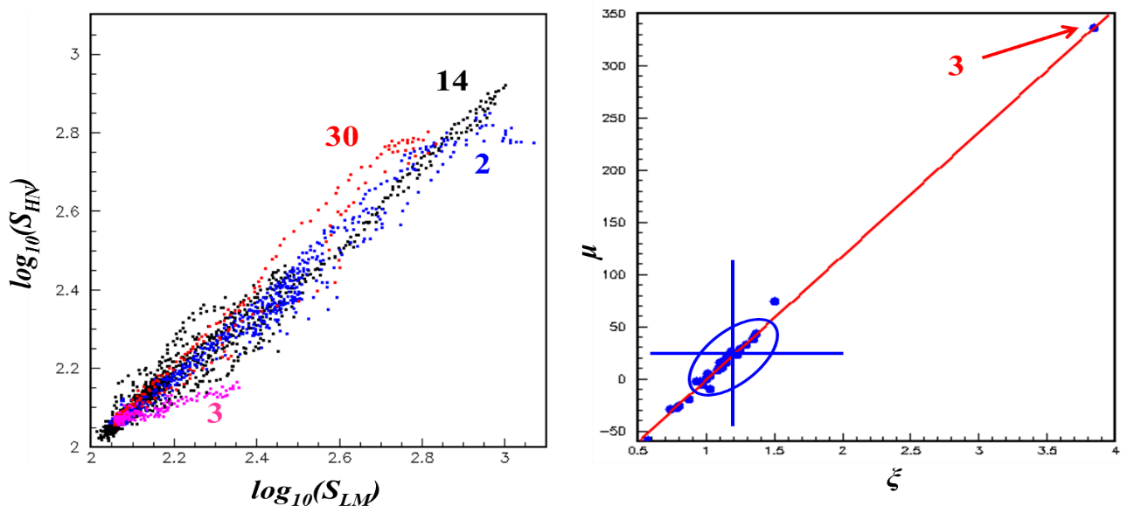

Figure 2.15 Left: Distribution of $log_{10}(S_{HN})$ *vs* $log_{10}(S_{LM})$. Right: Distribution of μ *vs* ξ. The line is for S_0=119 SFU. The cross indicates the expected average values. The ellipse indicates the set of measurements used to evaluate the quantity $\delta\xi$ in the next section.

Small deviations between the Ha Noi and Learmonth observations could be due to small differences in gains and/or system temperatures. In general, without knowing the gains and system temperatures of the two instruments, we may write $S_{LM}=\xi S_{HN}-\mu$ where $\xi-1$ and μ measure possible differences in gain and system temperature. As the two flux densities were normalized before the flare to a single value S_0, ξ and μ must obey the relation $\mu=(\xi-1)S_0$ if a good fit is to be obtained before the flare. For each profile, we can find the values of $\xi-1$ and μ that give the best fit between the two sets of data. If they deviate only slightly from zero, the accuracy with which the system temperature and the gain of the Ha Noi telescope have been evaluated can be blamed. However, some of the values taken by ξ and μ, displayed in Figure 2.15 right, are too large for such an explanation. While showing the expected correlation and a nucleus of concentration around $\xi \sim 1.2$ and $\mu \sim 20$, as expected for a Ha Noi system temperature of ~220 K and a quiet Sun level of ~120 SFU, they reveal the existence of significant deviations. Particularly spectacular is the case of flare 3, a small flare that followed flare 2 one hour later, which stands out far away from the other flares.

2.6 Interpretation in terms of polarized flare emission

The analyses of the preceding sections have not revealed any dysfunction of the Ha Noi telescope and have given confidence in the reliability of its observations, an invitation to consider seriously the possibility that the differences between the Ha Noi and Learmonth observations are due, at least in part, to the polarization of the flare emission.

Indeed, important polarizations are common in the radio emission of solar flares and are routinely recorded in solar observatories such as Nobeyama[10] in Japan. Models of the relevant mechanisms are available in the literature (M. Karlicky & M. Barta, 2004).

In order to compare flare emissions rather than total emissions, we define for each flare a profile F obtained by subtracting the quiet Sun signal from the total detected signal. In order to reduce errors resulting from a possible time shift between the Learmonth and Ha Noi data, we use time bins of 10 s instead of 1 s. The quiet Sun signal is obtained by linear interpolation between the signals measured before and after the flares. We checked that using instead a constant quiet Sun signal, as measured before the flare, would not significantly affect the results because the quiet Sun levels before and after a flare are very close to each other.

We obtain the polarization P of the flare emission from the ratio between the flux densities of the flare emissions measured in Ha Noi and Learmonth,

$$\frac{F_{HN}}{F_{LM}} = \frac{2R}{R+L} = 1 + \frac{R-L}{R+L} = 1 + P \qquad (2.1)$$

where, R and L stand for the right-handed and left-handed flux densities respectively.

Subtracting the quiet Sun signal from the total signal to obtain the flare signal implies that the system temperature drops out from the evaluation of the flare emission. However, when we normalize the pre-flare quiet Sun flux measured in Ha Noi to that measured in Learmonth to ease the comparison between the two sets of data, this

[10] http://solar.nro.nao.ac.jp/norh/html/event/

operation depends slightly on the system temperature assumed for the Ha Noi telescope, which we take equal to 215±30 K. The uncertainty of ±30 K translates in a first uncertainty on the value of P. A second uncertainty results from a possible time shift between the Ha Noi and Learmonth measurements, which we take as ±4 s. Both uncertainties may be very small in the case where the polarization is small. In particular, they essentially cancel in the quiet Sun regime. In order to account for possible inaccurate evaluations of the system temperature and gain of the Ha Noi telescope with respect to those of the Learmonth telescope, we introduce a third uncertainty evaluated from the concentration of events displayed in Figure 2.15 (right). Assuming that their dispersion, $\Delta\xi$~9%, is purely instrumental, namely that the associated flares are unpolarized, we find that the uncertainty $\delta\xi$ on ξ translates in a same uncertainty δP on P. We take as global uncertainty ΔP the quadratic sum between the three contributions. To the extent that part of the two former contributions contribute to the third, this is a conservative evaluation of the global uncertainty. It is also conservative to the extent that part of the value of $\Delta\xi$ is likely to be due to polarization (which is not expected to exactly cancel).

Another cause of error is a possible imperfect design of the Ha Noi feed. Indeed, while its circumference is equal to the wavelength as it should, its pitch is only 3 cm instead of the quarter wavelength (5.3 cm) expected. There exists an abundant literature on helical antennas (J.D. Kraus 1995 and 1950, J.D. Kraus & R.J. Marhefka 2002, see also http://www.w1ghz.org/antbook/conf/Helical_feed_antennas.pdf and references therein for an excellent summary) but we were unable to find a reference commenting on the purity of the handedness of the detected wave. Assuming that the Ha Noi telescope detects a fraction $\varepsilon>0$ of the left-handed component of the incident wave, the polarization P' measured as $F_{HN}/F_{LM}-1$ reads $P'=(1-2\varepsilon)P$. To the extent that $\varepsilon<<1$, a reasonable assumption, the effect is simply to lower the amplitude of the polarization by a constant factor.

Flare 33, a C3.9 flare peaking at 140 SFU above quiet Sun, displays an apparent time mismatch of ~10 s between Learmonth and Ha Noi. Such mismatch may occasionally happen (Owen Giersch, private communication) and makes flare 33 unsuitable for a reliable polarization measurement. We retain for further scrutiny any other flare either having an unpolarized flux density (F_{LM}) in excess of 100 SFU or displaying large significant values of P. Precisely, we define as reliable polarization measurements those having both $\Delta P<15\%$ and F_{LM}>25 SFU. Two M flares, flares 31 and 9, display too rapid flux density variations to obey these constraints. This leaves flares 30, 2, 3, 5, 14, 15 and 21 for further scrutiny.

The main parameters (NASA[11], TESIS[12], NOAA[13], MONTANA[14]) of the retained flares are listed in Table 2.1 and their profiles are displayed in Figure 2.16. The measured polarizations *P* of the flare emission are displayed in Figure 2.17.

The pair of flares 2+3 is particularly spectacular. Flare 2 is an X1.7 flare that erupted from active region 1882, just after it had emerged from the eastern limb of the Sun (Figure 2.18 left). It displays a rich time structure. It was followed seven hours later by an X2.9 flare erupting from the same Sun spot, too late however to have been caught by our and Learmonth telescopes. Flare 3 erupted about one hour after flare 2 and reaches very large *P* values. Measurements made at Learmonth at other frequencies (Figure 2.18 right) show that it is not seen at frequencies in excess of ~2 GHz while the brightness of flare 2 keeps slowly rising with frequency, giving evidence for their very different natures.

Table 2.1: Flare properties

Label	30	2	3	5	14	15	21
Date (ymd)	*120703*	*131025*	*131025*	*131028*	*131108*	*131110*	*131207*
Starting (UT)	*3:36*	*7:53*	*9:01*	*4:41*	*4:20*	*5:08*	*7:17*
Class	*C9.9*	*X1.7*	-	*M5.1*	*X1.1*	*X1.1*	*M1.2*
Max(F_{LM}) [kSFU]	*~ 0.45*	*~ 0.90*	*~ 0.10*	*~0.09*	*~ 0.85*	*~0.18*	*~0.08*
Max(P) [%]	*~ +30*	*~ –30*	*~ −70*	*~+10/−10*	*~ –20*	*~0*	*~0*
Nobeyama	*yes*	*No*	*no*	*yes*	*yes*	*yes*	*no*
Active region	*1515*	*1882*	*1882*	*1875*	*1890*	*1890*	*1909*

[11] http://www.nasa.gov/content/goddard/sun-emits-2nd-solar-flare-in-2-days/TESIS
[12] http://www.tesis.lebedev.ru/en/about_tesis.html
[13] http://www.swpc.noaa.gov/ftpmenu/warehouse/2013.html
[14] http://solar.physics.montana.edu/max_millennium/data_archives.shtml

In both Learmonth and Ha Noi, the quiet Sun antenna temperature returns to its original level between flares 2 and 3 and after flare 3. Flare 3 stands out (Figure 2.15 left) as being in particularly strong disagreement between the two observatories, implying that at least one of the two telescopes responds differently to emission from the flare and emission from the quiet Sun. Another way to illustrate the puzzling situation of flare 3 is from its position in the μ *vs* ξ plot of Figure 2.15 right, showing that no sensible values of the gain and system temperature can be invoked to explain the effect.

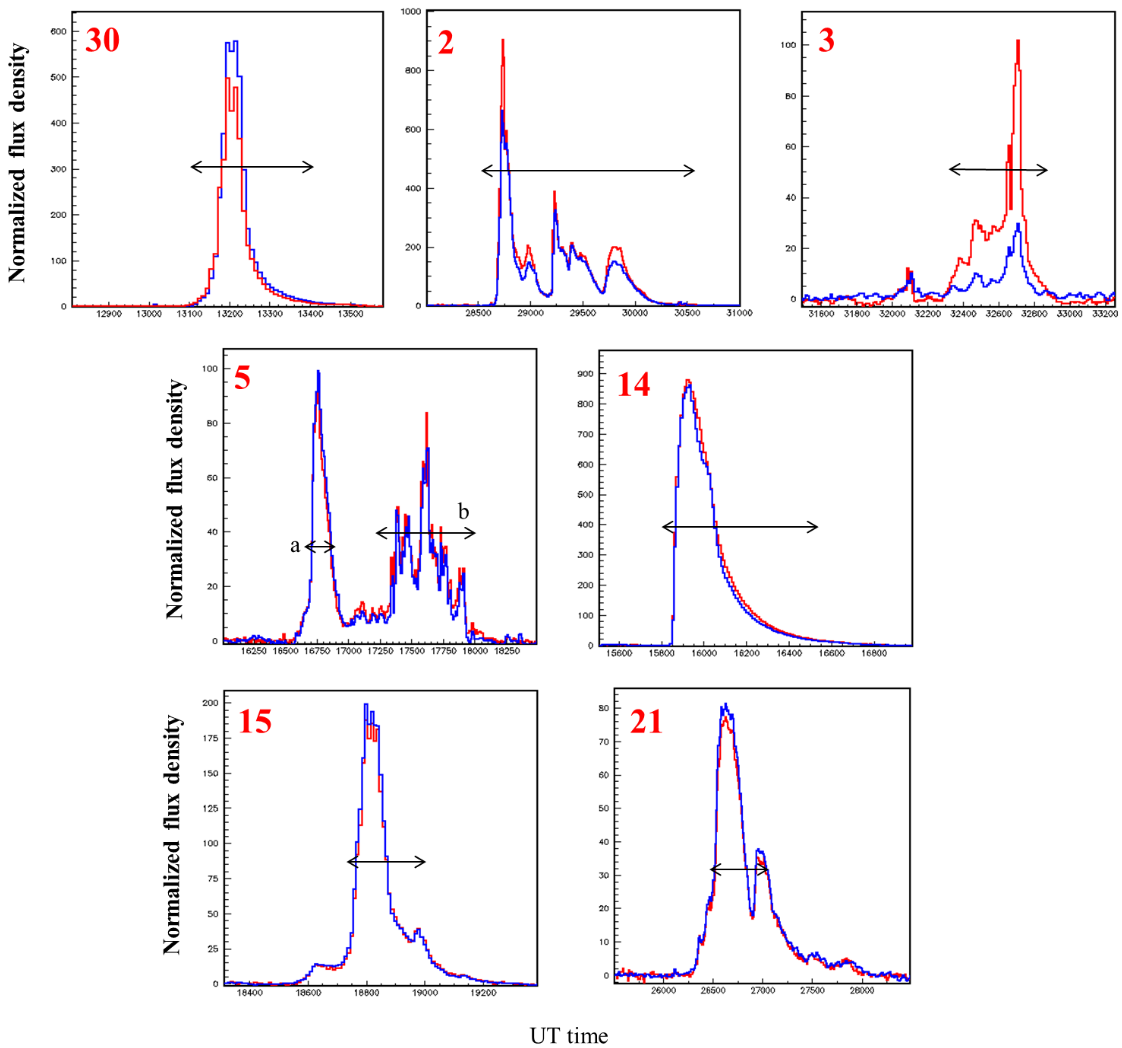

Figure 2.16 Flare profiles as measured in Learmonth (red) and Ha Noi (blue). The arrows indicate the intervals over which polarization is displayed in Figure 2.17 as being reliably measured. Time is UT in seconds

Figure 2.19 compares the flux densities of flares 2+3 measured in Learmonth and in the solar observatory of San Vito dei Normanni[15], in southern Italy. This observatory operates radio telescopes essentially identical to those at Learmonth. The Learmonth and San Vito measurements, when simultaneously available, are in good agreement. This is likely to exclude possible effects of the Hanbury Brown-Twiss type (R. Hanbury Brown & R.Q. Twiss 1956) causing important differences between the two observatories on one hand and Ha Noi on the other.

Major radio bursts, of the Tenflare type[16], meaning more than twice quiet Sun at 10 cm wavelength, were active during the periods covered by flares 2, 3 and 14. While ionospheric activity is expected to be much stronger in Ha Noi than in Learmonth and San Vito because of its exceptionally high S4 scintillation index (IPS(2012b)), this should not affect differently the quiet Sun and flare contributions.

Delayed decimetric bursts displaying a very high degree of circular polarization have been previously observed and examples of unusually strong such events are described in the literature (E.W. Cliver et al. 2011).

Flare 14 is an X1.1 flare, accompanied, as was Flare 2, by important Coronal Mass Ejection, a type II/IV sweep frequency event and a Tenflare radio burst. However, it is single-peaked at strong variance with Flare 2.

Flare 30, contrary to flares 2 and 14, is weak in X-ray emission. Flares 5, 15 and 21 are weaker and are consistent with being unpolarized.

Four of the flares listed in Table 2.1, flares 30, 5, 14 and 15, have been detected by the Nobeyama solar polarimeters. Unfortunately, the Sun had set in Japan when the pair of flares 2+3 erupted. The Nobeyama polarimeters operate at 1 and 2 GHz, providing two frequencies bracketing the Ha Noi/Learmonth frequency. Figure 2.17 compares the polarizations measured in Nobeyama with those obtained in the present work. The steep and irregular frequency dependence of the polarization of flare emissions, as observed in Nobeyama, makes a comparison difficult. Yet, the mismatch between Nobeyama and Ha Noi/Learmonth data on flare 30 is a cause of concern shedding doubts on the validity of our evaluation. None of the effects that have been considered until now can be blamed for such poor agreement.

---

[15] http://www.ngdc.noaa.gov/stp/ space-weather/solar-data/solar-features/solar-radio/rstn-1-second/san-vito/2013/

[16] Space Weather Highlights, SWPC PRF 1991, 28 October 2013, http://www.swpc.noaa.gov/weekly/2013_WeeklyPDF/prf1991. pdf

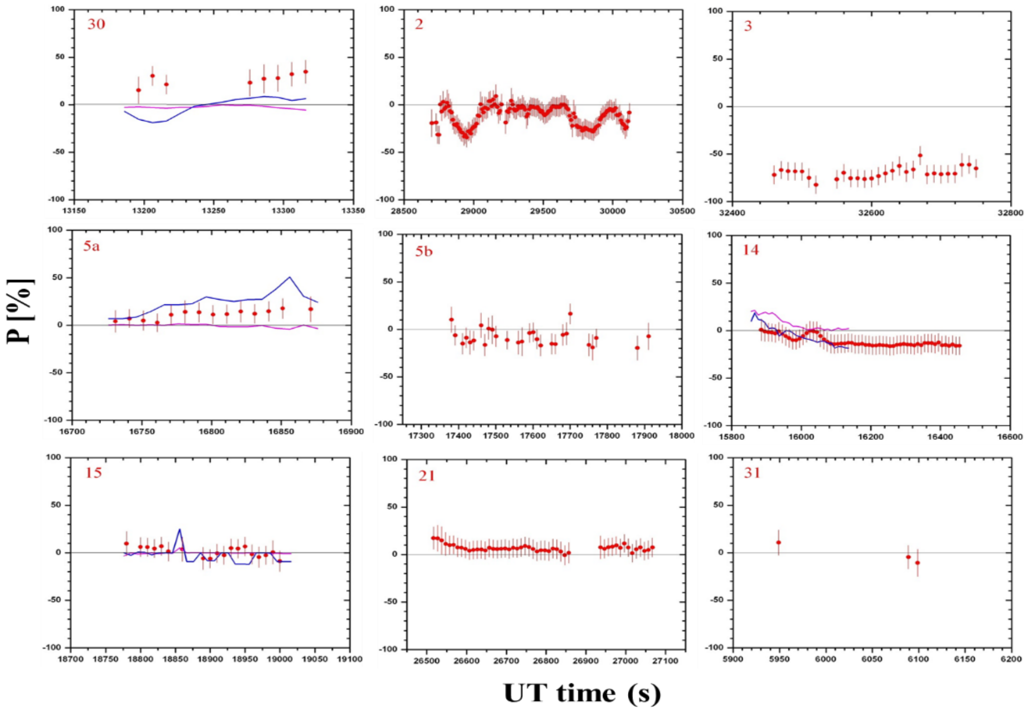

Figure 2.17 Polarizations measured for the flares listed in Table 2.1 (red) over the time intervals where reliable measurements are available (as indicated in Figure 11). Nobeyama polarizations (blue) measured at 1 GHz (magenta) and 2 GHz (blue) are shown when available. Also shown is the polarization of flare 31, a M2.9 flare peaking at ~280 SFU, which erupted from active region 1515 on July 6th, 2012 and was measured unpolarized in Nobeyama

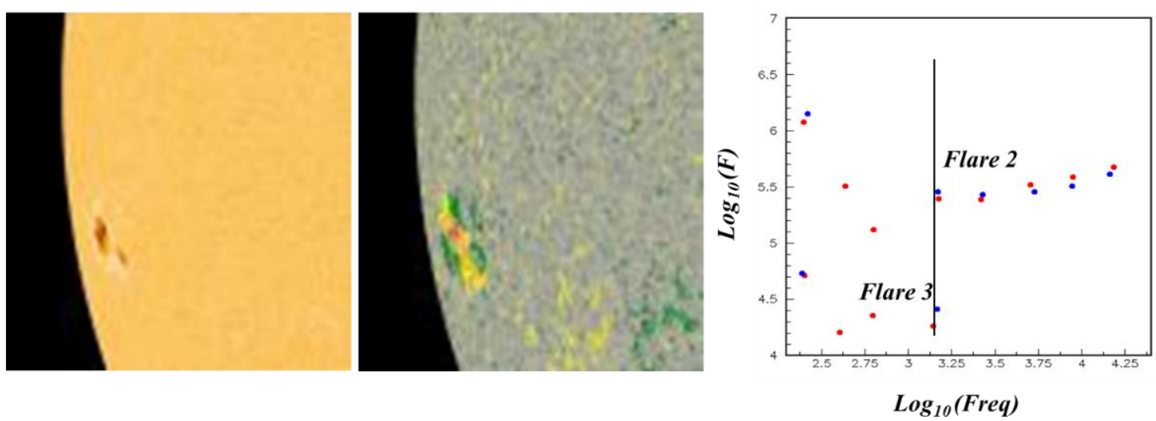

Figure 2.18 Left: Optical map and magnetogram of Sun spot 1882 from where flares 2 and 3 erupted. Right: Distribution of the decimal logarithm of the integrated flux densities (SFU) measured in Learmonth for flares 2 and 3 at Learmonth (red) and San Vito (blue) as a function of the decimal logarithm of the frequency (MHz). Flare 3 is undetected beyond 2 GHz. The line is at 1.42 GHz.

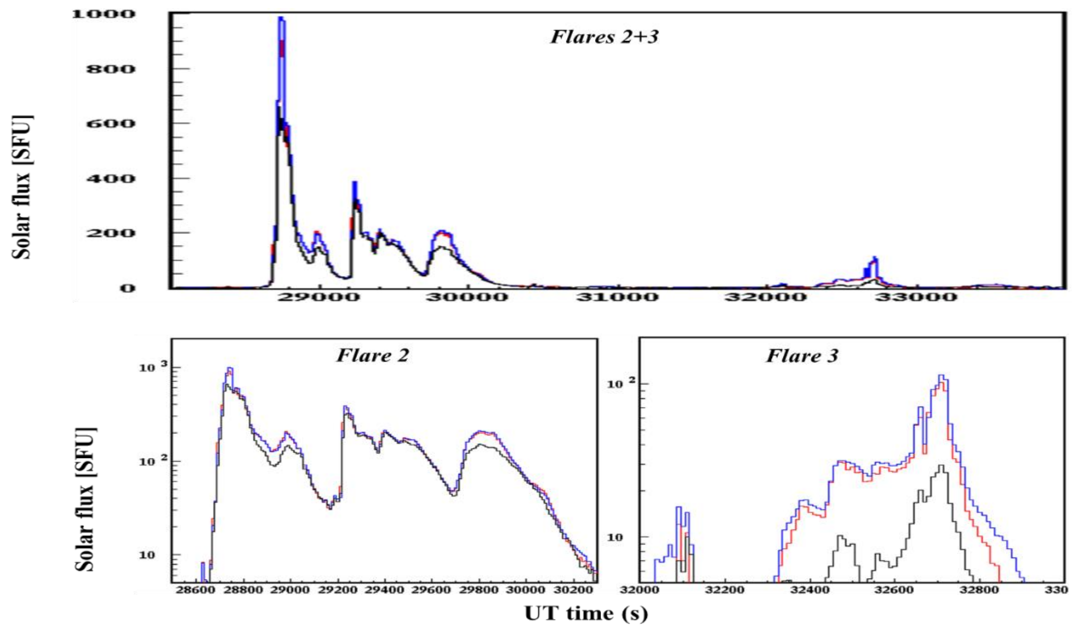

Figure 2.19 Comparison between the flux densities (SFU) measured in Learmonth (red), San Vito (blue) and Ha Noi (black) for the pair of flares 2+3. In many cases the Learmonth and San Vito values are indistinguishable

2.7 Summary

We have studied 34 solar flares that have been observed simultaneously in Ha Noi and Learmonth; we have compared their profiles as measured in the two observatories with the aim to reveal possible instrumental effects affecting the Ha Noi telescope.

A first result is the observation of disturbances of the frequency spectra measured in Ha Noi that are strongly enhanced by the presence of solar flares. Such disturbances had already been observed as associated with radio frequency interferences or transients on the line. They consist in inequalities of the fluxes detected in each of the three sub-bandwidths that are stitched together to produce the total bandwidth and are associated with rapid variations of the detected signal. In most cases, they only have a small incidence on the accuracy of the measurement of the antenna temperature. In a very few cases, however, they cause the system to fail completely (three such measurements were found in the sample under study and have been illustrated in Figure 2.13).

A detailed study has revealed the presence, in several cases, of significant differences between the flux densities measured in Ha Noi and Learmonth. Some of these have been identified as being the result of the different time resolutions of the two telescopes. A few others have been interpreted as giving evidence for significant polarization of the flare emission. However, comparison with measurements made at Nobeyama failed to give strong support to this interpretation. Particularly spectacular is the case of a small flare, peaking at ~100 SFU above quiet Sun and following an X1.7 flare after a delay of ~1 hour, which displays a polarization of ~70%. In this case, the fact that the quiet Sun fluxes measured before, in between and after the pair of flares are in very good agreement between Ha Noi and Learmonth makes it very difficult to invoke another effect than a strong polarization of the flare emission.

CHAPTER 3

RADIO OBSERVATION OF mHz OSCILLATIONS

3.1 Overview and early observations

The observation of the Sun between mid-April and early September 2012 revealed the occasional presence of mHz oscillations. A first question that has been asked was whether such oscillations are also observed by other observatories. The existence of the Learmonth Australian observatory, which was introduced in the preceding chapter, was therefore exploited for this purpose.

3.1.1 Observation of correlated mHz oscillations

The Sun was observed on-the-fly between mid April and early September 2012 at a frequency of 1.415 GHz (namely slightly below the 21 cm hydrogen line) and the data were compared with data from the Learmonth observatory taken at the same frequency during the same period (IPS 2012a). They were in general good agreement, both displaying oscillations in phase with the ~28 day rotation period of the Sun, maxima exceeding minima by ~50% and occurring around June 10th, July 8th, August 5th and September 2nd, revealing an important longitudinal asymmetry of the Sun activity.

It was noted that oscillations at the percent level were occasionally present in both the Learmonth and Ha Noi data, with typical periods of five to seven minutes. Figure 3.1 displays two such examples.

A set of 304 time intervals in which both the Ha Noi and Learmonth data were seen to display such oscillations was then selected. In each time interval, the Ha Noi and Learmonth data were fitted to a form (Figure 3.2)

$$S(t) = P(t) + A(t) sin(2\pi t/T + \varphi) \tag{3.1}$$

and the result was carefully scrutinized to finally retain 124 intervals where both Ha Noi and Learmonth data were properly described by this form. Examples are given in Figure 3.3. The definition of "properly described" was somewhat arbitrary and could not be simply quantified, for example by using a cut on the best fit value of χ^2. This difficulty was kept in mind and taken in due account.

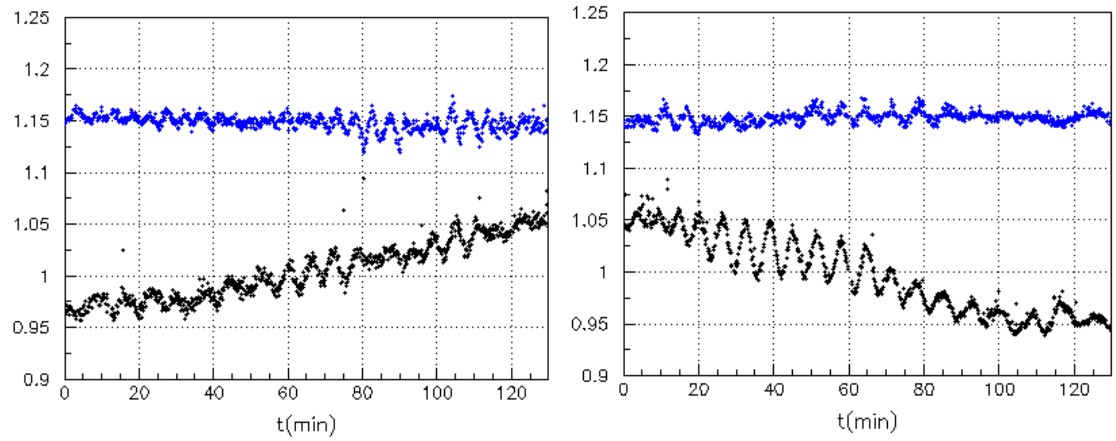

Figure 3.1 Two examples of oscillations simultaneously observed in Learmonth (upper traces) and Ha Noi (lower traces). Flux densities are normalized to unity (the Learmonth data have been shifted up by 15% for clarity)

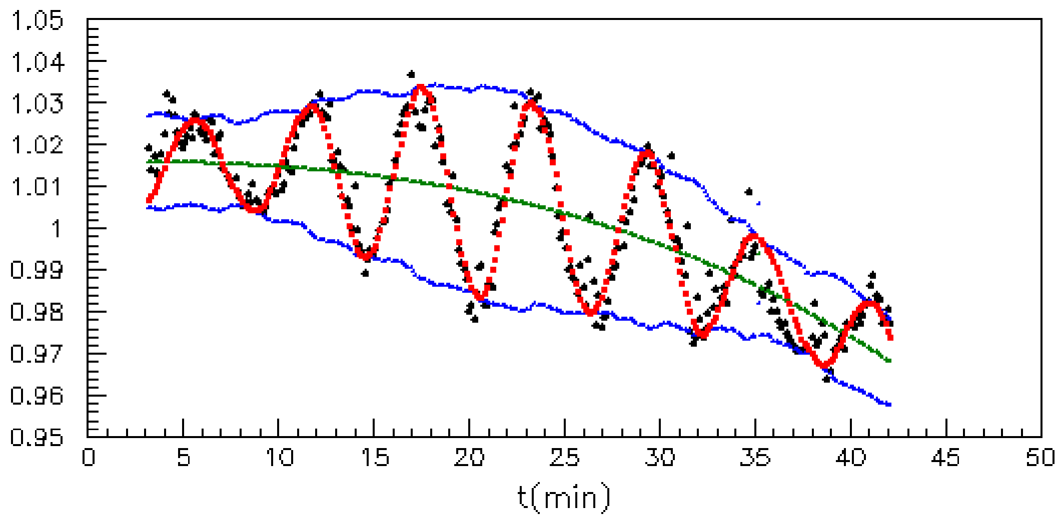

Figure 3.2 Fitting procedure: the data (dots) are first fitted to a third degree polynomial (central curve) over the whole interval. Their rms deviation from this polynomial, averaged over a 6 min sliding interval, defines the oscillation amplitude (outer curves), leaving two 3 min wide dead regions at the extremities of the time interval. In a last step, the period and phase of the oscillation are adjusted to minimize the value of χ^2 (dotted curve).

The reliability of the selection was investigated without revealing anomalies and correlations between the Ha Noi and Learmonth data were searched for with the result that a very significant correlation was observed between the periods of the oscillations, at variance with other quantities. Figure 3.4 (left) displays the distribution of time intervals in the plane (T_L,T_H) where T_L and T_H are the Learmonth and Ha Noi periods respectively. The periods of the oscillations are strongly correlated, the non-correlation hypothesis being rejected to an extremely high degree of confidence (a χ^2 of 106 for 25 degrees of freedom). As the figure suggests the presence of two distinct families of intervals separated by the line of equation $T_L=2.2T_H-9.2$ *min*, the analysis was then restricted to the more populated family (105 intervals) having T_L larger than this limit. It was found that while the oscillations observed in Learmonth and Ha Noi have similar periods on average, the spans that they cover differ significantly. A detailed study of the data retained did not reveal any anomaly and both Ha Noi and Learmonth oscillations were found to display, on average, a clear sine wave behaviour (Figure 3.4, right).

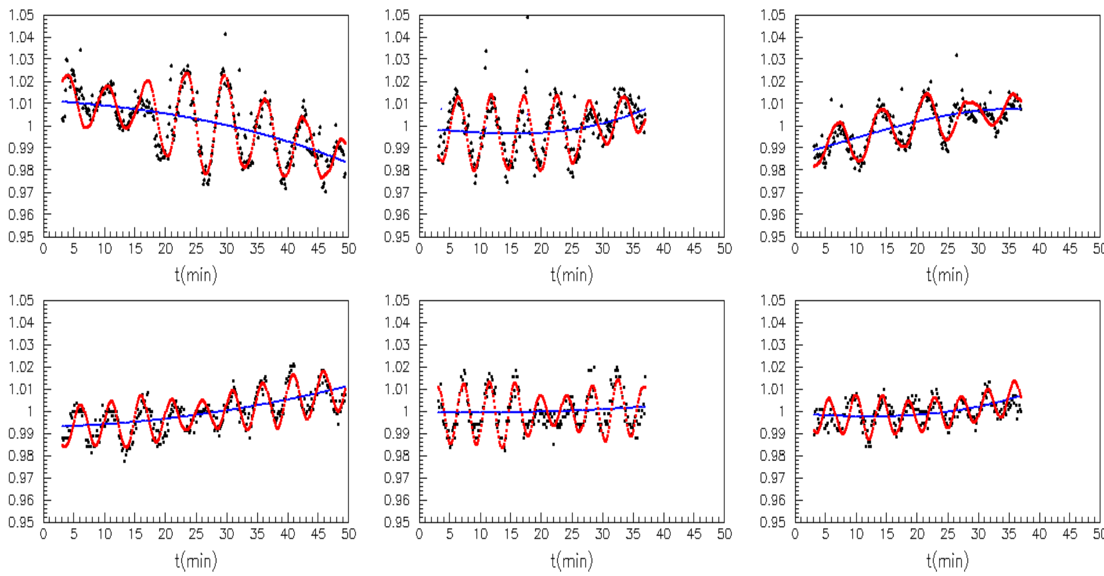

Figure 3.3 Three examples of selected intervals (Ha Noi data in the upper and Learmonth data in the lower panels). The curves show the polynomial and sine wave best fits

3.1.2 Search for possible instrumental effects

As a check of the solar origin of the observed oscillations, data had been taken by pointing the telescope 15° off the Sun; the absence of observed oscillations allows for placing an upper limit of 0.3 % on their possible relative amplitudes. Simple instrumental effects, such as resulting from electronics faults, e.g. saturation of electronics components, had been excluded. Generally, the evidence for a strong positive correlation between the periods of the oscillations observed in Ha Noi and at Learmonth seemed to exclude an interpretation in terms of simple instrumental effects. Nevertheless, it was remarked that the similarity between the two instruments implies that they suffer from similar biases or weaknesses, which might result in such positive correlations and in our misinterpretation of what they hide.

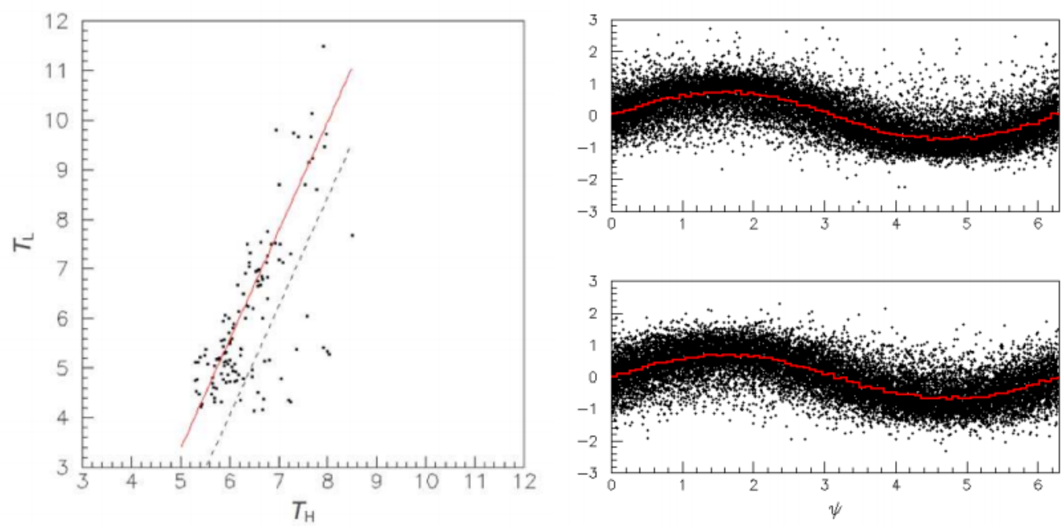

Figure 3.4 Left: Distribution of selected intervals in the [T_L,T_H] plane. The red line shows the best fit to the more populated family. The separation between the two families is indicated as a black line. Right: Shapes of the oscillations observed in Ha Noi (upper panel) and Learmonth (lower panel); the quantity $\{S(t)-P(t)\}/A(t)$ is displayed as a function of $\psi=2\pi t/T+\varphi$ modulo(2π) for the Ha Noi and Learmonth data separately The lines indicate the average wave forms.

Such a possible source of erroneous interpretation was suggested by Dr. Owen Giersch (O. Giersch, private communication) as arising from multipathing, namely interferences between the direct solar signal and its reflection on a nearby obstacle (building, ground, etc.). Multipathing would indeed be Sun associated and result in different oscillation amplitudes and periods in Ha Noi and at Learmonth because of their different local environment. For an obstacle at a distance D in a direction making an angle ω with the Sun, the path difference is $D(1\text{–}\cos\omega)\sim\frac{1}{2}D\omega^2$ as ω must be small enough for both the direct and reflected signals to be contained in the beam. Typically, $\omega\sim0.1$ rad and $d\omega/dt\sim3$ mrad/min. For the period $T=\lambda/(D\omega d\omega/dt)$ of typical multipath oscillations to be in the 6 min range, D needs therefore to be in the 100 m range which is a reasonable value for possible nearby obstacles. Moreover, such oscillations would be observed for the time it takes the Sun to sweep across an angle of the order of the beam aperture, namely a fraction of an hour.

Multipathing appeared therefore as a serious candidate to account for our observations. An important argument against it was the observation of the strong correlation between the periods of the oscillations measured at Learmonth and in Ha Noi. A crucial test of the multipathing hypothesis would have been the observation that it occurs preferentially when the Sun is low on the horizon. Splitting the distribution of elevations in three equally populated bins, 0^o to 52^o, 52^o to 62^o and 62^o to 90^o, the fractions of category 2 intervals are respectively 31±6 %, 64±8 % and 24±5 %. While this clearly excluded an excess of low elevation occurrences, as would be expected from multipathing involving obstacles on ground, it displayed a significant excess at elevations of the order of 60^o, by four standard deviations, for which we had no explanation. We noted that the combination of multipathing with spill over into side lobes could in principle generate oscillations at large elevations but we could not think of a sensible explanation along such lines.

3.1.3 Possible physics interpretations

To the extent that instrumental effects could be rejected, differences between the precise characteristics of the oscillations simultaneously observed at Learmonth and in Ha Noi are intriguing and call for an explanation. Two come to mind as natural candidates: one is the effect of the different polarization states detected in Ha Noi and at Learmonth, the other is the effect of different distortions caused by the traversal of the local ionosphere by the solar signal. Indeed, the particular position of Ha Noi with respect to the geomagnetic equator implies for it a maximal ionospheric scintillation index S4 (IPS 2012b) as shown in Figure 3.5. There exists an abundant literature on the effects of scintillation on L band transmission through the ionosphere (E.K. Smith & W.L. Flock 1994; S. Basu *et al.*, 2002) providing evidence for major disturbances affecting both the amplitude and phases of the transmitted signals, with important dependences on solar activity and on time, both seasonal and diurnal, multipathing resulting from inhomogeneities of the local ionosphere.

Some of the features observed and reported were considered reminiscent of the properties of coronal oscillations that have been studied extensively at visible and ultraviolet wave lengths (J. Chen and P.W. Schuck 2007; B. Roberts 2000). In particular, coronal loop transverse oscillations have been identified for the first time by (M.J. Aschwanden *et al.* 1999) using the Transition Region and Coronal Explorer (TRACE) in the extreme UV. They have periods of the order of 5 min, similar to that of photospheric oscillations, but are quickly damped. They have been interpreted as global oscillations, the loop being bodily displaced with the foot points remaining fixed (kink mode), triggered by a flare shock. Such oscillations have since been the object of new observations and have triggered the elaboration of several MHD models attempting their descriptions. However, reports of such oscillations at radio wavelengths are much less common. Strong oscillations with a period of 5.6 min were once reported at 22 GHz (F.M. Strauss, P. Kaufmann and R. Opher 1980) as lasting for about two hours using the Itapetinga radio telescope to track an active region of the Sun. Oscillations with periods ranging from 3 min to hours have been reported to be associated with solar active regions and are now extensively studied using the Nobeyama radio heliograph (G.B. Gelfreikh *et al.* 2004). There have also been reports of an association of so-called Type II radio-bursts, occurring from a few hundred down to one MHz, with coronal loop oscillations (H.S. Hudson and A. Warmuth 2004) but this is unrelated with what we observe.

While polarization effects are expected to be important in the detection of MHD oscillations, the Ha Noi and Learmonth data are not independent, the latter being a linear combination of the right handed signals observed in Ha Noi with a left handed component.

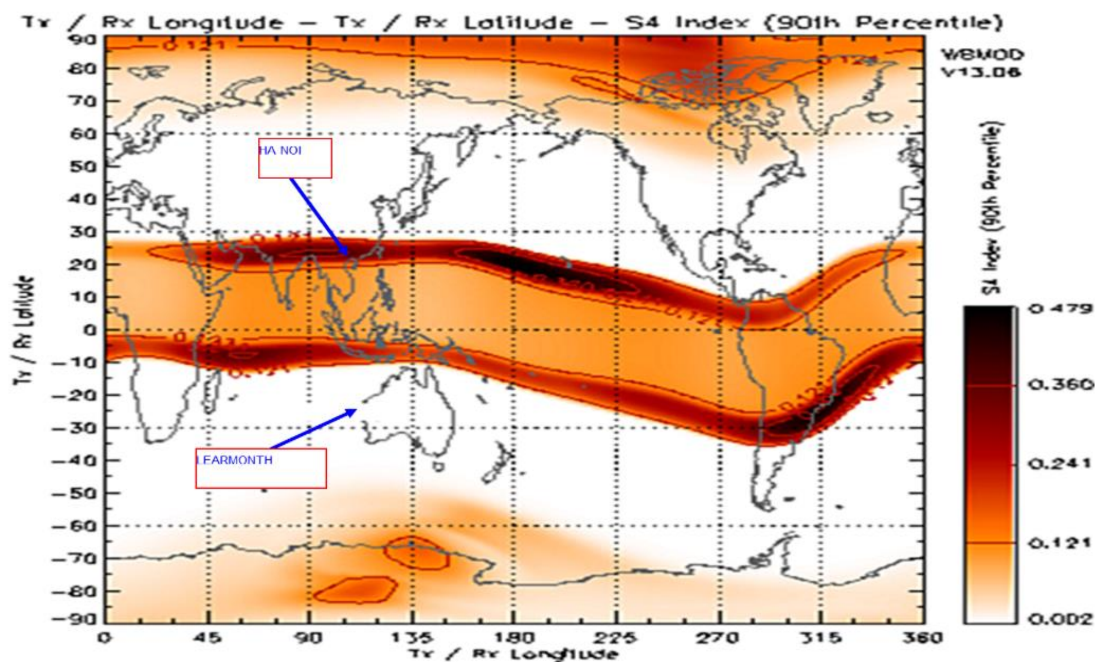

Figure 3.5 Typical geographical distribution of the ionospheric scintillation S4 index (IPS 2012b).

3.1.4 Summary

I reproduce below, *in extenso*, the summary of these early observations as they were published in (N.V. Hiep *et al.* 2014).

The Sun has been observed using the VATLY radio telescope at 1415 MHz between mid April and early September, 2012. The data have been analysed together with similar data collected by the Learmonth solar observatory in Australia. Both sets of data see the same general features, including flares of which three, in early July, are particularly strong. Comparison between the Learmonth and Ha Noi data shows that the former have smaller noise, by a factor ~1.7, but provides evidence for the proper performance of the VATLY radio telescope.

Both sets of data display frequent oscillations at the percent level and with periods around 6 min that last for a fraction of an hour typically. A detailed comparative analysis of the properties of these oscillations has been performed. The possibility that they might result from instrumental effects has been explored. A particularly serious candidate for such an explanation is multipathing, which, however, would not cause the strong observed correlation between Ha Noi and Learmonth periods. Moreover, in its simple form of being the result of reflections from obstacles on ground, it can be rejected as not being enhanced near the horizon; however, it illustrates how instrumental effects that we did not think about might possibly produce the observed oscillations. In particular, its most frequent occurrence at elevations close to 60^{o} remains unexplained. This caveat must be kept in mind when exploring possible physics interpretations.

While having uncorrelated amplitudes, the oscillations observed in Ha Noi and at Learmonth reach together, on average, their higher periods as well as their lower periods and tend to be in phase. However, when looked at time interval by time interval, they differ significantly, displaying important smearing with respect with this average behaviour. Moreover, the average amplitude in Ha Noi is larger than in Learmonth (by a factor ~1.75) while the period span in Learmonth is larger than that in Ha Noi (by a factor ~2.2).

Two physics effects that might cause some differences and that came to our mind are different polarization states (circular in Ha Noi, linear in Learmonth) or multipath effects resulting from inhomogeneous ionospheric transmissions (Ha Noi sits on a maximum of the S4 scintillation index while Learmonth is normal).

3.2 Correlated multipath effects between distant radio telescopes

3.2.1 Introduction

The intriguing observation of correlations between the periods of the mHz oscillations detected at Ha Noi and Learmonth led VATLY to seek the advice of world experts in the domain of solar physics, none of whom, however, was able to find an explanation. It was therefore decided to submit the result of the VATLY observations for publication in Solar Physics, in the hope that the referee would explain the effect, but the paper was accepted for publication (N.V. Hiep *et al.* 2014). The decision was then taken to start a new campaign of measurements in the winter 2013-2014 (November-December-January) in which I took part and the results of which are reported in the present section. Improvements were made to the analysis, in particular all oscillations were studied in each observatory without requiring their simultaneous observation by both observatories; moreover, any subjective factor was removed from the selection of time intervals during which both Learmonth and Ha Noi data display oscillations. The observation of strong correlations between the periods of oscillations and the time in the day, with characteristic patterns, was determinant in finding the solution of the puzzle. After having investigated a few unsuccessful hypotheses, we soon realized that what we were observing was in fact the result of interferences between the signal directly received from the Sun and its specular reflection on ground detected in a side lobe. The characteristic features of such interferences were found to match well the observations, both earlier and current, and the reason for a correlation between the periods of the observed oscillations was soon made clear.

Rather than reporting the results of our findings in chronological order, I prefer to privilege clarity by giving a presentation based on the description of the effect.

3.2.2 Pioneer observations in Australia

In the middle of the last century, in the wake of observations made by Navy officers during World War II, according to which the radar echo of a plane flying near horizon above the ocean is modulated by interference fringes, Australia was the home of the founding fathers of radio interferometry and the site of pioneering observations using the so-called “sea-cliff interferometer” (W.T. Sullivan III 1991; J.G. Bolton 1982). The principle of the method was to observe a radio source as it rises above the horizon with a single antenna located on top of a cliff above the ocean; the direct wave and its reflection on the water surface interfere and produce interference fringes that allow for considerably improved angular resolution with respect to what was possible at that time. Observations of solar spots (L.L. McCready, J.L. Pawsey and R. Payne-Scott 1947), soon followed by observations of various radio sources (J.G. Bolton 1948; J.G. Bolton and G.J. Stanley 1948a,b; J.G. Bolton and G.J. Stanley 1949; J.G. Bolton, G.J. Stanley and O.B. Slee 1949), have then been reported.

The present work is an illustration of the same mechanism causing correlations between apparent solar oscillations simultaneously detected by two distant observatories respectively located in Ha Noi (Viet Nam) and Learmonth (Australia) using radio telescopes operated at 1.415 GHz. In this case, oscillations are not observed on the rising Sun but at large elevations: the reflected wave reaches the antenna in one of its side lobes, at large angle with respect to the beam. As a result, the oscillations have amplitudes of a few per mil, rarely exceeding 1%. They occur on the ground surrounding the antenna and their periods are in the range of a few minutes.

The intriguing existence of correlations between the Ha Noi and Learmonth observations had first been considered as an argument against a possible instrumental effect (N.V. Hiep *et al.* 2014). It is now clearly established that the cause of the correlation is purely instrumental. The following sections develop this argument, accounts of which have been presented elsewhere (P.N. Diep *et al.* 2014).

3.2.3 Multipath from specular reflection on ground

Interferences between the direct plane wave emitted by a radio source and detected in an antenna, and its specular reflection on a horizontal surface – flat ground or ocean – have been known to produce oscillations since the first days of radio interferometry (W.T. Sullivan III 1991; J.G. Bolton 1982). Writing ξ the difference in path length between the interfering waves, υ the frequency and λ the wavelength, here ~21 cm, the time difference between the two interfering waves is $\Delta t= \xi/\lambda\upsilon$. Introducing a parameter ε to account for the attenuation resulting from the reflection on ground and from the lesser gain of the side lobe in which the reflected wave is detected, the dependence on time *t* of the detected signal reads

$$\begin{aligned} S &= |e^{i2\pi\nu(t-½\Delta t)} + \varepsilon e^{i2\pi\nu(t+½\Delta t)}|^2 \\ &= |e^{i2\pi\nu t}|^2 |e^{-i\pi\xi/\lambda} + \varepsilon e^{i\pi\xi/\lambda}| \qquad (3.2) \\ &= 1 + \varepsilon^2 + 2\varepsilon\cos(2\pi\xi/\lambda) \end{aligned}$$

In a time interval centred on t_0 (where $\xi=\xi_0$) the time dependence of the oscillation reads therefore

$$\mathrm{S(t)} = 1 + \varepsilon^2 + 2\varepsilon\cos\{2\pi\lambda^{-1}(\xi_0 + [\mathrm{t}-\mathrm{t}_0]\mathrm{d}\xi/\mathrm{dt})\} \qquad (3.3)$$

Describing the oscillation as a sine wave, $sin(2\pi[t-t_0]/T + \varphi)$, implies a period $T = \lambda/(d\xi/dt)$ and a phase $\varphi = \pi/2 + 2\pi\xi_0/\lambda$. In order to have T positive, one prefers to write

$$T = \frac{\lambda}{|d\xi/dt|} \quad \text{and} \quad \varphi = \pi/2 \pm 2\pi\xi_0/\lambda \tag{3.4}$$

where the + sign is for ξ increasing with t and the – sign for ξ decreasing with t.

Relation (3.4) implies a fundamental relation between T and $d\varphi/dt$

$$T|d\varphi/dt| = 2\pi \tag{3.5}$$

which is characteristic of the multipathing effect.

Note that Relation (3.4) allows for an evaluation of $d\xi/dt$ from measurements of T and/or $d\varphi/dt$ but not for a measurement of ξ itself: the difference in path length can only be obtained up to an unknown integer number of wavelengths. Equivalently, φ is only defined up to an unknown integer factor of 2π.

From Figure 3.6, $\xi=2D\sin h$ where D is the distance of the antenna to ground and h the elevation of the source.

As h increases with t in the morning and decreases with t in the afternoon, so does ξ. At a same time t, from one day to the next, one expects therefore φ to increase in the morning in the Northern hemisphere between December 22[nd] and June 21[st]. Changing from morning to afternoon, or from Northern to Southern hemisphere or from December-June to June-December changes the sign of the daily variation of φ.

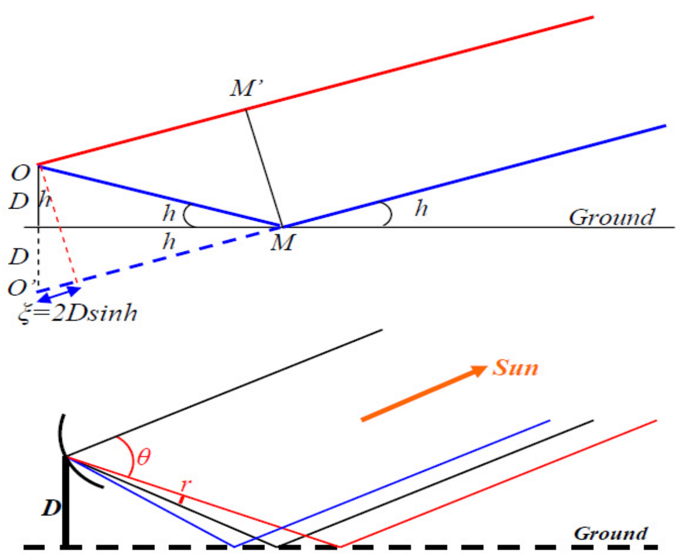

Figure 3.6 Upper panel: geometry of specular reflection on ground into a dish centred in O and having image O' in the ground mirror. Lower panel: departure from exact specular reflection (mean ray), definition of the angles r and θ.

If the hypothesis of specular reflection is slightly relaxed, reflections with an impact point farther away from the antenna than the specular impact (i.e. reaching the dish at a smaller angle with respect to the main lobe) are favoured with respect to reflections with an impact point closer than the specular impact. The reason is not only from pure geometry arguments but also because the reflected wave reaches the dish at large angle with respect to the beam and the antenna gain, on average, decreases with this angle. This causes the mean impact to be behind the specular impact and the path difference ξ to take larger values than in the specular case; as D is proportional to ξ, it is overestimated accordingly. The effect is easily simulated by describing the deviation from specular reflection by a Gaussian dependence of the reflection probability on the angle r of the reflected wave with respect to the specularly reflected wave, $exp(-½r^2/\sigma_r^2)$ and the decrease of the antenna gain by another Gaussian dependence on the angle θ between the reflected wave and the antenna axis, $exp(-½\theta^2/\sigma_\theta^2)$ (Figure 3.6). Moreover, accounting for the irregularities of the reflecting surface can be approximated by a smearing of ξ using a third Gaussian, $exp(-½\Delta\xi^2/[\xi\sigma_{sm}]^2)$.

An important consequence of the above mechanism is the existence of a correlation between the periods of simultaneous oscillations independently detected by two distant observatories such as Ha Noi and Learmonth. Consider two radio telescopes operated at a same frequency at heights D_1 and D_2 above a flat ground in observatories located at respective longitudes and latitudes (ψ_1,φ_1) and (ψ_2,φ_2).

Writing $h'=|dh/dt|$, the periods read $T_{1,2}=½\lambda/[D_{1,2}h'_{1,2}cos(h_{1,2})]$. In the approximation of a circular Earth orbit, calling δ the Sun declination and $H=t+\psi$ the hour angle $sinh=sin\delta sin\varphi+cos\delta cos\varphi cosH$ (H=0 when the Sun crosses the meridian plane). Hence,

$$T=\frac{T^*}{cos\delta|\sin(t+\psi)|} \tag{3.6}$$

with $T^*=½\lambda/(Dcos\varphi)$ being a constant for each observatory. Writing $\rho=T/(T^*cos\delta)$, $\rho^1=1/|sin(t+\psi_1)|$ and $\rho^2=1/|sin(t+\psi_2)|$ are trivially correlated, implying a correlation between the periods measured simultaneously by both observatories. If the two observatories are exactly at the same longitude, $\rho_1=\rho_2$ at any time. In practice, the longitudes of the two observatories should not be too different for them to have a chance to observe the Sun simultaneously for long periods of time. In the Ha Noi/Learmonth case, the two latitudes are nearly opposite (±21.6°±0.6°) and the two longitudes are nearly equal (–110°±4°). In the approximation where $\psi_1=\psi_0-\Delta$, $\psi_2=\psi_0+\Delta$, $0<\Delta<<1$ *rad* (observatory 1 being east of observatory 2) and writing $H_0=\psi_0+t$ the mean hour angle,

$$\rho^1 = \frac{1}{|sin(H_0+\Delta)|} \text{ and } \rho^2 = \frac{1}{|sin(H_0-\Delta)|} \tag{3.7}$$

Around noon, the elevation is stationary and the period of the oscillations takes very large values outside the range where they can be detected. In the morning, $H_0<-\Delta$, the elevation, and therefore the period of the oscillations increases with time. In the afternoon, $H_0>\Delta$, they decrease. Changing H_0 into $-H_0$ changes ρ_1 into ρ_2. In the morning, both periods increase, that of observatory 1 faster than that of observatory 2. In the afternoon, both decrease, that of observatory 2 faster than that of observatory 1. This is schematically illustrated in the left panel of Figure 3.7.

The predicted correlation is essentially independent of the season during which observations are made: the only seasonal contribution is from the $cos\delta$ term which remains confined between 0.92 and 1 over the whole year and has therefore very little effect.

3.2.4 Observed oscillations in Learmonth and Ha Noi

When applied to a real observatory, the parameters that characterize the oscillations are strongly dependent on the environment of the antenna. In the cases studied here, Ha Noi and Learmonth, the distance of the antenna to the reflecting surface is between 5 and 20 m, the latitude is ~±22° and the wavelength is 21 cm. Hence T^* is between 1 and 5 min. The method used to detect oscillations requires their period to be of the order of a few minutes, say 2 to 10 minutes typically, excluding an interval of 1 to 2 hours around local noon, during which the period of the oscillations is too large to be observed. However, the rest of the time, one deals with a broad range of elevations, allowing the impact point on ground to reach close to the antenna.

The Learmonth antenna (Figure 3.8 left) is located in an airport on a pole erected some 7.5 m above a flat ground. The only nearby building is located south of the antenna, outside the range of azimuths toward which the antenna is pointing. On the contrary, the Ha Noi antenna (Figure 3.8 right) is on top of a small building, some 20 m above ground and some 5 m above the flat roof, in a urban environment. One would therefore expect the multipath pattern observed at Learmonth to be considerably simpler and easier to describe than that observed in Ha Noi.

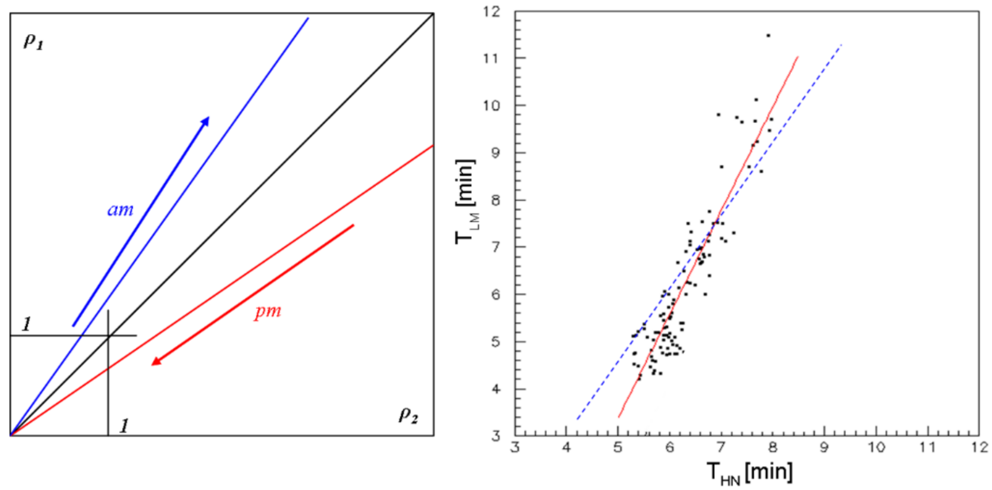

Figure 3.7 Correlations observed between the periods of oscillations measured in two observatories at nearby longitudes. Left panel: schematic illustration of the main features; the angle between the morning and afternoon lines is a measure of the difference of longitude between the two observatories. Right panel: correlation observed in N.V. Hiep *et al.* (2014) between Learmonth (ordinate) and Ha Noi (abscissa); the dotted line displays the model prediction for morning oscillations using respective *D* values of 7 m and 6 m for Learmonth and Ha Noi respectively.

Figure 3.8 Sites of the observatories in Learmonth (left, courtesy of Dr Owen Giersch) and Ha Noi (right). The lower panels show satellite maps of the two sites (source: Google map).

The data used in the present work cover the period October 24th 2013 to January 31st 2014 for both Ha Noi and Learmonth. In addition Learmonth data collected during the 10 central days of each month of the year have been included in the analysis. For both Ha Noi and Learmonth, the signal to noise ratio is of the order of 500.

After subtraction of solar flares and occasional interferences of human origin, the time dependence of the antenna temperature, averaged over the bandwidth, is searched for oscillations having periods in the 2 to 10 minutes interval. The method consists in evaluating, for each independent measurement, the amount of oscillation that the data can accommodate. Each oscillation is evaluated over a 20 min interval centred on the particular measurement i and is characterized by an amplitude A_i, a phase φ_i, a period T_i and a chi square describing the quality of the fit, χ^2_i. The significance of such oscillations can then be assessed objectively from the values of A_i and χ^2_i without requiring human intervention. For each period T_i and each measurement i one calculates the mean value M_i and the rms deviation with respect to the mean R_i in a time interval centred on measurement i and having a width T_i. In a second step, a fit of the antenna temperature is performed over a 20 min time interval centred on measurement i to a form $M_i+\eta R_i sin(2\pi(t–t_i)/T_i+\varphi)$. Here t spans the 20 min interval while t_i is the time of measurement i. Parameters η and φ measure the relative amplitude and phase of the oscillation respectively. The problem being linear in $\eta\cos\varphi$ and $\eta\sin\varphi$ allows for an easy explicit calculation of the parameters. Figure 3.9 illustrates the procedure.

Significant oscillations are defined as having a small χ^2 value, a large η value (meaning that the oscillation accounts for a major fraction of the signal fluctuation in the 20 min interval) and a large $\eta R_i/M_i$ value (meaning that the amplitude of the oscillation exceeds noise level). Different selection criteria have been tried and the robustness of the corresponding conclusions has been ascertained.

Distributions of time versus period using sensible selection criteria display very clear patterns that are illustrated in Figure 3.10 and follow the same trend as expected from specular reflection on ground. Examples of the evolution of the phase of the oscillations from one day to the next are displayed in Figure 3.11. Here again, the dependence on season, hemisphere and time in the day is as expected from specular reflection on ground.

3.2.5 Comparison between observations and predictions

Having illustrated by a few examples in Figures 3.10 and 3.11 the good qualitative agreement between the observed oscillations and the predictions of a multipath model assuming perfect specular reflection on ground, we now attempt a more quantitative analysis of the effect. The measurements of the period and phase of the oscillations provide independent evaluations of the altitude D of the antenna above ground. From $T=\lambda/|d\delta/dt|=\frac{1}{2}\lambda/(D|dh/dt|cosh)$ one obtains

$$D = \frac{1}{2}\frac{\lambda}{T|dh/dt|cosh} \tag{3.8}$$

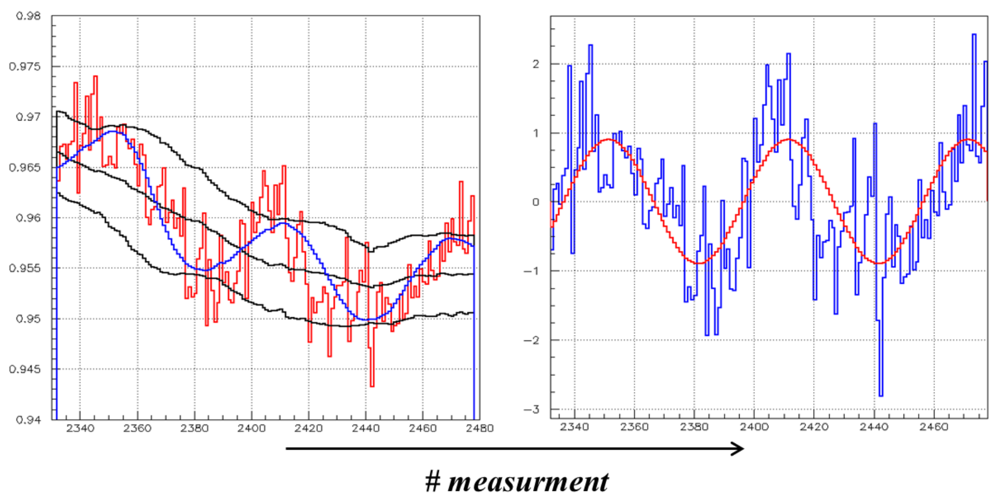

Figure 3.9 A typical oscillation. The left panel shows the data (red) together with the fit (blue) and M and $M\pm R$ (black). The right panel compares data (blue) and fit (red) after subtraction of M and division by R.

Relation (3.8) relates the height D of the antenna above the reflective surface to the measured value of the period of the oscillations under the hypothesis of specular reflection. Figure 3.12 displays the distributions of D obtained this way for the oscillations observed in Learmonth and Ha Noi. The former is dominated by ground reflections while the latter displays a more complex structure revealing reflections from the observatory roof in the morning and late afternoon and from ground in the early afternoon. Knowing D, it is easy to map the impact coordinates on ground, $x=Dcosa/tanh$ and $y=Dsina/tanh$. They do not display any particular structure in the Learmonth case, which is consistent with a flat ground, while revealing clearly distinct regions in the Ha

Noi case, that are unambiguously associated with the topography of the environment as shown in Figure 3.8.

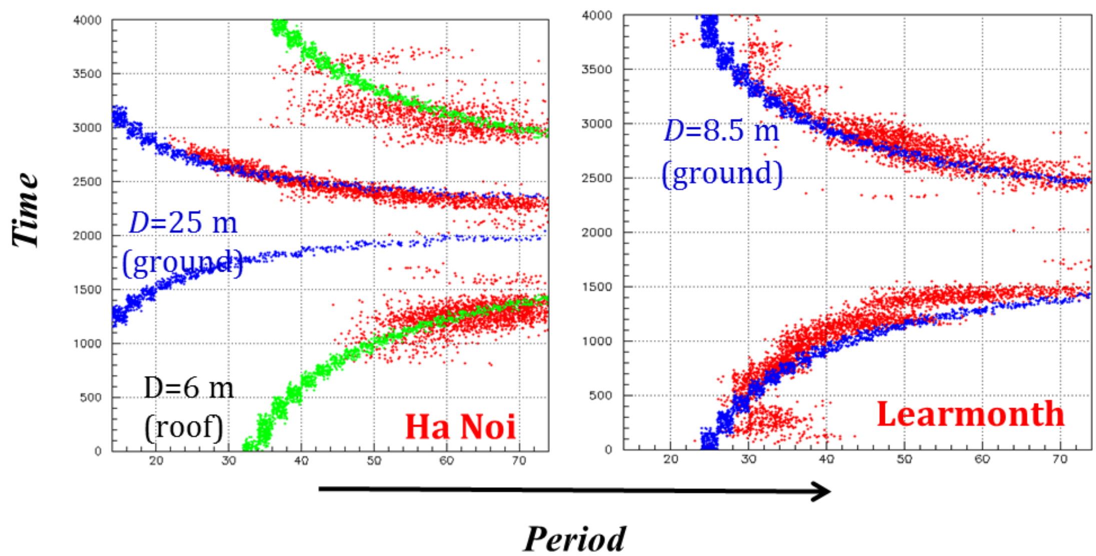

Figure 3.10 Examples of time *versus* period scatter-plots. Left panel: Ha Noi data (red) collected between October 25th and December 17th, 2013. The lines are specular reflection multipath predictions for D=6 m (roof) and D=25 m (ground). Right panel: Learmonth data (red) collected in the 10 central days of May 2012. The blue lines are ground specular reflection multipath predictions for D=8.5 m.

Using reasonable values for the parameters describing a small departure from exact specular reflection on ground, it is easy to obtain a good description of the D distributions as illustrated in Figure 3.12 where a common value of 45° has been used for σ_a while σ_r takes values between 9° and 16° and σ_{sm}~10%. The quality of the data does not allow to measure these parameters precisely and other combinations of their values can be found that give also acceptable results.

However, in all cases, the departure from exact specular reflection that can be accommodated remains small, not exceeding 20°. An effect of the inclusion of such departure is to significantly lower the estimate of D_T with respect to exact specular reflection: from 8.3 m to 7.7 m in the case of Learmonth and, in the case of Ha Noi, from 6.2 m to 5.7 m for the roof and from 26 m to 21 m for ground, improving significantly the agreement with real dimensions (respectively 7.5 m, 5.6 m and 17.7 m).

The correlation expected between oscillations observed in the morning at Learmonth from ground and in Ha Noi from reflections on the observatory roof is illustrated in Figure 3.7 (right). The agreement with observation is remarkable given the crudeness of the model used.

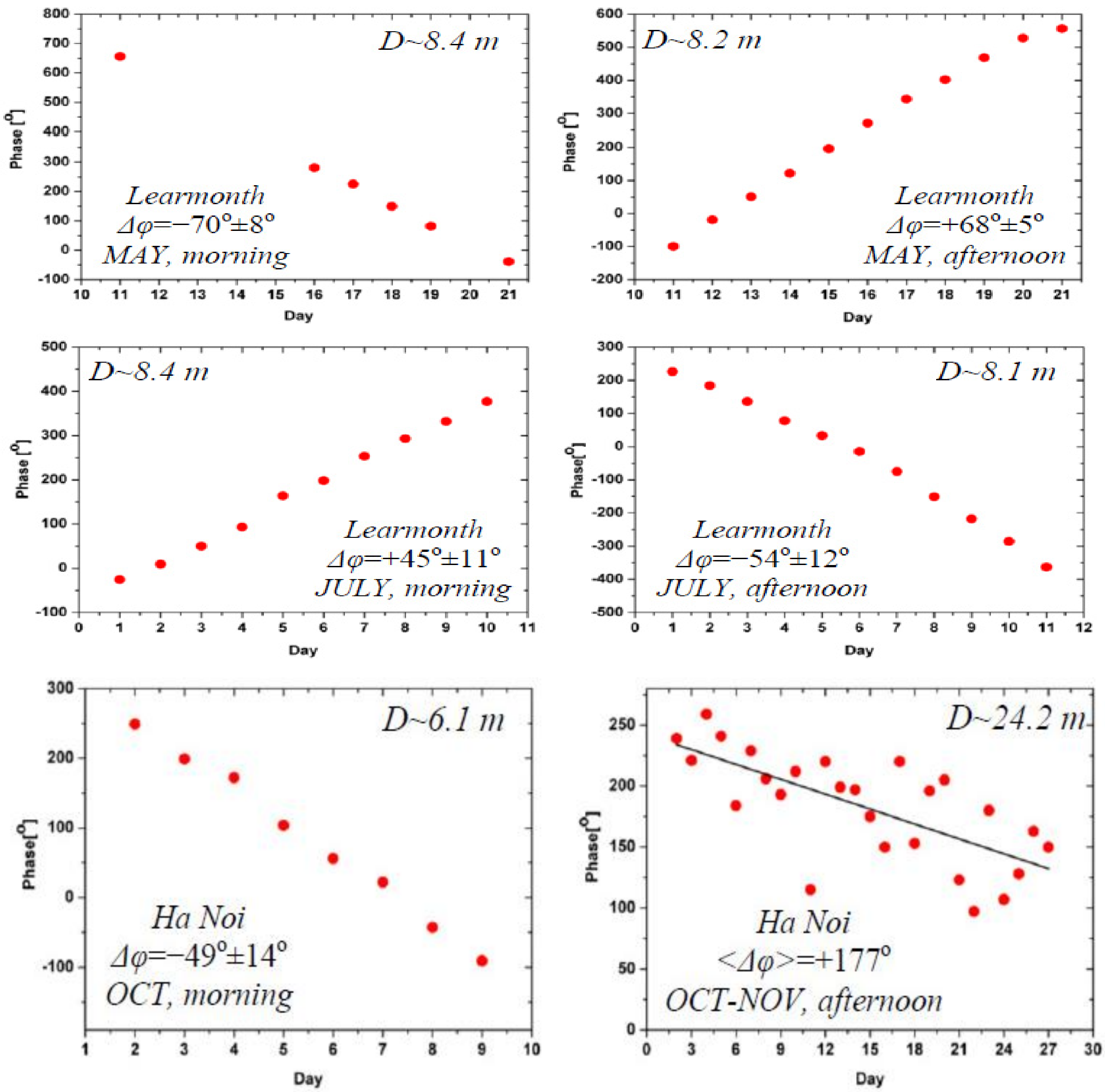

Figure 3.11 Dependence on the date of the phases of oscillations observed under different conditions. The lower right panel displays the daily phase increment rather than the phase itself and is seen to decrease when approaching the winter solstice as expected (its large value results from the large associated *D* value).

Relation (3.5), which relates independent measurements of the period and phase of the observed oscillations, offers a crucial test of their multipath nature. Note that the path difference between the direct and reflected waves is of the order of magnitude of D for the rather large values of the Sun elevation associated with the observed oscillations, meaning several tens of wavelengths. As remarked earlier, the phase of the oscillation is measured up to an integer multiple of 2π and it is not possible to measure D directly from a single phase value but $d\varphi/dt$ is simply evaluated from the phase difference between two successive measurements. The distribution of $(2\pi)^{-1}T|d\varphi/dt|$ obtained this way is displayed in Figure 3.13 for Learmonth and Ha Noi oscillations having amplitudes in excess of 3‰, giving in both cases very strong evidence for the multipath nature of the effect. Mean(rms) values of 1.01(0.11) and 1.00(0.13) are obtained for Learmonth and Ha Noi respectively, giving strong evidence for the multipath origin of the observed oscillations. Note that Ha Noi data mix reflections from ground and from the observatory roof, spanning a broad range of D values. The Learmonth data cover the whole year and the simple topography implies reflections from a flat ground with a well defined D value, 8.24 m on average. It fluctuates by only ±0.37 m over the year and the rms value of its distribution is 1.21 m on average. Comparing the summer months (November to February) with the winter months (May to August) for the retained oscillations, the mean elevation of the Sun is found to vary from 49° to 35° and the mean amplitude of the oscillations from 5.0‰ to 6.8‰ while the width of the distribution of $(2\pi)^{-1}T|d\varphi/dt|$ remains constant to better than 10% of its value. The number of retained oscillations is nearly twice as large in winter than in summer.

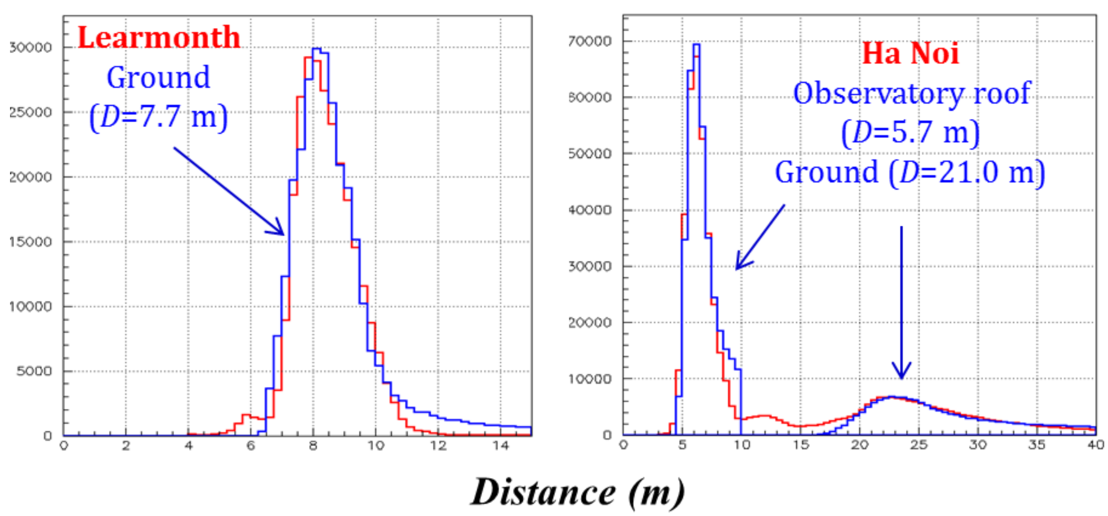

Figure 3.12 Distributions obtained from the Learmonth (left panel) and Ha Noi (right panel) data in November-December 2013. The blue lines show model predictions allowing for small departures from exact specular reflections (see text).

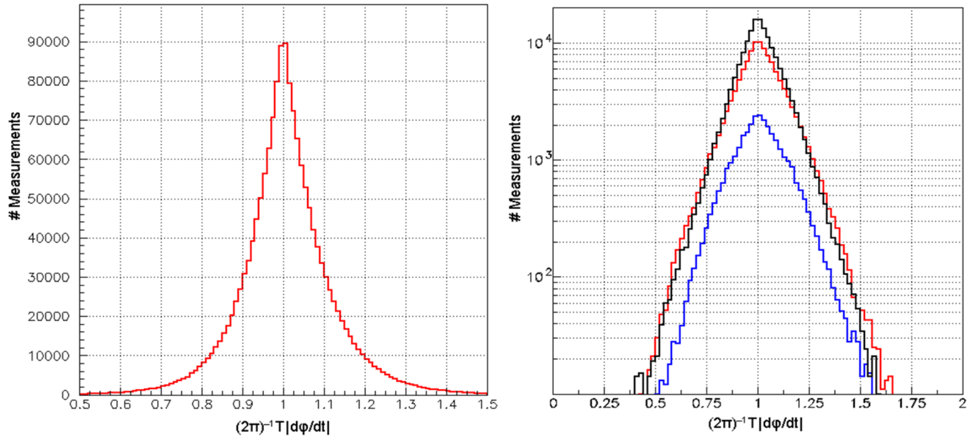

Figure 3.13 Distribution of $(2\pi)^{-1}T|d\varphi/dt|$ for oscillations having amplitudes in excess of 3‰ for Learmonth (left panel) and Ha Noi (right panel) data. The Ha Noi distributions display separately ground reflections (black) and roof reflections (blue in the morning and red in the afternoon). A log scale is used for Ha Noi in order to ease the comparison between ground and roof reflections but when plotted with a linear scale it displays the same shape as that shown in the left panel for Learmonth.

3.2.6 Conclusion

When observing the Sun, multipath effects between the direct wave reaching the antenna in the main lobe and its reflection on ground reaching the antenna in a side lobe have been shown to produce correlations between the periods of oscillations observed independently by two distant radio telescopes. The case of observations made at 1.4 GHz in Ha Noi and Learmonth has been studied in some detail. Strong evidence for the multipath origin of the observed oscillations has been obtained from the relation between their periods and their phases. Good agreement between observations and model predictions has been found and the departure from exact specular reflection that the data can accommodate has been shown to be small. The oscillations have periods and phases that are remarkably simple functions of time and are well described by the model. Their amplitudes, at the level of a few per mil, are consistent with the gain drop expected between the main and side lobes of the antenna pattern. The existence of a correlation between independent observations from two distant observatories, together with the large values of the elevation at which the oscillations were observed, had been used earlier (N.V. Hiep *et al.* 2014) as arguments against an instrumental explanation. It is now clear that the effect is of purely instrumental nature, making a search for genuine solar oscillations in this range of periods and amplitudes unfeasible with such instruments.

CHAPTER 4

RADIO OBSERVATION OF THE MOON

The Moon is known to be a strong radio source. At the limit of the ability of our telescope, it is a convenient target for the study of its sensitivity. Its radio emission has been studied in detail in the third quarter of the past century (P.G. Mezger and H. Strassl 1959, J.E. Baldwin 1961, C.E. Heiles and F.D. Drake 1963, V.A. Razin and V.T. Fedorev 1963, P.H. Moffat 1972 and F.P. Schloerb *et al.* 1976). At infrared wavelengths there are variations correlated with the lunar phase which are due to solar heating. At centimetre wavelengths such variations are nearly negligible. This is because radio emission (which is thermal) arises from below the surface, underneath the regolithe, where the rock is heated by conduction and the variations lag behind solar heating.

4.1 Beam-switching observations

A first series of 14 observations was performed between May 6th and June 17th 2014. Each observation covered a full transit of the Moon and was made by pointing the telescope to the Moon trajectory in a succession of measurements, each lasting ~8 min, namely including typically 60 frequency spectra. Precisely, the telescope was pointed alternately on and off the Moon, off-the-Moon pointings alternating between 7^{o} up and 7^{o} down in elevation with respect to the Moon trajectory. Each pointing was such that the Moon would cross its azimuth at mid-period. The sequence of observations was therefore as follows: 8 min on, 8 min up, 8 min on, 8 min down, 8 min on, 8 min up, 8 min on, etc. The strategy used to analyse the data is to consider pairs of successive "on-off" observations and to compare the associated antenna temperatures. In 8 min, the Moon spans typically 2^{o}, meaning ±1^{o} with respect to the antenna pointing direction, small enough compared with the σ of the beam (2.3^{o}) to have a nearly negligible effect (it decreases the flux by only 3%). On the contrary, the 7^{o} shift in elevation keeps the Moon contribution at a low enough level (between 1% and 3%). The central frequency was fixed at 1420.4 MHz.

In order to eliminate contributions from HI clouds and RFIs, the measurement of the continuum antenna temperature is limited to a pair of intervals of frequency bins, below and above the 21 cm hydrogen line. A first linear fit is made over these intervals and measurements deviating from it by δ>10 K in absolute value (Figure 4.1 left) are rejected. The fit is then repeated, giving, for each spectrum j, values a_j, b_j and χ^2_j, of respectively the slope of the antenna temperature (in Kelvin per frequency bin), the antenna temperature at the frequency of the 21 cm line, and a measure of the quality of the fit (calculated for an arbitrary 1 K uncertainty and divided by the number of degrees of freedom). Figure 4.1 displays the distributions of a_j/b_j and of χ^2_j. The inequalities $|a_j/b_j-0.45\ 10^{-3}|<0.20\ 10^{-3}$ and $\chi^2_j<28$ were required to be obeyed for the measurement to be retained. The distribution of χ^2_j indicates that a typical uncertainty of 4 K is attached to each frequency bin. Moreover, in order to exclude measurements where the system temperature and/or the sky antenna temperature are too high (possibly because of the proximity of the Sun, or of the Milky Way, or simply of ground) the inequality 205 K$<b_j<$255 K has also to be obeyed.

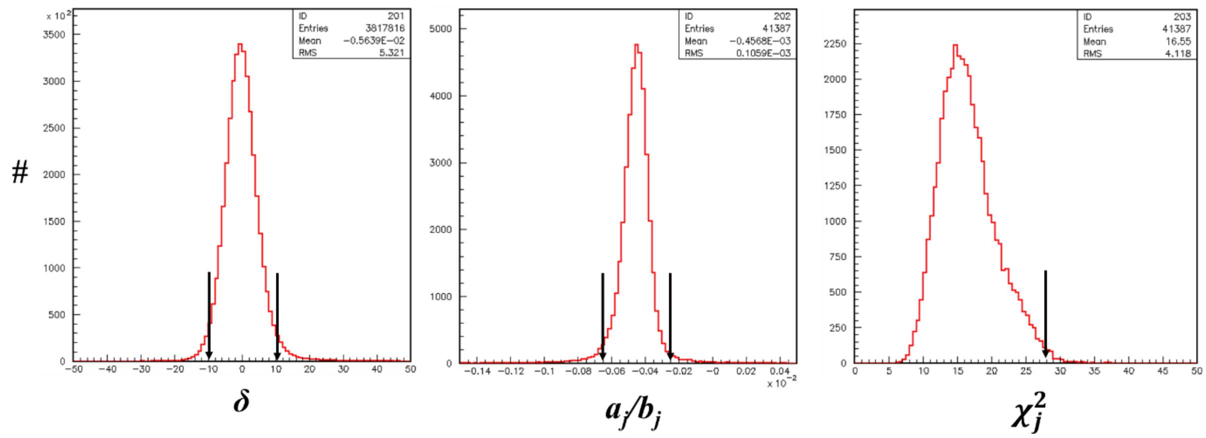

Figure 4.1 Distributions of δ (left), a_j/b_j (centre) and χ^2_j (right). The arrows indicate the cuts that are applied.

The next step checks the consistency of the sixty or so measurements of a same pointing. A linear fit of the form $b_j=b_0+b_1(j-j_{mean})$ is performed for each pointing, j_{mean} being the value of j at mid-time, when the Moon crosses the meridian to which the telescope is pointing. Here again, the fit is made in two steps, the first step calculating the mean value of b_j for the current pointing and the second step retaining only values of b_j deviating from it by $\Delta b<1.5\ K$ in absolute value (Figure 4.2 left). For a pointing to be retained in the final sample, it has to include a number $N>40$ of good measurements, to have a χ^2 per degree of freedom not exceeding 0.75 and a value of b_1 not exceeding 10 mK per measurement in absolute value. Distributions of these quantities are displayed in Figure 4.2.

The above selection retains 77 pairs of "on-off" pointings with two values of b_0, b_{on} and b_{off} measuring respectively the antenna temperatures of the Moon+sky and of the empty sky. We correct for the evolution of the empty sky antenna temperature between the "on" and "off" pointings, separated by ~60 measurements, by defining the Moon antenna temperature as $A_{Moon}=b_{on}-(b_{off}-60b_1)$. Its distribution is displayed in Figure 4.3. It has mean and rms values of 0.6 K and 1.2 K respectively. Requiring the antenna temperature of the empty sky not to exceed 245 K (240 K) reduces the sample to 57 (26) pairs of pointings and increases the mean value of the Moon antenna temperature to 0.7 K (0.9 K). This illustrates the importance of systematic errors in this set of data. The result varies typically between 0.5 K and 0.9 K when the selection cuts are varied within reasonable limits, making a realistic evaluation of the final uncertainty difficult.

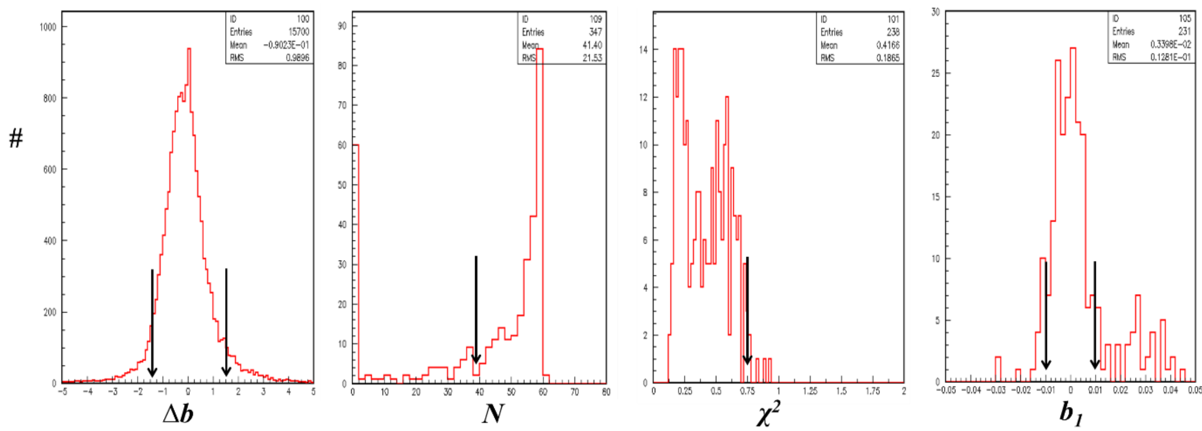

Figure 4.2 From left to right, distributions of Δb, N, χ^2 and b_1. The arrows indicate the cuts that are applied.

Different analyses using triplets of successive pointings of the type "off-on-off" or "on-off-on" as well as quintets of the type "on-up-on-down-on" have been made but failed to bring a significant improvement of the reliability and accuracy of the measurement. The main reason is the important variation of the empty sky temperature from one pointing to the next. The b_1 cut of 10 mK per measurement means a maximal excursion of ±0.3 K across the pointing and ±0.6 K between pointings, commensurate with the Moon antenna temperature being measured. More frequent beam-switching would have improved the situation in this respect (steering the antenna by 7^o in elevation and a few degrees in azimuth takes no more than 20 s). Another lesson of these observations is the importance of choosing a frequency as free as possible of HI clouds and RFIs. In this respect, the choice of 1420.4 MHz as central frequency was not optimal, the effective system temperature being higher there than at lower frequencies. We retain as final result a Moon antenna temperature of 0.7±0.2 K, dominated by systematic uncertainties.

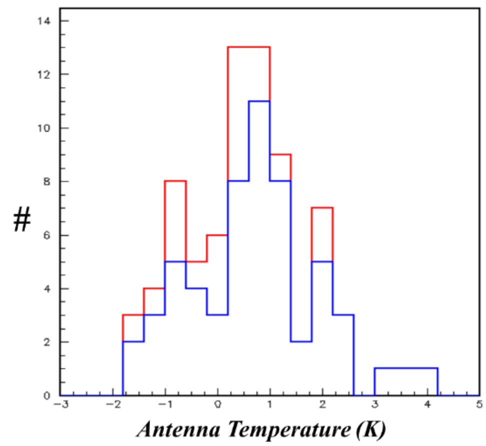

Figure 4.3 Distribution of the antenna temperature of the Moon, A_{Moon}, for the sample of 77 retained pairs of pointings (red) and for those obeying in addition the constraint b_{off} <245 K (blue).

4.2 Drift scans

Taking advantage of the experience gained with the series of beam-switching measurements, a second campaign of observations was made, this time collecting a large number of drift scans, each lasting 40 min, such that the telescope be pointing to the Moon at mid scan, namely 20 min after start. As 20 min corresponds to an angular drift of $5^{o} \cos\delta$, where δ is the declination, and the antenna lobe has a σ of 2.3^{o}, the sagitta of the dependence of the detected flux on time is more than $1-\exp(-½(5/2.3)^2)$~90% of the true flux. As we are close to a minor lunar standstill, the Moon declination remains small and the $\cos\delta$ factor has little influence. The frequency was fixed at 1417.6 MHz in order to be as free as possible from RFIs and HI clouds and observations were performed between July 16th and October 12th, 2014. After having rejected scans pointing too close to the Sun, the Milky Way or obstacles on ground, scans where the Moon at mid-scan is more than 0.8^{o} away from the pointing direction of the telescope and scans displaying sudden changes of gain resulting from strong RFIs, we are left with a total of 80 drift scans to be analysed.

In a first phase, we fit a straight line, $aj+b$, to the antenna temperature T_j measured in bin j of each frequency spectrum (of which there are 310 per drift scan). The resulting distributions of a, b, a/b, χ^2 and $|\delta_j|=|T_j-a_j-b|/\Delta_j$ (using an uncertainty Δ_j=2 K) are displayed in Figure 4.4. We only retain measurements having χ^2<5 units per degree of freedom (of which there are 138), $-9.4\ 10^{-4}<a/b<-5.4\ 10^{-4}$, $-0.22<a<-0.12$ and b<300 K. Here, a is in K×(frequency bin)$^{-1}$ and a/b in (frequency bin)$^{-1}$. We then repeat the fit retaining only frequency channels having $|\delta_j|<7$ and calculate the new values of the preceding quantities, which are also displayed in Figure 4.4 together with the earlier values. Finally, we only retain drift scans having a number N of retained measurements in excess of 270 (Figure 4.4). There are 64 of them.

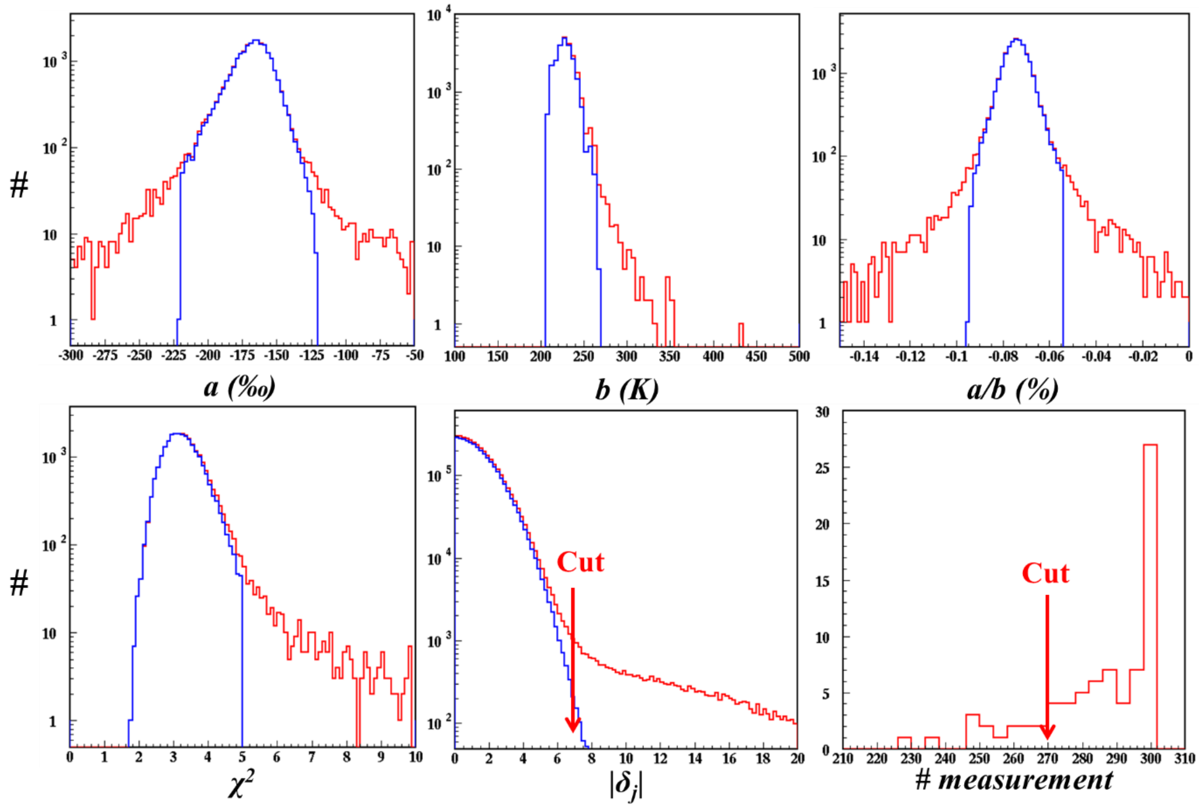

Figure 4.4 From left to right and top to bottom: distributions of a (‰), b, a/b (%), χ^2 and $|\delta_j|$ before (red) and after (blue) selection of the retained measurements. In the first four panels there is one entry per measurement, namely per frequency spectrum. In the fourth panel, there is one entry per frequency bin. The last panel displays the distribution of the number of retained measurements per drift scan (one entry per drift scan). Only drift scans having $N>270$ are retained for further analysis.

For each of the 64 retained drift scans, the b_i values of each retained measurement i (of which there are $N>270$ for this drift scan) are fitted to a form

$$b_i = T_{sky}[1+\xi(i-159)] + T_{Moon}\exp\left(\frac{-½(i-159)^2 cos^2\delta}{72.4^2}\right) \tag{4.1}$$

Here, the first term describes an empty sky contribution that varies linearly with time, with mean value T_{sky} and relative slope ξ. The second term describes the contribution T_{Moon} of the Moon, modulated by the beam as the Moon drifts across it. The values 159 and 72.4 correspond respectively to the value of i for the measurement pointing to the Moon and to the lobe width (σ=2.3°, meaning 9.2 min or 72.4 i bins divided by $cos\delta$). The resulting χ^2 distribution (calculated per degree of freedom for an uncertainty of 1 K on b_i) is displayed in Figure 4.5 left. The fit ignores the first four measurements (i<5) because they are used for calibration. Retaining only scans having $\chi^2<2$, we are left with a final sample of 52 drift scans. The distribution of the measured antenna temperature, from which the fitted sky temperature $T_{sky}[1+\xi(i-159)]$ has been subtracted, is compared in Figure 4.5 (right) with the result of the fit.

Distributions of T_{sky}, ξ and T_{Moon} are displayed in Figure 4.6. The latter, excluding 3 drift scans where T_{Moon} deviates by more than 3 K from its mean, has a mean value of 1.00 K with an rms value of 1.03 K. Ignoring possible systematic errors would mean an uncertainty of 1.00/$\sqrt{49}$= 0.14 K on T_{Moon}. The mean sky temperature has a mean value of 225 K with an rms value of 8 K and its time slope is centred on –12 ppm with an rms values of 49 ppm per 8.2 s, meaning respectively ~ –0.3 % and ~1.4 % over a full scan.

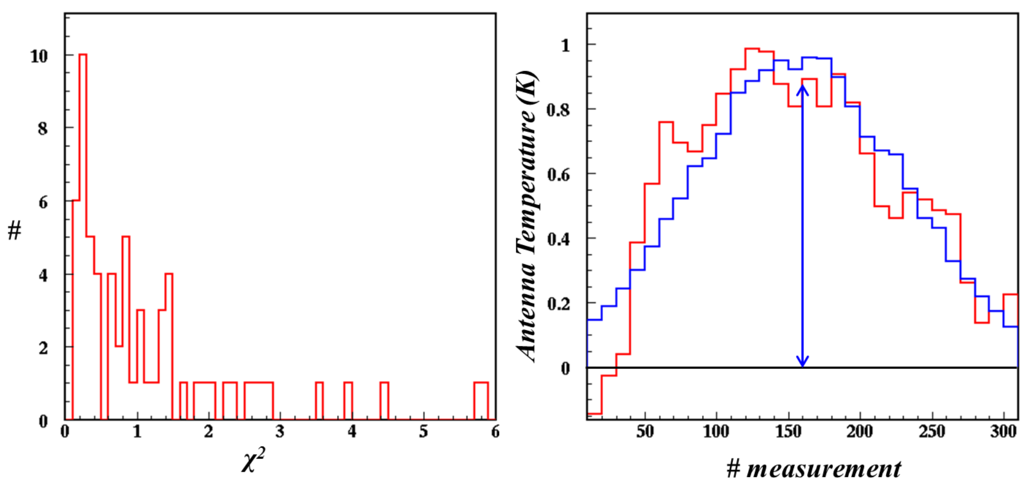

Figure 4.5 Left: Distribution of the χ^2 per degree of freedom obtained for the 64 final drift scans from fits of the b_i values to a form $T_{sky}[1+\xi(i-159)]+T_{Moon}exp[-½(i-159)^2/72.4^2]$. Right: Evolution of the antenna temperature as a function of measurement number, measured (red) and modelled (blue), from which the fitted sky temperature has been subtracted.

4.3 Discussion

We have obtained two different but consistent evaluations of the Moon antenna temperature, 0.7±0.2 K and 1.00±0.14 K. However, because of the different choices of frequency and of the better control over systematic errors offered by the drift scans, we prefer to retain the latter as our final result, using the former as a simple consistency check. Indeed, from the robustness of the results with respect to changes in the selection criteria, we estimate that the systematic uncertainty attached to the beam-switching result exceeds that attached to the drift scan result by factor of 2.

To the measured value of T_{Moon}, 1.00±0.14 K, we must add the contribution of the empty sky hidden behind the Moon and to its uncertainty a possible systematic contribution. The fraction of the solid angle, weighted by the gain of the antenna, covered by the Moon (angular diameter of 31’ and lobe σ of 2.3^{o}) is 0.66%. The antenna temperature measured on the empty sky takes values between 200 K and 250 K, ~225 K on average. Most of it is an effective system temperature, including all contributions other than from astronomical origin, the real contribution of the empty sky that is hidden behind the Moon is nearly negligible in comparison, just a few K (the HI line is out of the bandwidth). For an estimated empty sky antenna temperature of 5 K, we must add 0.03 K to the Moon antenna temperature.

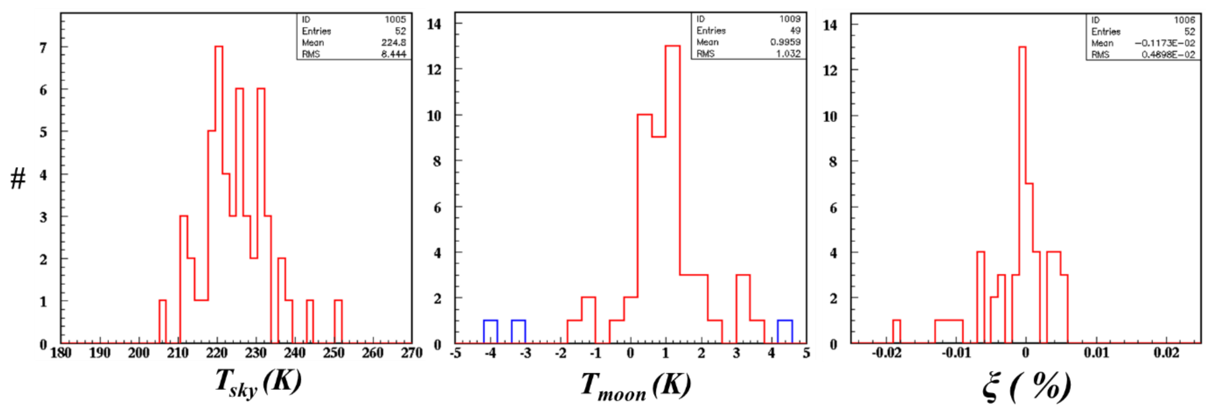

Figure 4.6 Left: Mean sky temperature, T_{sky} (K). Centre: Moon temperature, T_{Moon} (K). Right: Time slope of the sky temperature, ξ (in %).

From the robustness of this result as a function of the values adopted for the cuts, we estimate a systematic uncertainty of ~0.15 K. Adding it in quadrature to the value obtained from the rms dispersion of T_{Moon} around its mean, we retain as final result for the Moon antenna temperature: $T_{Moon}=1.03\pm0.20$ K. An estimate of the ultimate sensitivity of the instrument, as defined at the level of two standard deviations, is ~0.4 K for the antenna temperature, meaning ~300 Jy for the flux density, in agreement with earlier coarser estimates.

The Moon brightness temperature averaged over the whole disk has recently been measured (X.Z. Zhang *et al.* 2012) at 1420 MHz. The result, 233 K, is in good agreement with previous observations. The measurement was done on January 7th and 8th 2009, respectively 3 and 2 days before full Moon. As the Moon angular radius is 31'=4.5 10^{-3} rad, the Moon solid angle is $\Omega=\pi 4.5^2 10^{-6}=63.6\times10^{-6}$ sr and the flux density is therefore

$$2k_B\Omega\lambda^{-2}\times233=233\times0.0636\times10^{-3}\times(0.21)^{-2}\times2\times1.38\times10^{-23}\times10^{26}=0.93\text{ kJy},$$

corresponding to an antenna temperature of 1.16 K for the VATLY radio telescope in very good agreement with our measurement. Conversely, our result means a flux density of 0.83±0.16 kJy and a black body temperature of 207±40 K.

Figure 4.7 displays the variation of the Moon antenna temperature as a function of the phase φ of the Moon together with the result of a fit to a form $T_0+T_1\cos(\varphi-\varphi_0)$. Including such a phase dependence causes the χ^2 to decrease from 11.7 for 14 degrees of freedom to 10.2 for 12 degrees of freedom, implying that there is no evidence for any dependence of the Moon temperature on the phase. Indeed, it is well established (P.G. Mezger and H. Strassl 1959, J.E. Baldwin 1961, C.E. Heiles and F.D. Drake 1963, V.A. Razin and V.T. Fedorev 1963, P.H. Moffat 1972 and F.P. Schloerb *et al.* 1976) that the Moon brightness temperature at 1.4 GHz varies by less than 1% over a lunar month.

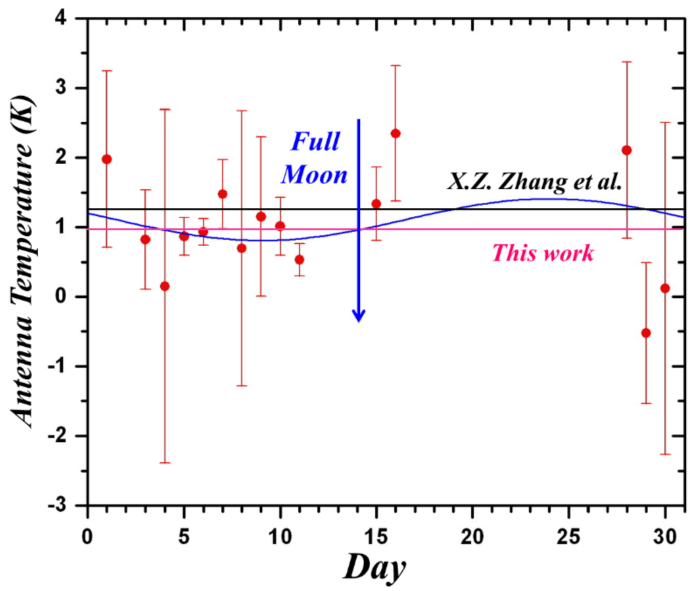

Figure 4.7 Variation of the measured antenna temperature of the Moon (red) as a function of its phase φ (measured in days from 0 to 30 starting at New Moon) together with the result of a fit (blue) to a form $T_0+T_1\cos(\varphi-\varphi_0)$, with $T_0=1.11$ K, $T_1=0.30$ K and $\varphi_0=-6.5^o$. The present result of T_{Moon}=1.03 K (no phase dependence) is shown as a magenta line and that of X.Z. Zhang *et al.* as a black line.

SUMMARY AND PERSPECTIVES

In four years of operation, the VATLY radio telescope has produced a number of studies that went well beyond what had been anticipated at the time of its acquisition. For a rather modest cost, less than 10 kUSD, it has turned out to be an efficient training tool providing an excellent introduction to the techniques and methods of radio astronomy.

Detailed studies of its performance have provided information on its main characteristics (pointing accuracy, system temperature, antenna efficiency factor, antenna temperature to flux density conversion factor, lobe width, etc.) as well as having revealed small effects, typically at the permil level, related to its basic design (such as non linearity and frequency dependence of the gain, features associated with the three sub-bandwidth structure, etc.). The importance of RFIs in limiting the sensitivity of the instrument has been demonstrated and their exploration has made it possible to minimize their influence. Much effort has been devoted to the understanding of the factors limiting the sensitivity of the instrument and two campaigns of observations dedicated to the detection of the thermal emission of the Moon have been particularly instructive in this respect. While measuring its black body temperature with an accuracy of 20% in good agreement with measurements obtained using more sophisticated instruments, they have made it possible to evaluate the ultimate sensitivity at the level of ~300 Jy.

Such a sensitivity is obviously insufficient to study targets other than the stronger radio sources in the sky. Yet, the observation of the Sun has given unexpected surprises when performed in conjunction with observations made in Australia at the Learmonth solar observatory using a similar instrument. One of these is the evidence for strong circular polarization of solar flare emission, taking advantage of the different feeds used by the two telescopes, a dipole in Learmonth and an helix in Ha Noi. The other is the observation of intriguing correlations between the periods of oscillations detected simultaneously by both telescopes. With amplitudes at the percent level and periods in the 6 minutes range, they turned out to result from multipathing between the direct Sun signal and its specular reflection on ground being detected in a side lobe. A simple model of the mechanism at play has described successfully the main features of the observed correlated oscillations.

Before the time covered by the present work, measurements of the Doppler velocity of hydrogen clouds in the disk of the Milky Way have given evidence for a differential rotation curve requiring the presence of a dark matter halo and have made it possible to draw a rough map of their distribution consistent with the known spiral arm structure.

The diversity of topics covered by these observations, inviting a concrete approach to their study, has been an opportunity to gain familiarity with a broad spectrum of astrophysics phenomena. In this respect, the telescope appears as an excellent training tool in basic astrophysics as well as in radio astronomy instrumentation.

It will continue to be used for the training of students at the undergraduate and master levels in the years to come. Possible extensions, such as operating with other similar antennas in interferometric mode or acquiring another telescope equipped with a right-handed feed in order to measure polarization are being contemplated.

BIBLIOGRAPHY

1. P.T. Anh (2010), Radio Detection of the Sun, Master thesis presented at the Institute of Physics, Hanoi
2. P.T. Anh (2012), presented at the 7th Annual Conference of the Thai Physics Society, May 9-12, 2012, Phranakhon Si, Ayutthaya, Thailand
3. M.J. Aschwanden *et al.* (1999), ApJ, 520, 880
4. J.E. Baldwin, 1961, MNRAS, 122, 513
5. S. Basu *et al.*, J. Atmos. Terr. Phys. 64 (2002) 1745
6. R.A. Benjamin *et al*. (2005), The ApJ 630, L149
7. G. Besla *et al.* (2007), ApJ 668, 949
8. G. Besla *et al.* (2010), ApJL 721, L97
9. L. Blitz (1979), ApJL 231, 115
10. L. Blitz, M. Fich and A.A. Stark (1982), Ap. J. Supp. 49, 183
11. J.G. Bolton (1982), Proc. Astron. Soc. Australia 4:349-58
12. J.G. Bolton (1948), Nature 162:141-2
13. J.G. Bolton and G.J. Stanley (1948a), Nature 161:312-3
14. J.G. Bolton and G.J. Stanley (1948b), Austral. J. Sci. Res. A1:58-69
15. J.G. Bolton and G.J. Stanley (1949), Austral. J. Sci. Res. A2:139-48
16. J.G. Bolton, G.J. Stanley and O.B. Slee (1949), Nature 164:101-2
17. W.B. Burton and M.A. Gordon (1978), A&A 63, 7
18. J. Chen and P.W. Schuck (2007), Solar Phys. 246, 145
19. W.N. Christiansen and J.V. Hindman (1952), Australian J. Sci. Res., A5, 437
20. E.CIPShurchwell *et al.* (2009), PASP 121, 213
21. D.P. Clemens (1985), ApJ 295, 422
22. Custom Astronomical Support Services Inc. (CASSI), 436 Highview Dr., Jackson, MO 63755, USA
23. E.W. Cliver, S.M. White and K.S. Balasubramaniam (2011), ApJ 743, 145 and references therein
24. J.M. Dickey *et al.* (2009), ApJ 693, 1250 and references therein
25. J. Diemand, M. Kuhlen and P. Madau (2007), ApJ 657, 262
26. Diep P.N., Phuong N.T., et al., 2014, PASA, 31, 29
27. H.I. Ewen and E.M. Purcell (1951), Nature 168, 356
28. G.B. Gelfreikh *et al.* (2004), Proc. IAU Symp. 223, 245, A.V. Stepanov, E.E. Benevolenskaya and A.G. Kosovichev, eds

29. E. Gonzalez-Solares *et al.* (2008), MNRAS 5388, 89
30. R. Hanbury Brown and R. Q. Twiss (1956), Nature 178/4541 (1956) 1046
31. Haslam et al. 1982, A&AS, 47, 1
32. F.D.A. Hartwick and W.L.W. Sargent (1978), ApJ 221, 512
33. C.E. Heiles and F.D. Drake, 1963, Icarus, 2, 281
34. N.V. Hiep (2012), *Observation of the 21 cm sky using the VATLY radio telescope*, Master thesis, presented at Vietnam Institute of Physics
35. N. V. Hiep *et al.* (2012), Comm. Phys. Vietnam, Vol 22, No 4, 365
36. N.V. Hiep *et al.* (2013), Comm. Phys. Vietnam. Vol.23, No 2, 107-119
37. N.V. Hiep *et al.* (2014), Sol. Phys. 289, 3, 939-950
38. N.V. Hiep *et al.* (2012), in Proc. of the 2nd Acad. Conf. on Nat. Sci. for Master and PhD students from Cambodia, Laos, Malaysia and Vietnam, Publishing House for Science and Technology, Vinh, Vietnam, 12
39. H.S. Hudson and A. Warmuth (2004), ApJ 614, 85
40. http://sprg.ssl.berkeley.edu/~hhudson/drafts/ii-osc/ms.pdf
41. R.A. Ibata *et al.* (2003), MNRAS 340, L21
42. IPS (2012a), Australian Government, Bureau of Meteorology, Radio and Space Weather Services, http://www.ips.gov.au/World_Data_Centre/1/10;
43. IPS (2012b), Australian Government, Bureau of Meteorology, Radio and Space Weather Services, http://www.ips.gov.au/Satellite/6/3;
44. P.M.W. Kalberla and J. Kerp (2009), Annu. Rev. Astro. Astrophys 47, 27
45. M. Karlicky and M. Barta, Nonlinear Processes in Geophysics (2004) 11: 471 and references therein
46. J.D. Kraus (1995), *A Helical-Beam Antenna Without a Ground Plane*, IEEE Antennas and Propagation Magazine, April 1995, p. 45
47. J.D. Kraus (1950), Antennas, McGraw-Hill
48. J.D. Kraus and R.J. Marhefka (2002), *Antennas: for All Applications*, third edition, McGraw-Hill
49. K.K. Kwee, C.A. Muller and G. Westerhout (1954), Bull. Astr. Inst. Netherl., 12, 211
50. R.E. Loughhead, J.A. Roberts and M.K. McCabe (1957), *The Association of Solar Radio Bursts of Spectral Type III with Chromospheric Flares*, Aus. J. Phys. 10, 483
51. N.M. McClure-Griffiths *et al.* (2007), ApJ 607, L127
52. L.L. McCready, J.L. Pawsey and R. Payne-Scott (1947), Proc. Roy. Soc. A190: 357-75

53. P.G. Mezger and H. Strassl, 1959, Planet. Space Sci., 1, 213
54. P.H. Moffat, 1972, MNRAS, 160, 139
55. A.F.J. Moffat, M.P. Fitzgerald and P.D. Jackson (1979), Astronom. Astrophys. Suppl. 38, 19
56. C.A. Muller and J.H. Oort (1951), Nature 168, 357
57. C.A. Muller and G. Westerhout (1957), Bull. Astr. Insts. Nethrlds. 13, 151;
58. N.T. Phuong *et al.* (2014), Comm. Phys. Vietnam, Vol 24, No 3
59. N.T. Phuong *et al.* (2014), Comm. Phys. Vietnam, Vol 24, No 4
60. N.T. Phuong, P.N. Diep and P. Darriulat (2014), *Solar data, Autumn/Winter 2013 campaign*, VATLY internal note 51
61. V.A. Razin and V.T. Fedorev, 1963, Radiofiz., 6, 1052
62. B. Roberts (2000), Solar Phys. 193, 139;
63. A. Rogers, http://www.haystack.mit.edu/edu/undergrad/srt/oldsrt.html
64. D.B. Sanders *et al.* (1986), ApJ. Suppl. 60, 1
65. F.P. Schloerb, D.O. Muhleman and G.L. Berge, 1976, Icarus, 29, 329
66. M. Schmidt (1957), Bull. Astr. Insts. Nethrlds., 13, 247
67. E.K. Smith and W.L. Flock (1994), NASA report 94-14671 (http://ntrs.nasa.gov/archive/nasa/casi.ntrs.nasa.gov/19940010198.pdf)
68. F.M. Strauss, P. Kaufmann and R. Opher (1980), Solar Phys. 67, 83
69. M. Su, T.R. Slatyer and D.P. Finkbeiner (2010), ApJ 724, 1044
70. W.T. Sullivan III (1991), Radio Interferometry: Theory, Techniques and Applications, IAU Coll. 131, ASP Conference Series, Vol. 19, 1991, T.J. Cornwell and R.A. Perley (eds.)
71. Tariq Malik (2012), *Solar Flare's Red Glare: Sun Unleashes Early Fourth of July Fireworks*, http://www.space.com/16400-solar-flare-sun-fireworks.html
72. N.T. Thao, N.T. Phuong et al. (2015), Comm. Phys. Vietnam, Vol 25, No 1
73. H.C. Van de Hulst (1945), Ned.Tijd.Natuurkunde, 11, 210
74. H.C. Van de Hulst, C.A. Muller and J.H. Oort (1957), Bull. Astr. Insts. Nethrlds. 12, 117
75. H. Weaver and D.R.W. Williams (1974), The Berkeley Low Latitude Survey of Neutral Hydrogen, Astron. & Astrophys. Suppl., 17 (1974) 1-249
76. G. Westerhout (1957), Bull. Astr. Insts. Nethrlds., 13, 201
77. A. Yanny *et al.* (2003), ApJ 588 (2003) 824 and 605 (2004) 575
78. X.Z. Zhang, A. Gray, Yan Su *et al.* (2012), RAA 12/9, 1297